

Soot Measurement and Species Simulation in Laminar Premixed Flames

By

Kenneth J Ho

A thesis submitted for the degree of Masters in Engineering Science



Faculty of Engineering, Computer and Mathematical Science
School of Chemical Engineering
University of Adelaide, Australia

DECLARATION

This work contains no materials which has been accepted for the award of any other degree or diploma in any university or any tertiary institution and to, the best of my knowledge and belief, contains no material previously published or written by another person, except where due reference has been made in the text.

I give consent to this copy of my thesis when deposited in the University Library, being made available for loan and photocopying, subject to the provisions of the Copyright Act 1968.

I also give permission for the digital version of my thesis to be made available on the web, via the University's digital research repository, the Library catalogue, the Australasian Digital Theses Program (ADTP) and also through web search engines, unless permission has been granted by the University to restrict access for a period of time

Kenneth Ho

ACKNOWLEDGEMENT

I would like to express my gratitude to all those people around me who have contributed much to my research in gas combustion and laser diagnostics for the past 2 years. Furthermore, I would like to mention the outstanding supervision efforts of Dr Zeyad Alwahabi, Dr Peter Ashman and Professor Gus Nathan who have relentlessly guided me on the right track.

I would like to thank those people in the lab who have helped me much in the lab: Paul Medwell and Shaun Chan. Without their attention to details, I would never get see certain elements in a more prospective way. Not forgetting Wang Yu from Shanghai, China who has helped me much in terms of understanding the fundamentals of laser diagnostics and soot morphology.

Last but not least, I would like to acknowledge the efforts of the support staff: Jason Peak and Brian Mulcahy for their excellent craftsmanship and advice. Without them, my laboratory layout would have never come to fruit. Above all, I would like to thank my family for giving me the support and guidance that I needed throughout these 2 years.

SUMMARY

This thesis reports on the study of laminar premixed ethylene/air flat flames, in both rich and lean conditions (ϕ at 1.82 to 3.80) at atmospheric pressure. The work was divided into experimental measurements of soot particles and theoretical computations of chemical products. In the experimental part, both intrusive sampling probes and non-intrusive laser diagnostics techniques were applied. The experimental measurements cover soot volume fractions by laser extinction (LE) and laser-induced incandescence (LII), temperatures by thermocouple insertion and soot morphology by thermophoretic sampling/transmission electron microscopy (TEM). The theoretical computations were performed using a detailed reaction kinetic model consisting of 544 elementary reactions among 100 chemical species to describe the formation and growth of polycyclic aromatic hydrocarbons (PAHs) up to pyrene. Results arising from this research would create a potential database, combined with visualizations, to focus as an education tool for students and researchers alike.

Two-dimensional imaging by LII revealed relatively uniform soot distributions from ϕ at 1.82 to 2.22. However, annular distributions were observed for fuel-rich conditions (ϕ at 2.84 to 3.80) which were elucidated to ambient air mixing due to low nitrogen shroud. The calibrated soot volume fraction profiles were in close agreement with LE for slightly sooty flames but differ by a magnitude of three for much sootier circumstances. Variable changes to the refractive index of soot, m resulted in potential errors between 3 to 11 % for soot volume fractions. Thermophoretic sampling was employed to complement the above methods. From TEM images, it was evident that soot particles undergo coagulation and aggregation and is a function of fuel equivalence. No obvious trends were seen in the particle size distribution. The effect of a low premixed reactant velocity was found to influence the magnitude and shape of the temperature profiles due to burner plate heat transfer. Ceramic coating on thermocouple wires was demonstrated to affect estimated temperatures by 205 K. The kinetic model provided an insight into the concentration profiles of minor, intermediate and aromatic species as reported in literature. It also addressed the importance of propargyl recombination reaction ($C_3H_3 + C_3H_3 \rightarrow C_6H_6$) into benzene as a fundamental step towards PAHs growth. Finally, a sensitivity analysis was carried out to tackle the influence of temperatures on chemical species.

Table of Contents

DECLARATION	i
ACKNOWLEDGEMENT.....	ii
SUMMARY	iii
LIST OF FIGURES	vii
LIST OF TABLES	x
1 INTRODUCTION.....	1
2 LAMINAR PREMIXED FLAMES.....	4
2.1 Introduction	4
2.2 Use of Flat Flames.....	5
2.3 Emissions from Premixed Combustion.....	7
2.4 Gas Handling System	8
2.5 Flowmeter Errors.....	15
2.6 Visual Observations	15
2.7 Summary	16
3 LASER EXTINCTION.....	18
3.1 Foundation of Laser Extinction.....	18
3.2 Soot Volume Fraction by Laser Extinction.....	18
3.3 Potential Errors Associated with Refractive Index of Soot.....	20
3.4 Experimental Description.....	22
3.5 Experimental Layout	23
3.6 Source of Errors.....	25
3.7 Results and Discussions	27
3.8 Summary	31
4 LASER-INDUCED INCANDESCENCE	33
4.1 Theoretical Basis	33
4.2 LII Considerations.....	34
4.3 Laser Intensity Profile	36
4.4 Time-Dependence Profile.....	38
4.5 Calibration via Laser Extinction.....	38
4.6 Experimental Description.....	39
4.7 Experimental Layout	41

4.8	Sources of Error.....	42
4.9	Results and Discussions	43
4.10	Summary	51
5	FLAME TEMPERATURES	53
5.1	Choice of Measurement.....	53
5.2	Thermocouple Types	54
5.3	Thermocouple Properties and Their Advantages	56
5.4	Measurement of Gas Temperature	57
5.5	Factors Influencing Temperature	59
5.6	Experimental Description.....	60
5.7	Experimental Layout	62
5.8	Thermocouple Interruption.....	63
5.9	Results and Discussions	64
5.10	Summary	67
6	SOOT MORPHOLOGY	69
6.1	Development of Soot.....	69
6.2	Thermophoretic Sampling Particle Deposition	73
6.3	Sampling Layout	74
6.4	Results and Discussions	76
6.5	Summary	81
7	COMPUTATIONAL MODELLING.....	83
7.1	Chemical Kinetics	83
7.2	Flame Radicals	85
7.3	Computational Procedure	90
7.4	Results and Discussions	97
7.5	Sensitivity Analysis.....	104
7.6	Summary	107
8	CONCLUSION OVERVIEW	108
9	POTENTIAL WORK RECOMMENDATIONS	110
10	NOMENCLATURE.....	111
10.1	Symbols.....	111
10.2	Greek Symbols	112
10.3	Acronyms	112
10.4	Chemical Species Acronyms.....	112
11	BIBLIOGRAPHY	113

APPENDICES

A	Premixed Flame Calculations	128
A.1	Refractive Index of Soot	128
A.2	Visual Determination of Laser Path.....	128
A.3	Flame Extinction	129
A.4	Soot Volume Fraction	130
A.5	Treatment of LII Signals	130
A.6	Radiation Heat Losses Correction	131
A.7	Soot Microscopy Statistical Analysis	132
B	PREMIX Default Variables	133
B.1	Solver Input Details	133
B.2	Reaction Zone Dimensions	134
C	Tabulated Results	135
C.1	Soot Volume Fraction (LE)	135
C.2	Calibration of Soot Volume Fraction (LII)	144
C.3	Temperatures after Correction	150
D	Mass Flow Controller Calibration Sheets	157
E	Publications	159

LIST OF FIGURES

Figure 1 Global carbon dioxide emissions from fossil fuel burning, 1950 – 2006 [31].....	4
Figure 2 Schematic structure of the flat flame burner [34] against porous burner.....	6
Figure 3 Microstructure of soot particle from diesel combustion [48].....	8
Figure 4 McKenna flat flame burner [34].....	9
Figure 5 Front and side views of traverse and plate	10
Figure 6 Tube and Mass Flowmeters Calibration Setup.....	11
Figure 7 Calibration relationship between tube flowmeters and mass flow controller	12
Figure 8 Photographs of stabilised premixed ethylene flames at $\varnothing = 1.82$ to 3.80	15
Figure 9 Helium-neon laser (Thorlabs, Inc)	22
Figure 10 Single beam procedure (Stanford Research Systems).....	23
Figure 11 Laser extinction experimental layout	23
Figure 12 In-house built photodiode with sheath	25
Figure 13 Mean extinction measurements for He-Ne laser for the duration of 1 hour.....	26
Figure 14 Soot volume fraction profiles (Axial) by LE at $\varnothing = 1.82 - 3.80$; symbols: measurements; lines: third-order polynomial fit.....	28
Figure 15 Effect of different refractive index at $\varnothing = 2.22$	30
Figure 16 Schematic diagram of the optical arrangements for 2-D LII measurements [81]....	33
Figure 17 TEM micrographs of laser-heated soot captured via thermophoretic sampling. Values of the laser fluence were a) 0.15, b) 0.3, c) 0.6 and d) 0.9 J/cm ² [87].....	36
Figure 18 Fluence dependence of LII measured in steady laminar diffusion flames. Data were collected at $H = 20$ mm in the ethylene/air flame for detection gate durations of 19ns (+) and 85ns (\diamond), both gates opening coincident with the arrival of the ≈ 5 ns laser pulse. Data also shown for the methane/air flame at $H = 50$ mm with the 85ns gate (\bullet). Raw signals for each condition have been normalized to a value of 1.0 at a fluence of 0.6 J/cm ² . The solid line shown is the least-square power-law fit of the methane data for fluences greater 0.3 J/cm ² ; the fit follows the expression $\text{signal} \propto \text{fluence}^{0.34}$ [13].....	37
Figure 19 Temporal profile of a LII signal obtained in the ethene-air laminar diffusion flame at heights of 10 and 30 mm above the fuel tube exit and at the radial locations corresponding to peak soot volume fraction for these heights [85].....	38
Figure 20 Model Brilliant B Nd:YAG Twins [90]	40
Figure 21 High performance camera use fiber optic taper/face plate (B) to couple the intensifier (A) to the CCD (C) [91]	40
Figure 22 Interference filter of 410 nm \pm 10 nm	41

Figure 23 Laser induced-incandescence experimental layout	41
Figure 24 Comparison of LII beam profile at $\varnothing = 2.22$ at HAB 11 mm as function of radial position.....	43
Figure 25 LII signal (Arbitrary) as a function of laser fluence at $\varnothing = 2.22$ of HAB 11 mm; insert: burnt image at laser fluence of $6.85 \times 10^9 \text{ J/cm}^2$	44
Figure 26 Time dependence of the LII signals as a function of HAB at $\varnothing = 2.22$; symbols: measurements; lines: second-phase exponential fit	45
Figure 27 Raw instantaneous LII images at $\varnothing = 1.82 - 3.80$ as a function of HAB 7 to 15 mm; excitation wavelength at 532 nm (Note RGB is based on colour map jet).....	46
Figure 28 Normalized radial LII profiles, calibrated to the highest intensity at $\varnothing = 2.22$	48
Figure 29 Soot volume fraction profiles (axial) as a function of HAB, calibrated to $\varnothing = 2.22$	49
Figure 30 Comparison of radial soot volume fraction profiles between a) LE and b) LII at $\varnothing = 2.84$	51
Figure 31 Basic thermocouple circuit [102]	56
Figure 32 Measured temperature profiles and their corresponding flowrates at $\varnothing = 2.07$ [114]	59
Figure 33 Effect of laminar burning velocities of ethane, ethylene and acetylene with air at atmospheric pressure as a function of equivalence ratio [94].....	60
Figure 34 Cross-section of Type R thermocouple	61
Figure 35 Thermocouple placement layout	62
Figure 36 Flame disruption by thermocouple.....	63
Figure 37 Temperature profiles (axial) at $\varnothing = 1.82$ to 3.80 from HAB 3 to 19 mm at flame centreline; symbols: measurements; lines: third-order polynomial fit	64
Figure 38 Temperature profile (radial) at $\varnothing = 2.84$ at HAB 15 mm; line: second-order polynomial fit.....	66
Figure 39 Electron micrographs of soot particles chains. Mean diameter of particle ca. 200 \AA [1].....	69
Figure 40 Schematic reaction path for soot formation in premixed flames [47]	70
Figure 41 H-abstraction- C_2H_2 -addition mechanism for PAH Growth [48]	72
Figure 42 TSPD experimental arrangement	74
Figure 43 TEM grid holder.....	75
Figure 44 TEM photographs (with a resolution of 64,000) of soot sampled at $\varnothing = 1.82, 2.22, 2.84$ & 3.80 as function of HAB at (a) 9mm, (b) 11mm, (c) 13mm, (d) 15mm, (e) 17mm	78
Figure 45 Mean particle size diameter as function of HAB as determined from TEM Photographs at.....	79

Figure 46 Primary particle development at $\phi = 2.84$ for six HABs on flame centreline	80
Figure 47 Simple hydrocarbon fuels oxidation mechanism hierarchy [136].....	84
Figure 48 Reaction mechanism for a stoichiometric C_2H_6 -air oxidation [137].....	85
Figure 49 Schematic diagram of cyclopentadienyl radical reaction with methyl [140].....	87
Figure 50 Resonantly-stabilized radicals with multiple electronic configurations [140].....	90
Figure 51 Schematic diagram of propargyl recombination channels that form single-ring aromatic hydrocarbons [140].....	90
Figure 52 Solution speed comparisons between different versions of CHEMKIN [®] (Linux 64-bit Platform).....	91
Figure 53 Simulation pathway in PREMIX flame code	92
Figure 54 Relationship of PREMIX program to CHEMKIN and TRANSPORT pre-processors, and to the associated input and output files [154].....	93
Figure 55 PREMIX procedural outlines	95
Figure 56 Starting estimate to the zone width and centre [154]	96
Figure 57 Minor species profiles at a) 1.95, b) 2.22, c) 3.10 & d) 3.80	98
Figure 58 Intermediate species profiles at a) 1.95, b) 2.22, c) 3.10 & d) 3.80	99
Figure 59 Aromatic species profiles at a) 1.95, b) 2.22, c) 3.10 & d) 3.80	102
Figure 60 Effect of reduced temperature on minor species profiles at $\phi = 2.22$ as a function of HAB	104
Figure 61 Effect of reduced temperature on acetylene at $\phi = 2.22$ as a function of HAB.....	105
Figure 62 Effect of reduced temperature on aromatics growth at $\phi = 2.22$ as a function of HAB	106
Figure 63 Measurement of laser path at $\phi = 2.22$	128
Figure 64 Solver default variables	133
Figure 65 Calibration Sheet for Ethylene Mass Flow Controller	157
Figure 66 Calibration Sheet for Air Mass Flow Controller	158

LIST OF TABLES

Table 1 Actual flow conditions and equivalence ratios	13
Table 2 Summary of flame test conditions	14
Table 3 Summary of complex refractive index of soot	20
Table 4 Comparisons of methods used in flame temperature measurements [32]	53
Table 5 Summary of laser optical path through luminous part of flame	129
Table 6 Summary of reaction zone inputs used in CHEMKIN	134
Table 7 Summary of extinction measurements and soot volume fractions at $\varnothing = 1.82$	135
Table 8 Summary of extinction measurements and soot volume fractions at $\varnothing = 1.95$	136
Table 9 Summary of extinction measurements and soot volume fractions at $\varnothing = 2.08$	137
Table 10 Summary of extinction measurements and soot volume fractions at $\varnothing = 2.22$	138
Table 11 Summary of extinction measurements and soot volume fractions at $\varnothing = 2.84$	139
Table 12 Summary of extinction measurements and soot volume fractions at $\varnothing = 3.10$	140
Table 13 Summary of extinction measurements and soot volume fractions at $\varnothing = 3.80$	141
Table 14 Summary of radial extinction measurements and soot volume fractions at $\varnothing = 2.84$	142
Table 15 Calibration of LII signals into soot volume fraction at $\varnothing = 1.82$	144
Table 16 Calibration of LII signals into soot volume fraction at $\varnothing = 1.95$	145
Table 17 Calibration of LII signals into soot volume fraction at $\varnothing = 2.08$	145
Table 18 Calibration of LII signals into soot volume fraction at $\varnothing = 2.22$	146
Table 19 Calibration of LII signals into soot volume fraction at $\varnothing = 2.84$	146
Table 20 Calibration of LII signals into soot volume fraction at $\varnothing = 3.10$	147
Table 21 Calibration of LII signals into soot volume fraction at $\varnothing = 3.80$	147
Table 22 Radial soot volume fractions from LII calibration at $\varnothing = 2.84$	148
Table 23 Axial temperatures after radiation correction at $\varnothing = 1.82$	150
Table 24 Axial temperatures after radiation correction at $\varnothing = 1.95$	151
Table 25 Axial temperatures after radiation correction at $\varnothing = 2.08$	152
Table 26 Axial temperatures after radiation correction at $\varnothing = 2.22$	153
Table 27 Axial temperatures after radiation correction at $\varnothing = 2.84$	154
Table 28 Axial temperatures after radiation correction at $\varnothing = 3.10$	155
Table 29 Axial temperatures after radiation correction at $\varnothing = 3.80$	156
Table 30 Radial temperatures after correction at $\varnothing = 2.84$	156

1 INTRODUCTION

The combustion of premixed hydrocarbon fuels in atmospheric flames has been the subject of numerous investigations lately. Under fuel-rich conditions, the process of incomplete combustion leads to the formation of soot. The presence of soot in flames not only affects the heat radiant properties but may also affect the associated chemical reactions. The physical and chemical processes associated with soot formation and oxidation is complex and often affects reliable predictions of chemical precursors and their mass growth to soot particulate matter by computational modelling. Motivated by these observations, the present study is aimed in two directions; 1) Investigation of soot formation in laminar premixed flames by reliable physical techniques such as laser extinction, laser-induced incandescence and thermophoretic sampling and 2) Possible prediction of chemical species and aromatics responsible for soot formation by computational modelling.

The formation of soot stems from the thermal conversion of a hydrocarbon fuel into carbonaceous agglomerates consisting of near spherical soot particles with about 10^6 carbon atoms [1]. Soot formed within the burnt gases can be described by the volume fraction, f_v , number density, N and particle size, d_p . To determine these properties, an elastic scattering from soot as a result of interaction with laser radiation is employed. This technique is commonly referred to as laser extinction (LE). It is able to provide line-of-sight temporal measurements across a finite laser path through the combustion zone and post-flame region. Measurements of soot volume fraction is vital to the study of soot growth within laminar flames [2, 3]. In post-flame region, laser extinction method is also used to estimate specific extinction coefficient per unit of fuel mass [4, 5].

Recently, laser-induced incandescence technique (LII) is applied to combustion systems to determine quantitative soot volume fraction distributions via two-dimensional imaging to construct a complete picture of soot characterization. Numerous works on the LII technique have shown promise towards spatial and resolved soot volume fractions in laminar premixed [6-11] and diffusion flames [12-14]. This technique behaves similarly to laser extinction except that the soot particles are heated to vaporisation temperatures by high laser intensities. As a result, they emit thermal radiation or incandescence proportional to the local soot volume fraction as pointed out by Melton [15]. The LII signals are often calibrated against soot volume fractions by laser extinction [6-8, 12]. However, interpretation of soot structure cannot be achieved by these laser diagnostics. Therefore to fully resolve issues regarding soot

formation/growth/aggregation/oxidation, another analytical method such as thermophoretic sampling is employed.

The application of thermophoretic sampling and analysis by transmission electron microscopy (TEM) as discussed by Dobbins and Megaridis [16] and subsequently improved by Koylu and co-workers [17], is normally used in conjunction with other optical techniques to complement the formation of soot in terms of morphology and size distribution. This technique works on the theoretical basis of thermophoresis by Eisner and Rosner [18] whereby soot particles are driven by a temperature gradient to deposit on the cold probe surface immersed in flames. The forte of thermophoretic sampling is that it is able to individually characterize each type of morphology as soot progresses from particle inception to surface growth and finally to carbonaceous aggregation state.

To fully understand the probable pathways towards soot formation, computational modelling is undertaken to investigate the reaction kinetics behind premixed flames. Recent efforts have been devoted towards the detailed formulation of reaction kinetics in polycyclic aromatic hydrocarbons (PAHs) formation, growth and oxidation in premixed flames [19-26]. In particular, the mechanism of benzene production via propargyl (C_3H_3) recombination receives much attention [19-22]. The formation of PAHs from benzene mass growth is found to be likely precursors to soot [27, 28]. A detailed reaction mechanism proposed by Frenklach and Wang [21] and updated by Appel and co-workers [19], describes the formation of benzene and mass growth of PAHs in rich laminar premixed flames with a reasonable level of accuracy and is still the basis of most soot models to-date. This model is commonly referred as the ABF soot model [29]. In this model, soot growth occurs mainly by acetylene (C_2H_2) addition and condensation of PAHs. Soot particles are incepted by the dimerisation of pyrene via H-abstraction- C_2H_2 -addition sequence [24]. This same mechanism applies to the surface growth reactions on particle surface and remains relatively unchanged throughout all these studies.

Despite significant advances in laser diagnostics and thermophoretic sampling towards soot property characterization, no study has yet bridged the gap between experimental means and computational modelling to determine the chemical species relevant to soot formation. Therefore, the main aim of this research is to apply intrusive and non-intrusive experimental techniques in laminar premixed flames, emphasizing on soot nucleation and surface growth. In addition, the simulation of chemical and aromatic species using a user-friendly combustion software CHEMKIN[®] [30] combined with an existing open-source soot model [29] helps to

interpret and correlate the experimental results, considering the reaction pathways towards benzene production and mass growth of PAHs into soot. Experimental conditions are tested for a range of equivalence ratios ($\phi = 1.82$ to 3.80) in laminar premixed ethylene/air flat flames at atmospheric pressures, including those reported [2, 7].

2 LAMINAR PREMIXED FLAMES

The main focus of this research is dealing with soot measurements and species simulation relating only to laminar premixed flames. This chapter reviews the background behind the ability of a commercialised flat flame burner (McKenna burner) able to produce stabilised, one-dimensional flames which is necessary for spatial and temporal measurements. Pollutant emissions from premixed combustion are briefly described. Other elements such as stabilising plate, traverse and mass flow controllers involved in the gas handling system are outlined as well. Flame test conditions in both fuel-lean and fuel-rich conditions ($\phi = 1.82$ to 3.80) are considered for this research.

2.1 Introduction

Combustion can be defined as a rapid gas-phase chemical reaction that results in the formation of stable by-products and visual radiation emissions in the form of flames. Gas combustion often refers to the reaction between a gaseous fuel reacting in the presence of an oxidant, commonly air or other supporting reactants. These gaseous fuels are classified as hydrocarbon gases namely natural gas, ethylene and propane which are constituents of gas coal after distillation. In some cases, due to the insufficient oxidant interaction, harmful derivatives are emitted which can affect the environment and peoples' well being. One such emission is carbon dioxide (CO_2) as demonstrated by its severity in Figure 1. Although it is considered to be one of the main stable by-products, but it is acknowledged to be one of the main attributable causes for climate change. Combustion researchers are actively revising current technologies to reduce the amount of carbon waste into the environment.

Flames are usually separated into two main categories; either premixed flames or non-premixed flames. The differences between these two types of flame are attributed to the way in which fuel and oxidant are introduced into the burner. For premixed flames, reactants are homogeneously mixed prior to the burner exit. However for non-premixed flames, only fuel is allowed through the burner and mixes with the ambient environment by molecular diffusion upon exit. This type of flame is often referred as a *diffusion* flame. From these two types of flames comes another classification which deals with the fluidic nature of the gas flow in the reaction zone – *laminar* and *turbulent*. Essentially *laminar* flow involves mixing and transport of species at molecular level whereas *turbulent* flow involves macroscopic eddying motion [32]. Typically, laminar premixed flames are more commonly inferred used as main combustion medium to analyse chemical species, temperatures and soot concentrations based on the assumptions that it burns at a constant pressure and there is local thermal equilibrium within the flame [33]. In order to achieve these effects, a flat flame porous plug burner (McKenna Burner) is used. The flat flames produced are known to exhibit spatial and temporal uniformity in their exhaust regions. Therefore, these flames are well-suited for calibration purposes such as temperature and laser diagnostics.

2.2 Use of Flat Flames

The combustion processes involving laminar premixed flames are still complex and require expressions for thermodynamics and transport properties. In order to rectify this problem, a flat flame burner is needed to produce flames one-dimensional flames. These flat flames are shown to provide spatial and temporal uniformity in terms of temperature and species conditions at well-defined conditions and hence suitable for in-depth analysis.

NOTE:
This figure is included on page 6
of the print copy of the thesis held in
the University of Adelaide Library.

Figure 2 Schematic structure of the flat flame burner [34] against porous burner

For this present study, a porous burner of diameter 30 mm, similar to the McKenna flat flame burner, is used to produce one-dimensional laminar flat flames as shown in Figure 2. The flat flame burner consists of a porous plate in either stainless steel or bronze configuration for flame stabilisation. A copper coil is embedded in its matrix to allow cooling water to pass through to prevent over-heating. Moreover by allowing the co-annulus flow of an inert gas through the porous plate, shear layer mixing is minimized and maintains flame homogeneity [35]. This burner matrix has been extensively used by combustion researchers for temperature and species analysis in a variety of gaseous fuels such as hydrogen [36], methane [35, 37], propane [38, 39] and ethylene [40]. Because of the simple geometry and spatial uniformity of the flames, the McKenna burner is highly regarded as a calibration tool for temperature and species measurements.

The constant throughput by the McKenna burner allows precise measurements of soot volume fractions using suitable laser and mass diagnostics such as laser extinction [2, 41, 42], laser-induced incandescence [7, 9] and gravimetric sampling [43]. Generally, soot measurements carried out by the line-of-sight light extinction is normally used as a calibration for other non-intrusive laser techniques such as laser-induced incandescence [2, 6, 8]. Moreover, probe measurements in laminar premixed flat flames yield useful information about soot inception kinetics and soot surface growth [23, 44]. Therefore the combination of intrusive and non-intrusive measurements allows researchers to postulate the formation of soot from a molecular

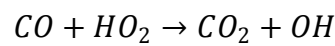
level up to graphitization. Therefore it would be advisable to use the same „laboratory-standard“ burner used for combustion analysis and comparison to eliminate experimental differential.

2.3 Emissions from Premixed Combustion

Primary pollutants from premixed combustion, as a result from insufficient oxidation, consist primarily of carbon by-products and oxides of nitrogen. As premixed industrial-grade (98%) ethylene of interest here, SO_x emissions are neglected in this scenario.

2.3.1 CO

Carbon monoxide is a colourless and odourless but toxic gas, produced as a resultant effect of partial combustion with oxidiser. This poses a significant threat to human health and also elevates the concentration of CO₂ in the atmosphere through further oxidation. However, the production of CO after the fuel breakdown is important as it acts like a chain-propagating step towards the formation of CO₂ with the liberation of hydrogen radicals (H) and even hydroxyl radicals (OH) via CO oxidation with HO₂ [45]:



2.3.2 CO₂

Carbon dioxide is the typical by-product of any complete combustion involving carbonaceous fuel. It is identified to be one of the main contributors to greenhouse gas emissions, leading to global warming [31]. Therefore reducing CO₂ emissions from combustion processes is essential for environmental sustainability. Possible remedies to lower CO₂ emissions is by increasing the system efficiency in terms of excess oxidation and revamping current technologies so that less fuel would be needed.

2.3.3 Soot

The formation of soot has long been a problem for combustion engineers and scientists alike. It is described as the formation of a particulate matter of carbon within the flame. Soot formation in flames involved two conceptually distinct steps; particle inception and surface growth [44]. Literature reviews into the formation of polycyclic aromatic hydrocarbons (PAHs) and its relationship to soot has been extensively discussed from the 1950s [46] up to present [28, 47, 48] but uncertainties still remains in terms of the first PAHs formation leading up to soot. Details into the characteristics of an individual soot particle from typical

diesel combustion has been analysed as well [48]. One such example is shown in Figure 3. Altering the amount of O₂ present in the oxidiser would significantly suppress soot formation [46].

Figure 3 Microstructure of soot particle from diesel combustion [48]

2.3.4 Oxides of Nitrogen

In the combustion of fuels with little or no nitrogen, nitric oxides or NO_x is generally formed by three chemical mechanisms that involve nitrogen from the air. They are thermal, prompt and N₂O-intermediate mechanisms [45]. As summarized, thermal mechanism involves high temperature combustion over a wide range of equivalence ratios whereas prompt mechanism only dominates in the fuel-rich combustion. The N₂O-intermediate mechanism focuses on the formation of NO in fuel-lean low temperature processes.

Among the different forms of NO_x emissions, the formation of nitrogen oxide (NO) is considered to be the most important as it oxidizes to form nitrogen dioxide (NO₂) which ultimately forms acid rain and smog. Reducing peak temperatures and increasing oxygen content are some of the ways to reduce NO_x emissions. Further details on NO_x reduction strategies can be found in Turn's work [45].

2.4 Gas Handling System

This sections not only details the specifications of the McKenna flat flame burner used in this research but also addresses the movability of the vertical traverse used to support the burner as well. The purpose of a 65 mm stainless steel plate above the burner acts like a bluff-body to the flames. The positions of mass flow controllers after tube flowmeters are not only used to determine exact flowrates but also calibrate flowrates as shown on tube flowmeters. Flame test conditions for each equivalence ratio are drawn respectively in terms of exit velocity, mass flux and their associated reactant mass fractions.

2.4.1 Flat Flame Burner

NOTE:
This figure is included on page 9
of the print copy of the thesis held in
the University of Adelaide Library.

Figure 4 McKenna flat flame burner [34]

The flat flame burner is able to give optimal spatial and temporal measurements of temperature and species particularly for laminar premixed flames. For this present study, a 30 mm sintered stainless steel porous flat flame burner encompassed by a 15 mm bronze mesh shroud is used for laminar premixed flame combustion at atmospheric pressure in Figure 4. Flame stability is achieved by making the incoming premixed gas lower than burning velocity (S_L) so that the flame burns back to the burner plate. As the flame approaches the plate, some of the heat is lost to the burner plate as conduction [49] and results in a stabilised flame. In addition, operation of the annular co-flow shroud allows the use of inert gas such as nitrogen to prevent air entrainment towards the flame base. This brings about uniformity for soot volume fractions measurements by laser extinction and laser-induced incandescence. Moreover the burner's sintered stainless steel plug has an internal cooling water coil which allows heat conduction to the burner to be minimized during experiments. The minimum rate at which the burner matrix has to be sufficiently cooled is set at a temperature of 297 ± 2 K with a flowrate of 1 litre per minute.

2.4.2 Vertical Traverse

The movable traverse in Figure 5 forms the base platform for the flat flame burner, providing stability and mobility along the axial position with minimal radial deviation. The entire setup is constructed of stainless steel and is held together by two guide rods drilled into the base platform. The traverse is held in place on a magnetic base attached to a metal plate so that its position would be fixed and remain constant for each experiment. The spinal column of the dual platforms is held together by the use of a 500 mm long tapered screw thread. This tapered screw thread is able to increase the axial height of the burner platform to the nearest 0.5 mm. Rods are installed to guide the burner platform with minimum radial positions with ± 10 % accuracy. The platform is able to reach maximum heights of 400 mm which is feasible

for further studies involving larger flowrates. Nonetheless, heights of up to 230 mm are only required.

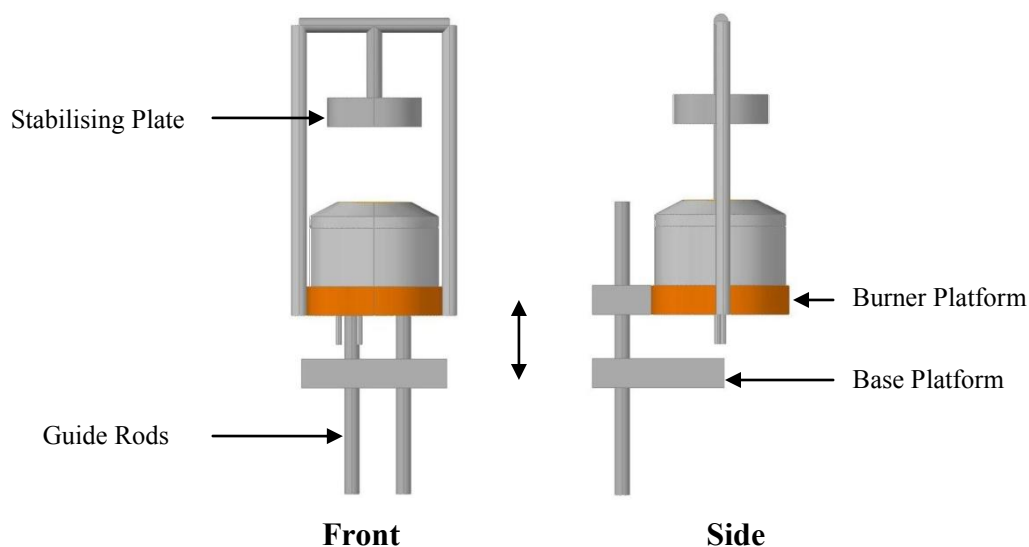


Figure 5 Front and side views of traverse and plate

2.4.3 Stabilising Plate

The placement of the stabilising plate displayed in the Figure 5 plays a major role in the analysis of one-dimensional flat flames. The custom-made plate is made out of stainless steel and measures about 65 mm in diameter with a thickness of 10 mm. The stainless steel plate suppresses the typical flame conical configuration and produces a stabilised but yet flat reference surface. The plate rods not only pivot as a building block to the stabilising plate, but also act as an adjustable stand for vertical movement. The flat flames produced are found to stabilise without any visible oscillations around HAB 3 mm as reported [50]. The burner plate positioned at 23 mm above burner which is found to yield the most favourable conditions for stabilised flames from ϕ at 1.20 to 2.95. A stainless steel mesh is placed on top of the burner plate to ensure uniform mixing at burner exit.

2.4.4 Premixed Gas Configuration

The metered flows for each of the gases are measured using tube and ball flow meters mounted on a stainless steel board for visibility and movability purposes. The ethylene and nitrogen gases used in the experiments are supplied via gas cylinders. Air Liquide [51] lists the gases as following: ethylene – 98 % purity and nitrogen – 99.5 % purity. In addition, air is supplied by an air compressor via external piping which is fitted with an in-line filter. Needle valves are installed on the outlet of each rotameter to facilitate precise movability to ± 1 % of its graduation mark. The flows of ethylene, air and nitrogen are calibrated by the use of mass

flow controllers (Bronkhorst High-Tech, Model F-201CV-500AAAD-22-E), custom set for maximum rates of 1000 ml/min air and 200 ml/min ethylene at specified conditions of 137.9 kPa and 20 °C. The flow conversion sheets can be found in Appendix D. Both mass flow controllers are connected and controlled via a power supply/readout unit (Bronkhorst High-Tech, Model E-5714). Both fuel and oxidant are premixed at room temperature prior to burner delivery. Check valves are installed to prevent flashback during combustion. An illustration of the above description is shown in Figure 6.

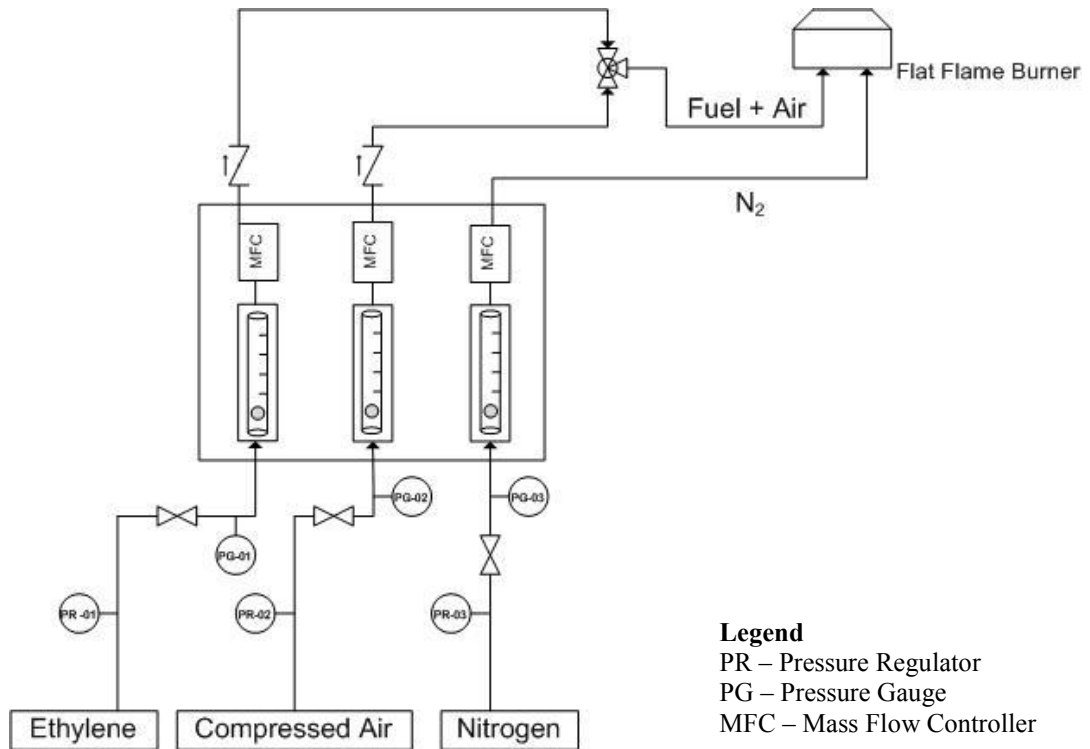


Figure 6 Tube and Mass Flowmeters Calibration Setup

By keeping the mass flow controllers at 100 % open and manually operating the tube flowmeters, a direct relationship between them can be established for each gas type. Figure 7 show the calibration relationships between the analog tube flowmeter and digital mass flow controller for ethylene, air and nitrogen separately.

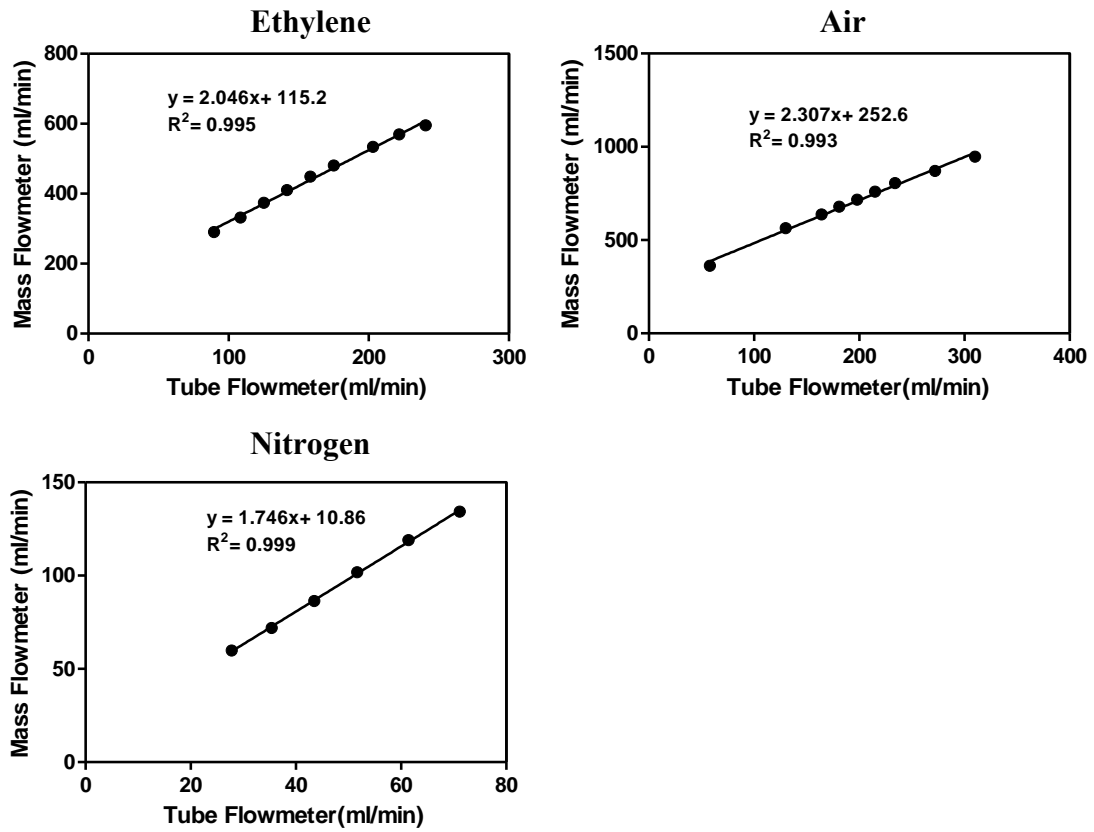


Figure 7 Calibration relationship between tube flowmeters and mass flow controller

Equivalence ratio, ϕ is defined as a ratio of experimental fuel-oxidant ratio and stoichiometric fuel-oxidant ratio, $(F/O)_{st}$ [45]:

$$\phi = \frac{(F/O)}{(F/O)_{st}} \quad \text{Equation 2.1}$$

Having established the relationship between tube flowmeter and mass flow controllers, actual flow conditions can be derived to yield corresponding equivalence ratios as listed in Table 1.

Table 1 Actual flow conditions and equivalence ratios

	Tube Flowmeter (ml/min)	After Calibration (ml/min)	Ø
Ethylene	91.98	303.30	
Air	954	2452.42	1.82
	880.8	2283.62	1.95
	822	2148.03	2.08
	763.8	2013.82	2.22
	572.4	1572.45	2.84
	513.6	1436.86	3.10
	399	1172.59	3.80
Nitrogen	71.74	136.05	

2.4.5 Flame Test Conditions

Seven premixed ethylene/air flames are investigated, having equivalence ratios in the range from 1.84 – 3.80 as summarized in Table 2. Flame conditions are carried out at 137.9 kPa (gauge) and 298 K. Ethylene flowrate is kept constant at 303 ml/min whereas air flowrate is varied to achieve the required test conditions. Annular nitrogen co-flow remains static at a constant volumetric flow of 136 ml/min for shroud purposes. Air drafts are minimized by the use of metal sheets placed 40 cm surrounding the burner. An exhaust hood is placed 1 metre above the burner to draw off the sooting combustion products. Adiabatic temperatures are calculated using a combustion equilibrium program – GASEQ [52].

Table 2 Summary of flame test conditions

Flame Test	Air flowrate (ml/min)	Equivalence Ratio (Φ)	T_{ad} (K)	Burner Exit Velocity, U_o (m/s)	Mass Flux x 10⁻³ (kg/m².s)	Reactant Mass Fraction		
						C₂H₄	O₂	N₂
1	2452.42	1.82	1933	0.97	203.64	0.103	0.195	0.702
2	2283.62	1.95	1866	0.91	191.07	0.110	0.194	0.696
3	2148.03	2.08	1799	0.87	180.98	0.116	0.192	0.691
4	2013.82	2.22	1733	0.82	170.98	0.123	0.191	0.686
5	1572.45	2.84	1447	0.66	138.13	0.152	0.184	0.663
6	1436.86	3.10	1372	0.62	128.03	0.164	0.182	0.654
7	1172.59	3.80	1332	0.52	108.36	0.194	0.175	0.630

2.5 Flowmeter Errors

Separate gas flows for ethylene, air and nitrogen are measured using tube and ball flowmeters. Slight variation in the premixed flow may lead to differences in the unburnt gas exit velocity and gas composition, hence affecting the overall accuracy of the whole setup. Similar flowmeter configuration [53] lists an accuracy and repeatability of $\pm 2\%$ and 0.5% at near full scale reading. Ethylene was kept at low velocities which resulted in significant errors of 9.5% whereas the minimum and maximum errors associated with air variation range from 0.7% to 1.5% . The rated accuracy for the thermal mass flowmeters is $\pm(0.8\%Rd + 0.2\%FS)$. Furthermore, the extensive distance of 5 metres between the cylinders and flowmeters resulted in a pressure degradation of 13.8 kPa. Pressure regulators are installed in placed but are expected to be of the same error magnitude to that of flowmeters.

2.6 Visual Observations

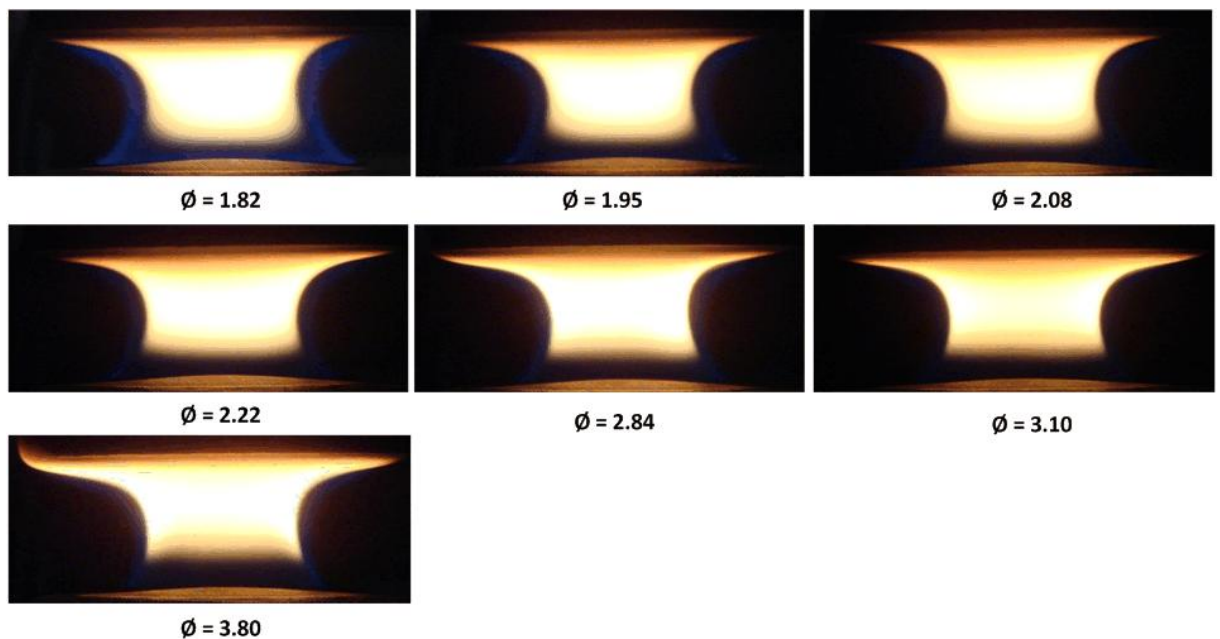


Figure 8 Photographs of stabilised premixed ethylene flames at $\text{Ø} = 1.82$ to 3.80

Figure 8 shows photographs of the stabilised flames at seven flame test conditions using a 30 mm flat flame burner and a 65 mm stainless steel stabilising plate for bluff-body stabilisation. It is observed that flame luminosity begins from HAB 7 mm near burner exit and increases with stoichiometry. The stabilising plate was positioned at HAB 23mm where no visible oscillations are observed. The blue radiation near burner surface at $\text{Ø} = 1.82$ reflects the presence of excited CH radicals in high-temperature zone whereas in richer mixtures such as one in $\text{Ø} = 3.80$, the zone appears blue-green instead due to excited C_2 radicals [45]. Even though nitrogen co-flow gas is employed as a shroud to the premixed flames but in

comparison to the inlet premixed fuel, it is at least 20 times smaller to the least sooty flame ($\phi = 1.82$). Based on visual observations, the flames still remain stabilized. However, the acquired flame images do not reflect much on the soot distribution within the flame. Therefore a secondary procedure is needed to investigate the distribution.

A dark zone can be visibly seen at near burner exit which is suggested to be a region of oxidizing power where the concentration of OH radicals is said to be in excess of equilibrium [54]. In addition, simulation results obtained by CHEMKIN[®] support the above statement where there are high levels of OH radicals at near burner surface in Figure 57. At fuel-rich conditions, the main contributor to soot oxidation would most likely be OH radicals which are more reactive than stable O₂ at temperatures from 1580 to 1860 K at atmospheric conditions [55].

Flame stabilisation is more likely by heat conduction than of nitrogen co-flow. Nitrogen co-flow velocity is kept constant throughout the seven flame test conditions. Due to the low nitrogen co-flow, the unburnt gas mixture is preheated by the burnt gas which causes the adiabatic burning velocity to increase and hence stabilize through heat loss to the burner plate [36, 49]. This results in a large amount of unspecified heat release to the water-cooled burner. Consequently, temperature profiles by thermocouple measurements are significantly reduced in Figure 37. The low unburnt gas velocities can dramatically influence the shape of the temperature profiles [36]. Due to these repercussions, soot volume fraction profiles maybe inadvertently affected.

2.7 Summary

The motivation behind the use of a flat flame burner to generate one-dimensional flames extensively used as calibration benchmarks for temperature and chemical species analysis was looked at. To suppress the conical configuration of a laminar premixed flame, a stabilising plate was used. Seven flame test conditions from $\phi = 1.82$ to 3.80 had shown possibility in this study.

The observed flame images of the stabilised flat flames were consistent with the visual radiation exhibited by excited C₂ and CH radicals. The dark zone near the flame front was hinted to be of OH radicals in excess which is a main contributor to soot oxidation. Low nitrogen co-flow resulted in flame stabilisation by burner plate that inadvertently modified the

temperature profiles. However, the visual observations did not depict much about the soot distributions in the flame.

3 LASER EXTINCTION

This chapter focuses on the theory behind laser extinction and the method of approach to calculate soot volume fractions from incident and attenuated beam intensities. Potential errors involving different refractive indices of soot are reviewed as well. Details about the continuous wave Helium-Neon laser and other components in the experimental setup are briefly explained. Calculated soot volume fractions are arranged as a function of burner heights. The influence of refractive index of soot on soot volume fractions is discussed.

3.1 Foundation of Laser Extinction

Presence of soot can dramatically affect the efficiency and radiant heat transfer profiles in combustion systems. Application of lasers to soot particle measurements is needed to understand the formation and oxidation processes associated with soot formation. One of these methods is *in-situ* laser extinction. Laser extinction has been heavily involved in soot volume fractions measurements in both diffusion and laminar premixed flames alike [2, 13, 41, 56]. The laser extinction (LE) technique typical for combustion systems compose of a laser beam crossing perpendicularly to the flame reaction zone. The interaction between the laser beam and the reaction zone is assumed to be a piece of horizontal cylinder with a constant cross-section [57]. At the opposite end, an optical device measures the intensity of the laser beam thereafter. Laser extinction is based on the beam attenuation theory whereby soot particles within the flame absorb a part of the incident beam. The ratio of the attenuated beam to the incident beam (\bar{I}_T/\bar{I}_O) intensity will yield partial absorbance of the flame which indicates soot volume fraction at that point of time. Soot volume fraction can be calculated using Bouguer's law if soot dimensions are assumed to be within Rayleigh limit for spherical particles ($\pi d_p/\lambda < 0.3$) with respect to incident light source [58, 59]. This line-of-sight method is able to provide instantaneous and non-intrusive measurements over a finite path length through the main reaction zone.

3.2 Soot Volume Fraction by Laser Extinction

Fundamentally, soot volume fraction, f_v can be calculated from the extraction of extinction measurements if the refractive index of soot, $m = n-ik$ is known and that laser pathway, L through the flame is assumed to be a constant zone. This is determined by the following steps:

$E(m)$ as a function of refractive index of soot:

$$E(m) = -Im \left(\frac{m^2 - 1}{m^2 + 2} \right) \quad \text{Equation 3.1}$$

Bouguer's law for light extinction [59] :

$$\frac{\bar{I}_T}{\bar{I}_O} = e^{-K_{ext} L} \quad \text{Equation 3.2}$$

Soot volume fraction obtained from laser extinction:

$$f_v = \frac{K_{ext} \lambda}{6\pi E(m)} \quad \text{Equation 3.3}$$

Where λ is the wavelength of the light source, K_{ext} is the extinction coefficient and \bar{I}_T/\bar{I}_O is a function of the transmitted and incident averaged laser intensity across the assumed homogenous flame reaction zone. The laser path is determined by manual assessment of the luminous flame photographs taken at each condition. Details and description of the laser path methodology is described in APPENDIX A.2. In Rayleigh's regime, soot particles must be less than 60nm and valid within Rayleigh's limit ($\pi d_p/\lambda < 0.3$) where λ is the wavelength of the incident laser beam. Extinction caused by scattering is considered negligible for very small particles in this regime. Based on this assumption, the dimensionless extinction coefficient, K_e equals that of the dimensionless absorption coefficient, K_a , obtained from Mie theory in the limit of small particle sizes as reported [60-62]. This coefficient is a useful optical property that provides a simple relationship between extinction and soot volume fractions [43, 63]:

$$K_a = \frac{36\pi n_\lambda k_\lambda}{(n_\lambda^2 - k_\lambda^2 + 2)^2 + 4n_\lambda^2 k_\lambda^2} = K_e = 6\pi E(m) \quad \text{Equation 3.4}$$

Rearranging Equation 3.4:

$$E(m) = \frac{6n_\lambda k_\lambda}{(n_\lambda^2 - k_\lambda^2 + 2)^2 + 4n_\lambda^2 k_\lambda^2} \quad \text{Equation 3.5}$$

Where n_λ and k_λ are the real and imaginary parts of soot refractive index, m . Equation 5 is only valid for isotropic spheres in a monodisperse system with particle sizes much smaller

than the laser wavelength [7] and is limited by a suitable substitution of the refractive index of soot. Uncertainties pertaining to the incorporation of the appropriate refractive soot index and the assumption of monodispersivity are the two main limitations to the soot volume fraction theory which forms the basis for the subsequent section.

3.3 Potential Errors Associated with Refractive Index of Soot

The accuracy of soot volume fractions measurements based on light extinction approach is questionable in response to the dubious use of appropriate soot optical properties in different situations. A series of refractive index of soot values obtained by different authors is shown in Table 3. Some of these works include: (1) *ex-situ* reflectometry measurements of soot in fuel-lean acetylene and propane diffusion flames by Dalzell and Sarofim [60]; (2) *in-situ* soot measurements in the fuel-lean region of plexiglass/air diffusion flames by Lee and Tien [61]; (3) *in-situ* dynamic light scattering and extinction measurements of soot in fuel-rich premixed methane/oxygen flames by Charalampopoulos and Felske [62]; (4) *in-situ* light attenuation measurements for propane soot by Chippett and Gray [64].

Table 3 Summary of complex refractive index of soot

Authors	Wavelength (nm)	n	k	Ref
Dalzell and Sarofim	632.8	1.57	0.56	[60]
Chippett and Gray	visible	1.9	0.35	[64]
Lee and Tien	visible	1.8 – 2.0	0.45 – 0.65	[61]
Charalampopoulos and Felske	488	1.6	0.6	[62]

There still remain potential issues in the determination of refractive index of soot. The *ex-situ* light reflectance technique applied to soot samples by Dalzell and Sarofim [60] has been greatly criticised by Lee and Tien [61] as surface roughness, as a function of reflectance, presents a potential problem to soot property changes. There are uncertainties involved in the soot particle sizing by Charalampopoulos and Felske [62] as their method is unsuitable for submicronic particles. *In-situ* measurements of Chippett and Gray [64] involved approximation of Drude-Lorentz dispersion model to predict the variation of soot refractive index with wavelength and temperature, has also been employed in other works as well [61, 62]. Despite theoretical and technical differences, the refractive index of soot, $m = 1.57 - 0.56i$ by Dalzell and Sarofim [60] is still the most cited reference in the combustion community for visible wavelengths.

The Drude-Lorentz dispersion model is used to determine soot refractive index and is susceptible to wavelength, temperature and C/H ratio changes [60-62, 65, 66]. This model assumes soot to be of the same order to that of graphite with three bound electrons and one loosely bound electron. The real and imaginary parts of the index n and k may be expressed in terms of the number densities of the bound and free electrons (n_{bj} , n_f), natural frequencies of the bound electrons (w_{bj}) and the damping constants of the bound and free electrons (g_{bj} , g_f) through the dispersion equations as reported by Lee and Tien [61]:

$$n^2 - k^2 = 1 + \frac{e^2}{m\varepsilon} \sum_{j=1}^2 \frac{n_{bj}(w_{bj}^2 - w^2)}{(w_{bj}^2 - w^2)^2 + w^2 g_{bj}^2} - \frac{e^2}{m^* \varepsilon} \frac{n_f}{(w^2 + g_f^2)} \quad \text{Equation 3.6}$$

$$2nk = \frac{e^2}{m\varepsilon} \sum_{j=1}^2 \frac{n_{bj} w g_{bj}}{(w_{bj}^2 - w^2)^2 + w^2 g_{bj}^2} + \frac{e^2}{m^* \varepsilon} \frac{n_f g_f}{w(w^2 + g_f^2)} \quad \text{Equation 3.7}$$

The parameters m and m^* represent the masses of the bound and free electrons respectively with w as the frequency of the incident radiation. The sensitivity of the above equations is limited to main parameters such as number densities of bound and conduction electrons or temperature dependence of the damping constants. Comparison with Dalzell and Sarofim [60]'s model concluded that they did not take into account the effective mass of conduction electrons. Even though their work is the universally accepted refractive index of soot for soot volume fraction in the visible, it was noted that it may result in an overestimation of profiles by one order of magnitude [65].

Application of an averaged refractive index for all heights in the entire flame may result in potential errors. The use of an averaged index at lower heights will result in errors in number density and size. This is attributed to the maturity and size of the soot particle [61, 62]. By altering the refractive index, it also influences the absorption coefficient K_{abs} in such a way that increases the accuracy of the extinction diagnostic technique as well [6]. Clearly, caution should be exercised in applying an average value of refractive soot index to the entire flame due to the changing characteristics of soot for different heights.

Another identified source of error is the use of a constant soot refractive index throughout the flame as soot particles does not usually validate within Rayleigh limit. In order for light scattering to absorption to remain negligible, the primary soot particle diameters must be smaller than 60 nm compared with a source wavelength of 632.8 nm [43]. This assumption is more valid for „young“ soot particles after nucleation which consists of relatively size

uniformity at low and intermediate heights [10, 16]. However in later stages, soot particles undergo intense coagulation and aggregation to form clusters of primary soot particles with a decrease in number density. At this juncture, the size distribution becomes larger with higher carbon content composition [7]. Soot aggregates comprise of hundreds of individual primary particles and the average aggregate dimension may reach up to the same magnitude of extinction wavelength. Under this condition, scattering cannot be assumed negligible. This, combined with uncertainties associated with soot refractive index, may affect the accuracy of soot volume fraction profiles.

3.4 Experimental Description

This section focuses on two parts: Helium-Neon laser and optical chopper. The laser is responsible for the absorbance in the flame whereas the purpose of the chopper is to isolate and separate background noise from laser signal.

3.4.1 Helium-Neon (He-Ne) Laser

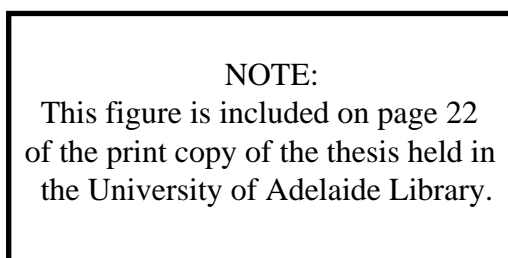


Figure 9 Helium-neon laser (Thorlabs, Inc)

A non-intrusive laser extinction technique is used to determine the soot volume fractions in one-dimensional premixed flat flames. In this technique, a continuous wave Helium-Neon laser of wavelength 632.8 nm shown in Figure 9 is used as the main light source for laser extinction measurements. The specifications [67] (Thorlabs, Inc) detail this laser equipment to produce a minimum output power of 35.0 mW with linear polarization of $500 > 1$. An external housing is used to maintain mirror alignment consistency. The laser head comes equipped with a beam shutter installed at the front bezel of the laser housing for safety purposes.

A custom-made adjustable laser head holder is constructed for stability and vertical height adjustments. Two of these holders are strategically placed at either ends to distribute the

weight of the He-Ne laser. Movements along the vertical axis are also made possible by the use of stainless steel screw rods.

3.4.2 Optical Chopper

An optical chopper is used to produce a square-wave modulation to the laser optical intensity signals so that laser beam intensity signals can be separated from the background noises. The Model SR540 chopper from Stanford Research Systems [68] is able to “chop” light signals at operational rates between 4 Hz to 3.7 kHz.

NOTE:
This figure is included on page 23
of the print copy of the thesis held in
the University of Adelaide Library.

Figure 10 Single beam procedure (Stanford Research Systems)

As shown in Figure 10, the single He-Ne optical beam is “chopped” by the outer row of slots dependent on the set chop frequency. The reference output from the controller is then linked to the lock-in amplifier followed by a data acquisition system. This acts a trigger mechanism for a phase sensitive synchronous detection of small signals due to noise interference [69] in union with the photodetectors. This same configuration is implemented into the laser extinction experimental setup with a lock-in rate of 300 Hz.

3.5 Experimental Layout

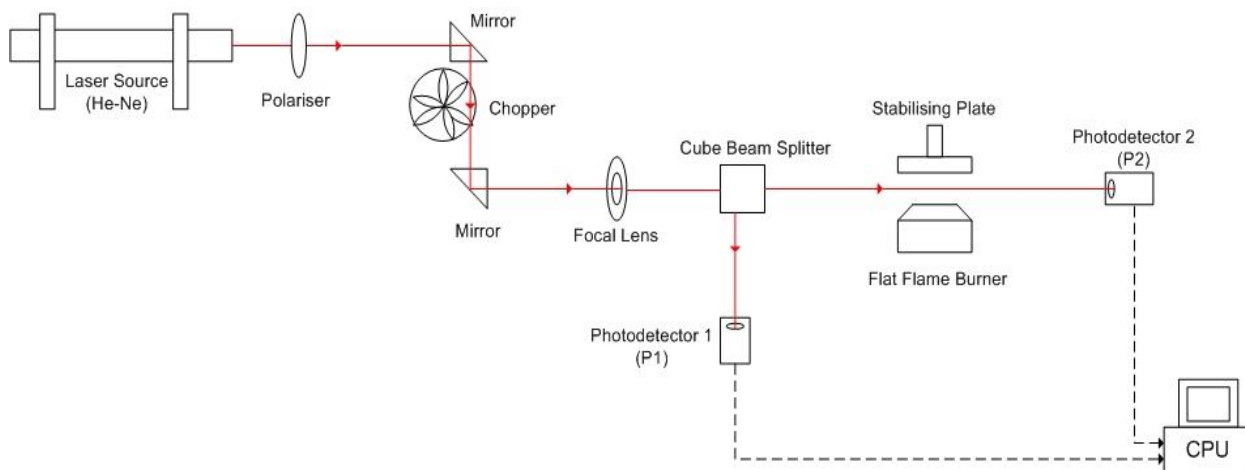


Figure 11 Laser extinction experimental layout

As per experimental layout described in Figure 11, the laser equipment, optics and photodetectors must be adjusted in such a way that optimum soot measurements can be acquired and later tabulated. Starting from the laser beam emittance, a polarizer is placed in front of the He-Ne laser source so that the emerging refracted ray is partially polarized to 25 % transmittance. The mechanical 6-blade chopper is kept at 300 Hz to separate the flame and background emission. It gives an optimal of 3 square modulations within one sweep rate of a 256 sample collection. Due to laboratory space constrictions, a low intensity dichroic mirror is used to deflect the polarized laser source to a simple lens of focal length $f = 50$ mm. This lens is used to focus the polarized beam to near collimated light condition about 1 metre downstream. In addition, a non-polarizing cube beam splitter is used to split the laser into 2 beams for the incident and transmitted photodetectors. The entrance and exit faces of the beam splitter are anti-reflection coated to prevent any unwanted aberration to the nearby optical setup. The splitter provides a split ratio of 30:70 to incident and transmitted photodetectors.

The respective optics is aligned to best conform the laser source to yield a straight line through the top of the flat flame burner at a stationary position. The laser beam diameter after polarization and focusing is measured to be about 1.2 mm in diameter, with a beam energy of 2.2 ~ 2.4 mW. This focused laser source offers a high signal-to-noise ratio and sufficient resolution to spatial time-averaged soot. Movements along the vertical axis are supported by the use of vertical burner traverse. Since stabilised flat flames are one-dimensional in nature, it is assumed that the reaction zone is treated like a constant cylinder. Therefore shifting the traverse sideways will produce radial profiles from -14 mm to +14 mm with an error of ± 0.5 mm deviation.

A large-area in-house built silicon photodiode is used to fulfil the purpose of detecting laser intensities and converting them into electrical signals. They are strategically placed before flame and after flame corresponding to incident and transmitted intensities. In order to prevent ambient light from mixing with the laser source at detection, the detector is fitted with a custom-made sheath with a PVC pipe to prevent unwanted interferences from the surrounding background as shown in Figure 12. The incident photodiode (**P1**) is placed on the same level beside the beam splitter whereas the transmitted photodiode (**P2**) is placed on a platform located about 1 metre away from the burner. In both cases, the laser beam is aimed at the middle of the silicon photodiode for optimum detection.



Figure 12 In-house built photodiode with sheath

The analogue signals from both photodiodes are sent to a lock-in amplifier which is then digitized in real-time on SCOPE [70] for processing. Intensity values through the flame for each burner height are collected at a rate of 4 kHz and continual repetition of two more times for averaging purposes. Background flame noise is measured to be around $\pm 1\%$ of the raw data which is considered negligible. A flameless procedure is carried out for **P2** to compensate for the trade-off as encountered when the laser beam passes through the air as an incident ray prior to experiment. This trade-off is considered in the calculation of soot volume fraction.

3.6 Source of Errors

3.6.1 Data Measurement Errors

Besides the inherent inaccuracy of the flowmeters, there are other unpredictable elements which may affect the combustion performance. One of them is gas composition make-up. Every effort is taken to monitor their measurements. However, slight inconsistencies may still remain in the gas composition as no isokinetic sampling was done on the premixed flames. No temperature analysis was done on the burner plate to determine flame stabilisation via heat conduction [49]. In spite of these factors, the expected uncertainty of the gas composition would be small due to the little variations in the flow meters.

It is identified that deviations in radial distance and laser path through burner centreline are some of the minor elements which may affect actual data measurements. It is observed that a ± 2 mm deviation will result in a 5.5 % difference for radial soot concentration profile at $\phi = 2.84$ at HAB of 15 mm. In addition, laser path lengths are estimated through physical assessment from flame photographs (See APPENDIX A.2). The associated errors with this type of measurement can be estimated to be less than 5 %. Therefore without appropriate consideration to the height and position of these elements, significant errors can affect the final results.

3.6.2 Effect of Laser Variation

Not all measurements made by continuous wave lasers would yield temporal and spatial results in terms of soot volume fractions. Initial investigations into the laser beam profile prior to LE experiments were carried out to determine these deviations and provide suitable explanations.

A flameless procedure as aforementioned in Chapter 3.5 was carried out before each run to determine the incident intensity. It was observed that the incident intensity differed daily. To ensure the smooth operation of the He-Ne laser, the laser was warmed up at least 1 hour beforehand together with the photodiodes. Transmission measurements are obtained by taking the ratio of extinguished and incident laser beams, free from any dependence on the laser optical path length and refractive index variables. Any external fluctuations are accounted for by taking the ratio of the extinguished and incident signals from the photodetectors. Figure 13 shows the He-Ne laser extinction measurements for a mean duration of 1 hour.

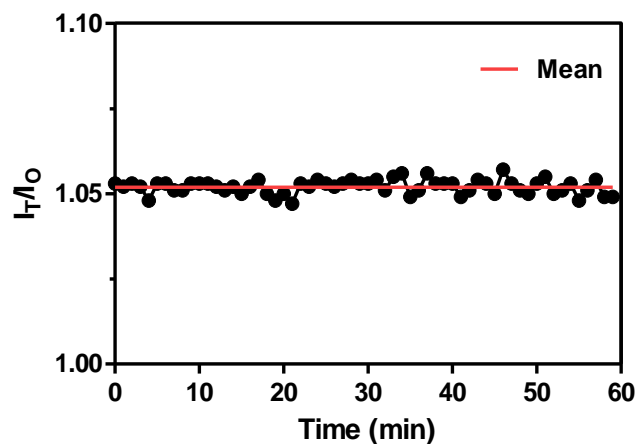


Figure 13 Mean extinction measurements for He-Ne laser for the duration of 1 hour

In comparison to the mean extinction value, the maximum deviation encountered for this type of continuous wave laser is calculated to be within $\pm 0.5\%$. This deviation is insignificant to cause any major changes to the present soot volume fraction profiles in later stages. But at low burner heights between HAB 3 to 5 mm will result in a 3% increase in absorption rate. This, in turn affects soot volume fractions to go below the zero datum.

3.7 Results and Discussions

Experimental work is undertaken to measure the concentrations of soot in laminar premixed ethylene flames by laser extinction. Attenuated and incident intensities of the laser beam are taken from photodiodes. This reflects the partial absorbance of the flame. Thereafter soot concentration or volume fractions are obtained with the help of laser path and refractive index of soot. A range of investigations are subsequently conducted:

1. Observations of soot volume fractions as a function of height above burner (HAB).
2. Comparison of present study's results to similar reported works [2, 7].
3. The variation of the refractive index of soot influencing soot volume fractions.

3.7.1 Soot Volume Fraction Profiles

Laser extinction relies on the assumption that soot particles must be less than 60 nm and are within Rayleigh's limit ($\pi d_p/\lambda < 0.3$) with respect to the incident light source. Extinction measurements (\bar{I}_T/\bar{I}_O) are acquired by taking the ratio of the transmitted and incident laser intensities. These transmission elements are independent from optical path length and refractive index variables. Extinction results derived from these experiments seems to be decreasing as a function of burner height which reflects the sooting tendency per flame condition. With the inclusion of the widely cited refractive index of soot, $m = 1.57 - 0.56i$ [60], soot volume fractions can thus be determined. The calculated results profiles are tabulated in APPENDIX C.1.

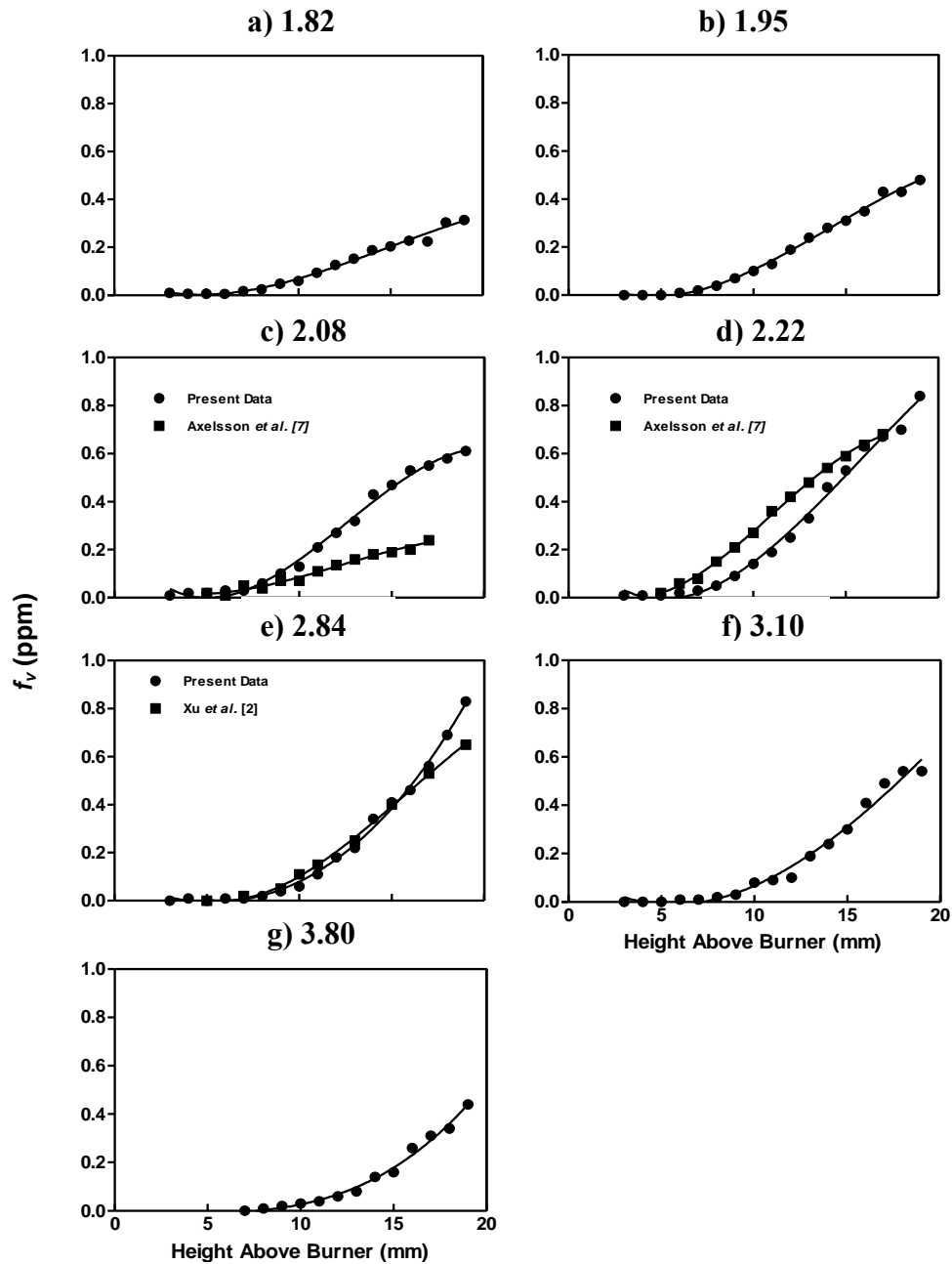


Figure 14 Soot volume fraction profiles (Axial) by LE at $\text{Ø} = 1.82 - 3.80$; symbols: measurements; lines: third-order polynomial fit

The calculated soot volume fractions are arranged with respect to height above burner. In this way, the profiles or trends can be observed. Figure 14 shows the axial profiles of the mean soot volume fraction, f_v as a function of height above burner in each of the investigated flame test conditions. Non-linear regression least square trend lines are fitted within 95 % confidence limit to best suit the data measurements. A small part of the total soot volume is exhibited in the lower HABs due to the soot nucleation process; however surface growth reactions can be seen predominant in higher HABs. It is also observed that the magnitude of these soot concentrations increase with sooting propensity when Ø reaches 2.22 but decreases

with respect to heavier sooty flames i.e. ϕ greater than 2.84. For this scenario, soot production rate is limited by the influence of OH radicals. OH radicals, which are far more reactive than O_2 , strongly support the oxidation process of removing the carbon element away [55]. With the absence of OH oxidation, the expected break-up of the soot will be minimized and hence a decrease in particle number will result in lower detection values. This is confirmed by thermophoretic sampling in Figure 45 whereby mean primary particle diameters at fuel-richer conditions approach nearer to 60 nm in size. At these rates, there is a possibility of Rayleigh scattering.

One important aspect of LE is that it fails to take into account of the soot distribution in the flame. Laser extinction procedure measures the transmission values across a defined optical pathway through a flame regardless of premixed or diffusion structure by Bouguer's law (Equation 2). The differences in soot distribution as shown in Figure 27, conducted by laser-induced incandescence (LII) two-dimensional imaging can affect the accuracy of soot volume fraction profiles. Soot distributions range from a fully premixed structure from $\phi = 1.84$ to 2.22 to annular structure at richer conditions for ϕ greater than 2.84. Soot volume fraction calculations (Equation 3) cannot be applied to fuel-richer conditions as the flame medium is non-homogenous even though visual inspection suggests otherwise (See Figure 8). Thereby employing LII procedure prior to LE to determine soot distribution uniformity, a feasible assessment can be done to foresee which flame conditions are suitable for LE.

Comparisons of the soot axial profiles are carried out for similar conditions to previous studies [2, 7] as shown in Figure 14 (c) to (e). The overall trends of the 3 profiles conform to the least square non-linear regression fit which suggests that soot surface growth is expected dominantly from HAB 7 mm onwards. One can see the slight difference in the values of HAB involved. Present soot concentration values at $\phi = 2.84$ are within agreement to Xu *et al.* [2] but deviations can be seen for Figure 14 (c) and (d) at higher HABs for Axelsson *et al.* [7]. These deviations can be possibly attributed to two factors: One is that a single soot particle undergoes significant structural changes and leading to changes in chemical composition and refractive index [2]. The other explanation is that slight variations in the burner velocity and/or equivalence ratio would bring about major differences in the soot distribution. In this present study, a 30 mm diameter porous burner was used as the main combustor to produce similar flames to that of Axelsson *et al.* [7]. The significant differences in Figure 14 (c) can be attributed to the use of the refractive index of soot, $m = 1.56 - 0.46i$ [7]. This inappropriate use of index produced an error difference of up to 25 %. Therefore the standardization of the

refractive index of soot is important for the evaluation of the scattering-extinction measurements.

3.7.2 Influence of Refractive Index on LE profile

The differences in the refractive index of soot, m can have a profound impact on the soot volume fractions. These differences can be attributed towards particle size, aggregation properties and a constant refractive index throughout the flame. Soot particle properties changes with flame height, for example a nucleated soot particle at low heights have high hydrogen content whereas an aged particle is dehydrogenated [71]. In addition, fuel equivalence can have a substantial effect on the soot agglomeration process and hence affect the refractive index of soot. Specifically, a rise in the equivalence ratio can increase the real part of the index by up to 22 % whereas the imaginary part by 39 % [66]. Besides the agglomeration and fuel composition elements, it is also anticipated that the use of a constant refractive index of soot in the entire flame may generate uncertainties in the soot volume fraction calculations [6].

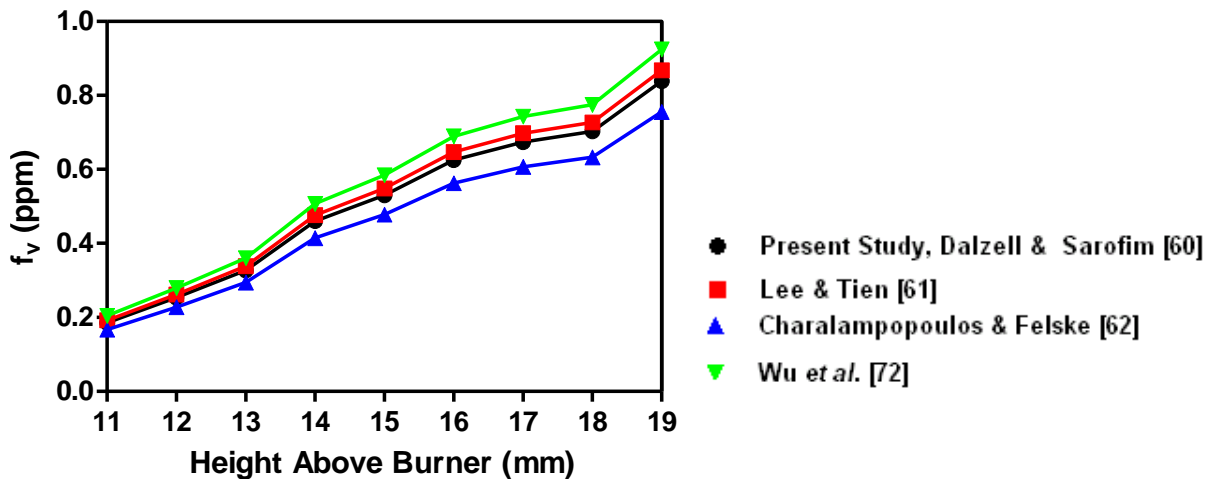


Figure 15 Effect of different refractive index at $\phi = 2.22$

A comparison study on the incorporation of different refractive index of soot into the soot volume fraction profile at $\phi = 2.22$ from HABs 11 mm to 19 mm is shown in Figure 15. In-depth indices' determination details and their potential errors are described earlier. This present study uses the commonly cited refractive index of soot by Dalzell and Sarofim [60] of $m = 1.57 - 0.56i$. It was observed that the implementation of Chippett and Gray's refractive index [64] overestimate soot volume fractions by a factor of two. Instead, Wu and co-workers [72] conducted *ex-situ* scattering measurements in fuel-lean conditions of various fuels for visible wavelengths (350 – 800 nm). Their refractive index of soot of $m = 1.71 - 0.53i$ is used

here as comparison instead. It is apparent from Figure 15 that a slight change in the m value brings about a 3 – 11 % change in the soot volume fraction profile. While the $E(m)$ results of Lee and Tien [61] are 26 % lower than that of Dalzell and Sarofim, the soot volumes fractions produce a 3.4 % increase over the original. The highest difference seen here is Charalampopoulos and Felske [62] with a difference of 11.1 %. This is due to the sensitivity of the imaginary part of the refractive index, k [66]. The imaginary part is highly impacted by temperature changes, wavelength excitation and equivalence ratio and may range by up to 39 % for the same position in the flame.

Soot optical properties may change due to their inherent nature to undergo surface mass growth and agglomeration. For the optimum laser extinction soot measurements, soot particles must be less than 60nm and valid within Rayleigh's limit. In some cases, light incident attenuation upon particles on the leeward side of the agglomerates is caused by blockage of particles on the forward side [4, 5, 73]. This effect is known as the beam shielding effect which may cause variations in the K_{ext} value. It was pointed out by Chang and Charalampopoulos [74] that agglomerates consists of primary particles with varying sizes and that the inferred indices are more of „effective“ refractive indices. This has been proven with the aid of electron micrographs at the same condition (See Figure 44) which reflects that soot particles are spherical in shape in the early stages of soot formation before agglomeration starts to develop. The presence of agglomerates at higher HABs is predominant and thus affects validation of Rayleigh's limit. Also, it is clear from these observations that the same refractive index of soot cannot be used throughout the flame as the primary particles increase in diameter and normally cluster to form agglomerates. By introducing a variable refractive index [6], errors for scattering and number density are compensated. In this study, a constant refractive index, $m = 1.57 - 0.56i$ is applied for this present study and may expect a difference by a factor of two.

3.8 Summary

Measurements of soot concentrations in flat flames were achieved by passing a continuous wave visible laser beam through a constant flame reaction zone commonly referred as laser extinction. On the basis that soot particles are within Rayleigh limit ($\pi d_p / \lambda < 0.3$), soot volume fraction profiles can be obtained via Bouguer's law for laser extinction across a finite path length, L . The most commonly cited refractive index of soot, $m = 1.57 - 0.56i$ [60] was used here. Results from soot volume fraction profiles gave rise to the following observations:

-
- 1) Axial profiles exhibited a small change at lower HABs probably to the soot nucleation process but surface growth was seen to predominant at later stages. In contrast to fuel-rich conditions (ϕ greater than 2.84), the soot distribution deviated from fully premixed to annular structure as confirmed by laser-induced incandescence.

 - 2) The use of various refractive index of soot generated differences from 3 to 11 % in soot volume fractions. Another uncertainty associated with laser extinction was that soot particles, consisting of agglomerates at higher HABs, exhibited a beam shielding effect which may cause variations in the extinction/scattering values.

Nonetheless, laser extinction proved to be a simple but yet responsive technique for measuring soot volume fraction in one-dimensional flat flames.

4 LASER-INDUCED INCANDESCENCE

Another laser diagnostic technique suitable for determining soot volume fractions in laminar premixed flames is laser-induced incandescence. Literature reviews behind this technique are extensively reported for its laser fluence dependency, temporal decay and calibration method against laser extinction to yield soot volume fractions. Comparisons of both techniques, axial and radial profile, are also considered.

4.1 Theoretical Basis

Laser-induced incandescence involves the heating of an energy-absorbing soot particle using a high-energy laser. This method dramatically alters the particle's temperatures to levels far above ambient and emit increased amounts of gray/blackbody radiation by several orders of magnitude [75]. This phenomenon is termed as laser particulate incandescence or rather commonly known as laser-induced incandescence (LII). The main attraction of this technique is that it is able to provide spatial and temporal quantitative measurements with a simple use of a high-energy pulsed laser coupled with suitable photodetection equipment. LII can be applied either as a point, line or two-dimensional laser sheet detection. The LII signals from photodetection are typically calibrated to various *in-situ* and *ex-situ* methods such as laser extinction [2, 6, 8, 12, 76] and gravimetric sampling [77] to determine soot volume fraction. Sometimes, exposure to a high-energy pulsed laser can lead to changes soot morphology which can be explained by a thermal annealing mechanism [78]. The LII technique may also been applied to size up primary soot particles as well [78-80]. A typical approach to the LII experimental setup is shown in Figure 16.

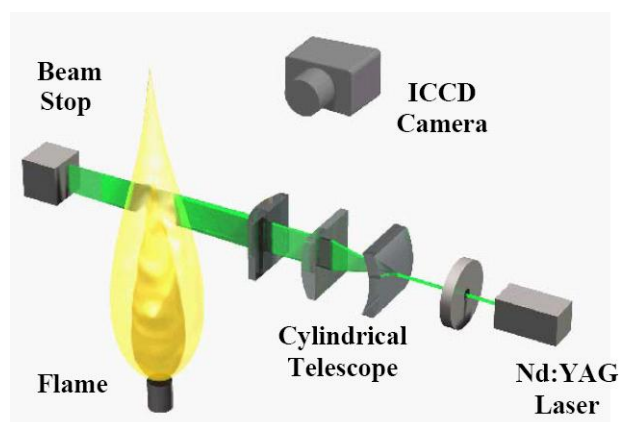


Figure 16 Schematic diagram of the optical arrangements for 2-D LII measurements [81]

The generation of a LII signal is the result of an “intricate thermo-optical phenomenon”, which is complicated by dependencies on parameters such as particle size, particle temperature, surrounding ambient temperature, laser energy intensity and laser beam profile. [59]. This interpretation of the LII signal can be modelled by the use of an energy balance on a single soot particle. The energy equation describes the heat transfer between the particle and its surroundings as well as interaction with the incident laser radiation. It also relates the absorption and loss of energy through convection, radiative and vaporisation as reported by Santoro and Shaddix [59]:

$$m_s \frac{d(c_s T_s)}{dt} - \frac{H_V}{M_V} \frac{dm_s}{dt} = q C_{abs} - h A_s (T_s - T_\infty) - \int_0^\infty 4 C_{abs} E_{b,\lambda}(T_s) d\lambda + \int_0^\infty 4 C_{abs} E_{b,\lambda}(T_w) d\lambda \quad \text{Equation 4.1}$$

The individual terms identified on the left-hand side are: 1) The rate of energy stored in the particle and 2) Loss of particle energy due to vaporisation whereas the right-hand terms are: 1) The rate of absorbed energy from laser pulse, 2) Collisional convective cooling rate, 3) Radiative emission, 4) Radiative Absorption. Further explanations into the analysis of the individual terms are as described [59]. In other words, given a temporal profile of the laser pulse, q , the time-dependent particle size inferred by surface area, A_s , and the particle temperature, T_s , can be solved.

4.2 LII Considerations

One important consideration used in the fundamentals of laser extinction also applies to LII as well. It is the assumption that primary particles must lie within Rayleigh scattering regime ($\pi d_p / \lambda < 0.3$). It is in this condition that soot particles are able to absorb the incident light in proportion to their volume [59]. However, as soot particle sizes in flames can range from individual particles of less than 15 nm up to large aggregates, the above assumption of radiative absorption cannot be held true. Therefore Melton’s model [15] has shown that the peak of the LII signal intensity is proportional to:

$$\text{Prompt LII} \propto N_p d_p^x$$

Where d_p is the mean soot particle diameter and exponent x is $(3+0.154/\lambda_{det})$. For detection wavelengths, λ_{det} between 400 and 700 microns, Melton’s parameter approaches to 3. As a result, the LII signal provides an approximate proportionality to the volume fraction of the absorbing particles. It is this simplistic approach that the LII technique is the much preferred method for soot detection in practical combustion systems.

Another consideration in LII is the selection of suitable wavelengths for incident light. Studies have been conducted wherein the wavelength used to excite LII signals, has been varied from ultraviolet to infrared [9]. There is some indication that fluorescence from laser-produced C₂ radicals from soot vaporisation shows good agreement with soot volume fractions. However, to avoid fluorescence interference from polycyclic aromatic hydrocarbons, wavelengths in the ultraviolet region must be avoided. The emission spectra of C₂ radicals from aromatics showed relative line intensities for wavelengths at 266, 355 and 532 nm [82]. The Swan bands, in resonance with C₂ radical emission spectra, have been known to occur in the wavelength region between 420 to 620 nm [11, 13]. Also, if a short wavelength is used, the LII signal would be biased towards particles with higher temperatures due to particle size [15, 83]. Nevertheless, for most LII experiments either the fundamental wavelength of 1064 nm [12, 84] or the second-harmonic wavelength of 532 nm [7, 8, 10, 85] of a Nd:YAG laser has been often cited as the main source of particle excitation.

To negate the primary particle size and local gas temperature gas differences in any LII measurements, signal integration beginning with excitation intensity or prompt gating is preferred [7, 15, 83]. Any delay in the detection gate will bias the LII measurements in favour of large particles [83]. On top of that, fluorescence interference from PAH species may contribute to the LII signal [59]. Thus the approach of prompt gating is ideal for the detection of LII signals.

Although not a major prerequisite to the LII considerations but it is noteworthy to observe that soot particles under high volume of heating may result in physical and optical changes. Several efforts have been carried out by Vander Wal and co-workers [78, 86, 87] to examine the effects of LII excitation process on soot particle morphology. TEM micrographs reveal physical changes in laser-heated soot for all laser fluences via thermophoretic sampling in Figure 17. These physical changes i.e. formation of shell-like structures, can alter the radiative and cooling characteristics [86] of the laser-heated soot but such effects do not seem to affect the capabilities of the LII process. Conversely, primary particle size determination under high laser intensities does raise some concerns about the induced morphological changes which are often inferred by a thermal annealing process [78]. This may pose a potential source of error to the theoretical modelling of the LII signal where optical properties may vary in such a manner.

Figure 17 TEM micrographs of laser-heated soot captured via thermophoretic sampling. Values of the laser fluence were a) 0.15, b) 0.3, c) 0.6 and d) 0.9 J/cm² [87]

4.3 Laser Intensity Profile

The intensity of the LII signal is dependent on the temperature of the laser-heated soot which is determined by the rate of laser energy absorption and heat losses through the following mechanisms of conduction, radiation and vaporisation [85]. Previous work has shown that LII signals to increase linearly with laser intensity until a point where soot particles experience significant mass loss due to vaporisation at a peak laser fluence of $\approx 0.2 \text{ J/cm}^2$ at 532 nm [88]. Further increase in the laser fluence will show little or no change in the LII signals. For laser fluences below the saturation threshold, the absorbed laser energy is solely used to raise the soot particle temperature, resulting in relatively weak LII signals whose magnitude is strongly dependent on the laser fluence [59]. As the laser fluence approaches the peak temperature above 4000 K, the main heat loss mechanism occurs through vaporisation [15]. At this point, LII signal is heavily influenced by the laser fluence around the vaporisation threshold [11-13, 85].

Fluence dependence for a Gaussian beam profile shows a rapid rise in the LII signal followed by a “plateau” or levelling region where the gradient of the curve is significantly less than that

at lower laser fluence values. This dependence effect can be seen in Figure 18 for a Gaussian beam profile over a range of incident laser fluence values up to 10 J/cm^2 . In principle, an increase in the laser fluence would result in a rapid rise in the soot incandescence until the particles begin to vaporize. The peak temperature of the soot remains approximately constant regardless of increasing laser fluence which accounts for the levelling-off. Eventually, the profile experiences a constant decay rate due to mass loss by vaporisation and results in a reduction in radiation being emitted over the duration of the detection sampling time. Others [7, 12, 83, 85] have observed the same trend of using a Gaussian beam profile but instead occur with a slightly steadier “plateau” region than that in Figure 18. This constant “plateau” behaviour is explainable by the enlargement of the sampling volume influenced by the increase in particle number [13]. Therefore it is desirable to operate the laser fluence at saturation regime as the LII signal would be least affected by the laser beam attenuation across the flame [83].

Figure 18 Fluence dependence of LII measured in steady laminar diffusion flames. Data were collected at $H = 20 \text{ mm}$ in the ethylene/air flame for detection gate durations of 19ns (+) and 85ns (\diamond), both gates opening coincident with the arrival of the $\approx 5\text{ns}$ laser pulse. Data also shown for the methane/air flame at $H = 50\text{mm}$ with the 85ns gate (\bullet). Raw signals for each condition have been normalized to a value of 1.0 at a fluence of 0.6 J/cm^2 . The solid line shown is the least-square power-law fit of the methane data for fluences greater 0.3 J/cm^2 ; the fit follows the expression $\text{signal} \propto \text{fluence}^{0.34}$ [13]

4.4 Time-Dependence Profile

Another notable feature of the LII technique is the time-resolved LII signals. During the onset of laser irradiation, soot particles are quickly elevated to incandescence temperatures over 4000 K. At this moment, the soot particles start to vaporize followed by a significant reduction in particle mass. This is continued by conductive and radiative heat losses to the ambient gas which results in a gradual decay rate of the LII signals as shown in Figure 19.

Figure 19 Temporal profile of a LII signal obtained in the ethene-air laminar diffusion flame at heights of 10 and 30 mm above the fuel tube exit and at the radial locations corresponding to peak soot volume fraction for these heights [85]

The temporal variation of the LII signals is qualitatively similar to the LII response function for an idealized laser pulse computed by Melton [15]. There is an immediate but almost identical LII signal increase for all heights shown which is consistent with Tait and Greenhalgh's prediction [89] regardless of particle size. However, LII signals at the lower height exhibit a faster decay rate to those obtained at a higher height of 30 mm. This is attributed to the difference in particle diameter [85] as smaller particles, with a larger surface area per unit mass, cool down faster. Similarly for higher laser fluences, an increased magnitude of vaporisation would result in significant larger surface area-to-volume ratio cooling and lower heat content [85].

4.5 Calibration via Laser Extinction

LII measurements are quantitatively analysed through the calibration of signals. They are usually performed by comparing photodetection signals to soot volume fraction obtained by laser extinction [2, 6-8]. In some instances, gravimetric soot sampling has been used as the main medium to calibrate LII signals [76, 77]. In order to derive soot volume fractions from

laser extinction, tomographic inversion of the extinction data is required to yield the soot volume fraction distributions. This procedure proves to be a simple and time-consuming process. The use of a single point calibration at mid-heights is often used to derive soot volume fractions [9, 12, 13]. But this method tends to underestimate values at low heights by up to 10%. This is attributed to the increased sensitivity of LII technique and smaller ranges of primary particle sizes at mid-heights [59].

On the contrary, it is preceded in previous articles [2, 6-8] not only did they not investigate the effects of soot distribution but also ignored the possible effects of polycyclic aromatic hydrocarbons (PAHs) interference on the calibrated soot volume fraction using laser extinction. This may result in an overestimation on the soot volume fraction profiles by an order of magnitude. Bengtsson and Alden [10] concluded that the presence of PAHs at low burner heights emit strong fluorescence signals and increases with C/O ratio. Several studies carried out for laser extinction are based a universal agreement that soot particles absorb strongly in either 532 nm [7, 8] or 633 nm [2, 43, 56] wavelength configuration. However, no local study is undertaken to investigate the role of PAHs in the 1064 nm region using the same experimental means.

4.6 Experimental Description

This section covers the Nd:YAG laser specifications and photodetection equipment used to “capture” soot incandescence.

4.6.1 Neodymium-Doped Yttrium Aluminium Garnet (Nd:YAG) Laser

The purpose of a high-intensity laser beam in laser-induced incandescence is to elevate soot particles’ temperatures to incandescence levels thereby allowing photodetection using an intensified CCD (ICCD) camera. The use of a fundamental 1064 nm laser line was often cited as an approach to eliminate interferences such as C₂ from LII excitation process [12, 13]. However, this method proved to be dangerous to this current practice as the beam is invisible and difficult to alignment. Therefore the other option of using a pulsed laser to produce a second harmonic wavelength of visible wavelength at 532 nm is utilised instead. This is achieved through the use of a Nd:YAG laser (Model Brilliant B Nd:YAG Twins) [90] shown in Figure 20. The output of the laser beam ($\lambda = 532$ nm) is generated with a Gaussian beam profile of approximate 9 mm in diameter with a flash lamp frequency of 10 Hz. Pulse duration for all experiments is performed at 5 ns.

NOTE:
This figure is included on page 40
of the print copy of the thesis held in
the University of Adelaide Library.

Figure 20 Model Brillant B Nd:YAG Twins [90]

4.6.2 Two-Dimensional Photodetection Equipment

The photodetection or imaging of soot incandescence is done using a combination of a 16-bit ICCD camera and interference filter of $410 \text{ nm} \pm 10 \text{ nm}$ bandwidth to minimize potential background and flame interferences.

The 16-bit PI-Max ICCD camera from Princeton Instruments/Acton [91] is used in the spectroscopic detection of soot incandescence. It is widely used as an imaging device for time-resolved measurements in low-lighting conditions. The ICCD camera consists of an intensified tube, coupled via a fiber optic taper as depicted in Figure 21. The camera also consists of both high voltage gating and timing controls for the intensifier as well as low noise CCD readout circuitry. It is linked to a desktop computer where its input settings and output data acquisition can be done remotely.

NOTE:
This figure is included on page 40
of the print copy of the thesis held in
the University of Adelaide Library.

**Figure 21 High performance camera use fiber optic taper/face plate (B) to couple the intensifier (A) to the
CCD (C) [91]**

In the selection of a suitable spectral bandwidth over which incandescence measurements can be made, an optical filter of 410 nm with a 10 nm bandwidth shown in Figure 22, is employed to reduce C_2 emission interferences. As previously mentioned, the C_2 radical emission interference spectra is known to occur in wavelength ranges between 420 to 620 nm [11, 13]. Therefore the use of narrowband filters of transmission wavelengths less than 450 nm will

beneficially reduce these C_2 emission interferences. This filter is coupled to the lens of the ICCD camera with the front side (blue), facing the flame.

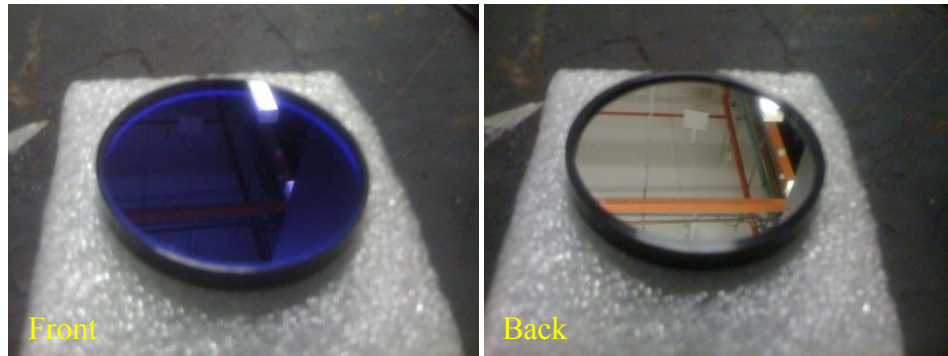


Figure 22 Interference filter of $410 \text{ nm} \pm 10 \text{ nm}$

4.7 Experimental Layout

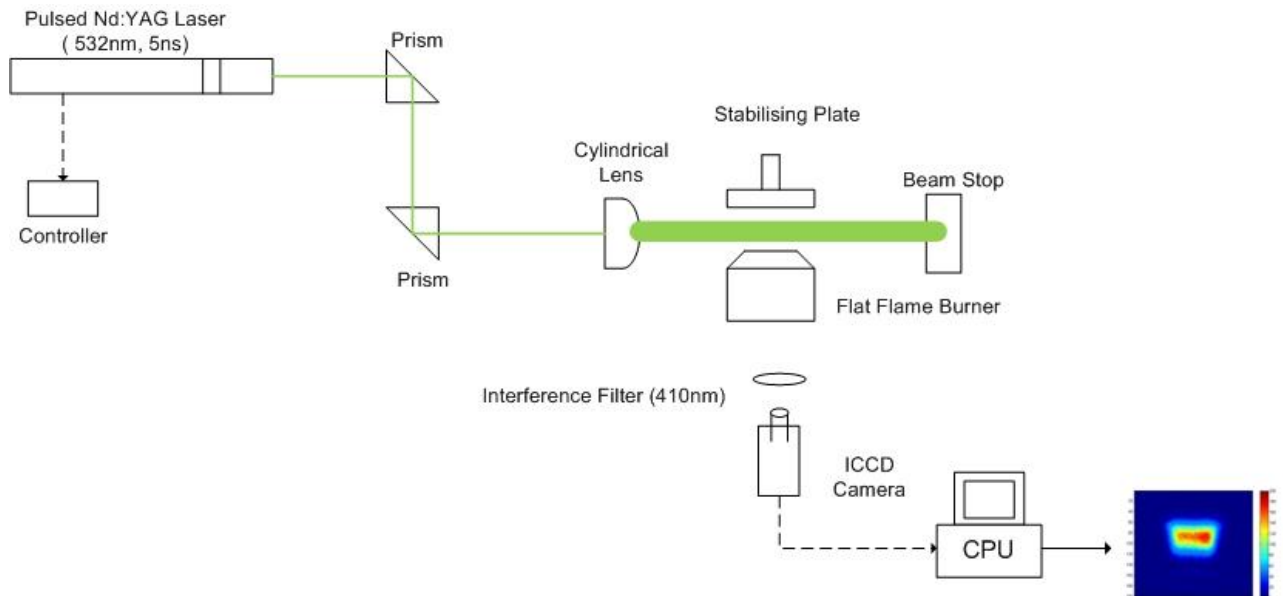


Figure 23 Laser induced-incandescence experimental 2-D layout

The placement of the pulsed Nd:YAG laser, optics and ICCD camera are strategically positioned so that temporal and spatial resolution of the soot incandescence signals is achieved with minimum flame disruptions as shown in Figure 23. Flashlamp for the Nd:YAG laser is warmed up for a duration of 1 hour prior to Q-Switch pulsating. The 2nd harmonic output ($\lambda = 532 \text{ nm}$) of the pulsed laser is directed to a high-intensity mirror whereby the beam is deflected onto a cylindrical lens with a focal length of $f = 2000 \text{ mm}$. A vertical, polarized laser sheet of 15 mm high and $\sim 1 \text{ mm}$ thick is produced. This polarized sheet, as main detection medium, passes through the central zone of the stabilised flames (HABs = 5 mm to 20 mm). A beam stop is placed at the end of the laser path to prevent laser scattering.

To compensate for the weaker laser intensity at both ends of the vertical sheet, about 2 mm of either side is neglected.

To determine the peak LII intensity at which laser fluence can be operated with minimum beam attenuation, the laser fluence is measured using a calibrated power meter (Model Solo 2) and detector (Model UP19K-15S-VM) [92] with 0.75 mV/W sensitivity and $\pm 0.5\%$ of full scale accuracy. It is observed that the highest LII signal for a Gaussian beam produced by the Nd:YAG laser corresponds to a laser fluence of 2.91×10^8 W/cm² for a 9 mm diameter laser beam diameter operating at a frequency of 10 Hz with a pulse duration of 5 ns.

After exposure to the pulsating laser, soot incandescence is captured in the form of two-dimensional images. Images are recorded with a gated ICCD camera [91] coupled with an interference filter of 410 nm \pm 10 nm bandwidth, aligned perpendicular to the burner at a safe distance of 1 metre. In order to improve signal-to-noise ratio, prompt gating (delay \approx 0 ns) is employed with a gate width of 20 ns to coincide with the arrival of the laser pulse. A gain of 200 is applied to increase the ICCD camera sensitivity bias towards LII signals to compensate for the background noise. Flame fluctuations are compensated by accumulating 20 individual sheet images into one single sheet. For each set of burner height per flame test condition, 20 straight images are taken which results in a total accumulation of 400 sheets, 300 by 200 pixels. The images are extracted out using WinView 32[®] [93] as image files (TIFF). A treatment of these image files converted into relevant intensity values is summarised in APPENDIX A.5.

4.8 Sources of Error

4.8.1 Image Processing

From the two-dimensional images obtained by LII, it is necessary to apply some form of processing before analysis and calibration can be done. The processing procedure is outlined in APPENDIX A.5 which involves background deduction, dark charges and averaging. These values are later normalized to a single-point calibration at $\emptyset = 2.22$ of HAB 11 mm. Regardless of the above procedure, potential errors may exist due to the range of primary particle size and LII experimental sensitivity. Careful consideration is taken to ensure that the appropriate values are rightfully calibrated.

4.8.2 Laser Fluence Consistency

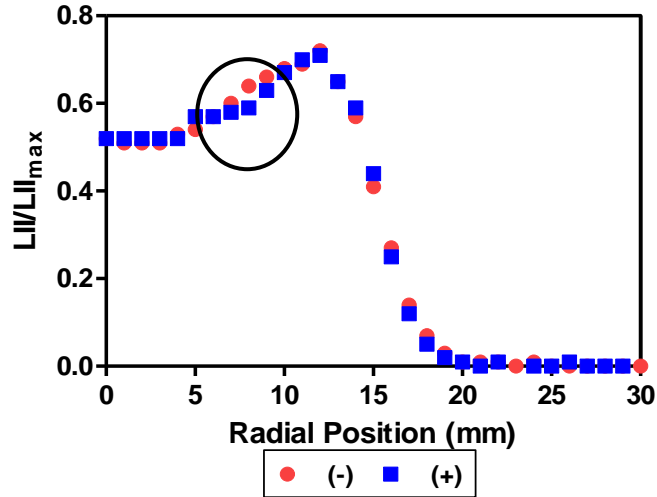


Figure 24 Comparison of LII beam profile at $\text{Ø} = 2.22$ at HAB 11 mm as function of radial position
(Note: (-) & (+) denotes laser entry & laser exit)

Figure 24 compares the LII beam profile at $\text{Ø} = 2.22$ of HAB 11 mm across the stabilised flame upon laser entry (-) and exit (+). At this particular condition, the LII signals are at its highest but still maintain relative constant flame uniformity. As observed, there is an excellent agreement between the laser entry and exit within $\pm 5\%$ but there are still slight variations at 8mm towards laser exit (+). The slight increase in the LII signals at laser entry may result in a slightly higher intensity at laser entry for the radial profile. Nonetheless, this does not have a major impact on the overall soot volume fraction behaviours.

4.9 Results and Discussions

Photodetection of soot incandescence in laminar premixed flames via laser-induced incandescence is performed. Captured two-dimensional images from the ICCD camera are processed using a custom-written programme (Matlab[®]) to decipher and extract LII intensity values from each image. These values are calibrated to $\text{Ø} = 2.22$ at HAB 11 mm of laser extinction to yield soot volume fractions for comparison. Other investigations may include:

1. Measurement of LII intensities against laser fluence and detection gate delay at $\text{Ø} = 2.22$.
2. Observations of soot distributions from $\text{Ø} = 1.82$ to 3.80 based on instantaneous two-dimensional images and normalised radial profiles.

-
3. Direct comparison of axial and radial soot volume fraction profiles for both laser extinction and laser-induced incandescence in all flame test conditions.

Based on the above observations, the optimal conditions for laser extinction measurements are identified. Calibrated soot volume fractions are tabulated in APPENDIX C.2 as a function of HAB from 7 to 15 mm.

4.9.1 Fluence Dependence

Typically for nanosecond laser pulses, soot particles in the range between 10 to 200 nm with temporal detection gates longer than laser pulse duration, the only factor that determines power dependence is the integrated laser intensity over the pulse duration [13]. This is termed as laser fluence (W/cm^2). It is influenced by the temperature of laser-heated soot particles which is dependent on the rate of laser energy absorption and heat loss through conduction and vaporisation.

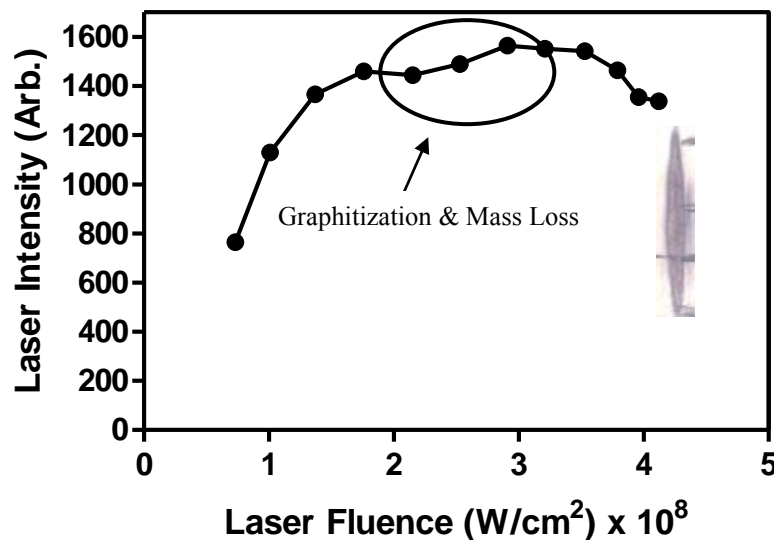


Figure 25 LII signal (Arbitrary) as a function of laser fluence at $\varnothing = 2.22$ of HAB 11 mm; insert: burnt image at laser fluence of $2.91 \times 10^8 \text{ W}/\text{cm}^2$

Figure 25 represents the average LII intensity values as a function of varying laser fluence at $\varnothing = 2.22$ of HAB 11 mm. The laser fluence was determined with the use of a calibrated power detector and meter. A steep incline is observed at low fluences followed by a levelling-off “plateau” as fluence increase before gradually decreasing. This same phenomenon has too been observed for a Gaussian beam profile in several articles [12, 83, 85]. As the laser fluence increases, the incandescence from a single particle exhibits a sharp rise in its temperature until

vaporisation point. This point is illustrated as the peak in Figure 25 as the temperatures remain constant regardless of laser fluence. Soot vaporisation is the dominant effect that limits the increase in soot particle temperature. This peak temperature corresponds to the laser fluence of $2.91 \times 10^8 \text{ W/cm}^2$. A single shot of the pulsed laser on a litmus paper, passed through the burner centreline, is shown in Figure 25 (insert) corresponds to this peak laser fluence. Further increase in the laser fluence will result in the gradual decrease of the LII signal due to mass loss by vaporisation, effectively reducing the particle mean volume and the amount of emitted radiation over the detection period. At this juncture, conduction determines the temperature decay trend.

Near the “plateau” region, the LII signal experiences a slight drop regardless of increasing laser fluence as pointed out by the red circle in Figure 25. This occurrence can be explained via soot graphitization and mass loss. At high energy levels, unusual shell structures are observed [86] which may alter the radiative characteristics of the soot particle. This results in a lower LII signal despite linear increase in energy levels.

4.9.2 LII Signal Temporal Decay

Decay curves depict information about particle diameters’ cooling rates and their response to temperatures. They closely relate to the estimation of the particle size from vaporisation limit with smaller particles exhibiting faster cooling or decay rates. The decay profile is generated by varying the detection gate delay timing from 0 to 300 ns.

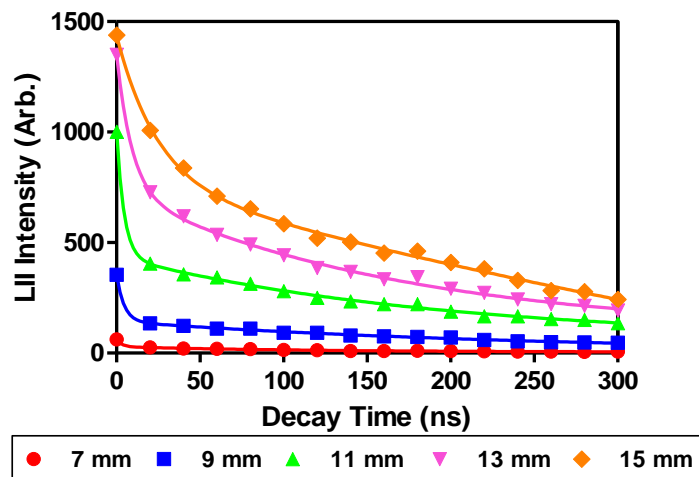


Figure 26 Time dependence of the LII signals as a function of HAB at $\varnothing = 2.22$; symbols: measurements; lines: second-phase exponential fit

A temporal decay profile of the LII signal as a function of burner heights for flame condition at $\varnothing = 2.22$ is shown in Figure 26. For the peak laser fluence of $2.91 \times 10^8 \text{ W/cm}^2$, the LII

signal reaches its maximum just after the laser pulse which is then followed by a long decay as time progresses. This same rapid response was also observed in Melton [15] for a single carbon particle diameter of 20 nm at 100 MW/cm². The dramatic drop in the LII signals after peak is due to a size reduction of primary particles by vaporisation, hence increasing their surface area per unit mass and thereby cooling faster [85].

However, conclusions cannot be drawn regarding the possible effects of particle size, chemical composition or aggregate morphology solely based on the temporal decay profile. The only indication in Figure 26 is that the size of the soot agglomerates becomes larger as height increases. The long decay region at higher HABs reflects slower decay gradient than those at lower burner heights. This is due to the differing ranges and sizes of the soot agglomerates after vaporisation which is related to the degree of conductive and convective cooling thereafter [85]. Thermophoretic sampling at the same condition identifies the varying degree of particle agglomeration in Figure 44. Chemical composition of these agglomerates is undetermined as no probe sampling was carried out.

4.9.3 LII Instantaneous Images

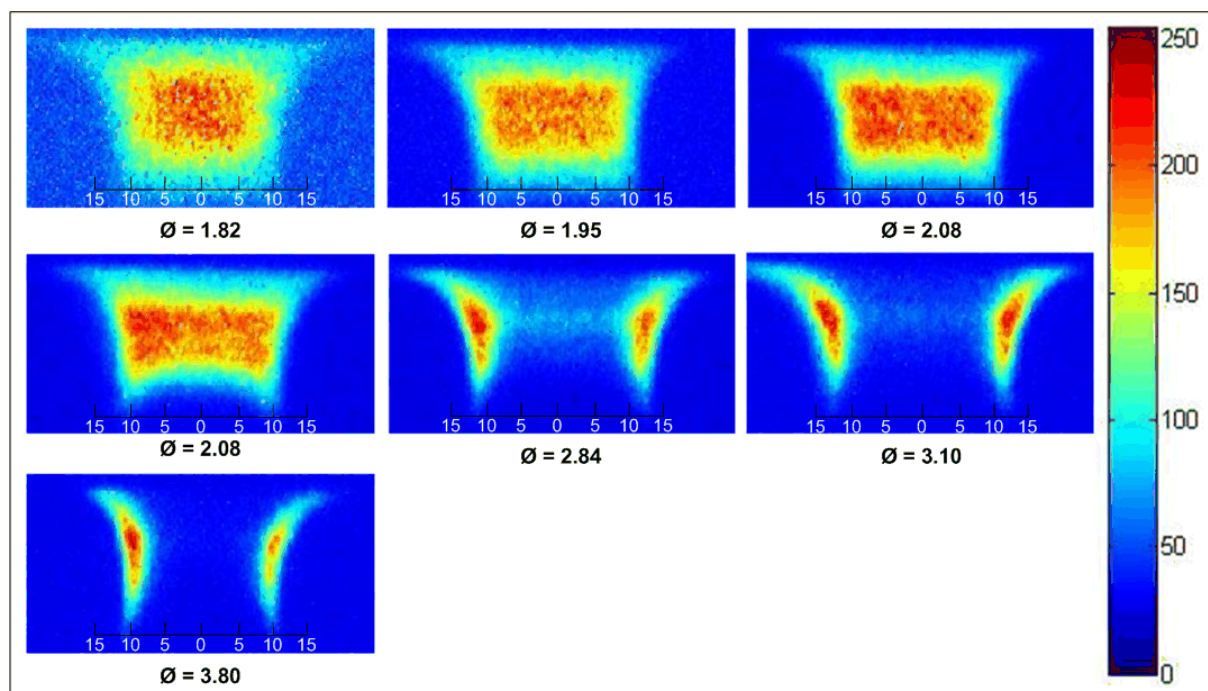


Figure 27 Raw instantaneous LII images at $\text{HAB} = 7 - 15$ mm; excitation wavelength at 532 nm (Note RGB is based on colour map jet).

Figure 27 reflects the instantaneous two-dimensional images obtained from the laser-induced incandescence process on laminar premixed ethylene flat flames. These images correspond to ones taken by visual observations in Figure 8. As the laser pulse passes through the reaction

zone (HAB 7 to 15 mm), the energy-absorbing soot particle quickly reaches incandescence levels which are later detected by the use of an ICCD camera, fitted with an interference filter. This filter of $410 \text{ nm} \pm 10 \text{ nm}$ bandwidth is used to suppress C_2 interferences [13]. Subtraction of background noises and sheet accumulation are applied to enhance the LII signal-to-noise ratio.

A closer inspection at the LII images will give an estimation of the soot distribution from least to heavy sooty conditions to test burner uniformity. As observed, a more uniform premixed structure can be easily determined from \emptyset at 1.82 to 2.22 with the strongest intensity located in the centre of the flame. It is evident from these structures that they exhibit a constant rectangular shape, predominantly of a homogeneous medium. However, as the flame tests deviate more to the fuel-rich conditions (\emptyset greater than 2.84), the relatively uniform soot distribution shifts to the flame edges exhibiting an annular region. This suggests that the flames behave more like laminar diffusion flames as opposed to premixed flames at less sooty conditions. In this condition, ambient air is allowed to mix and react within the flames even though flame velocity is higher than that of flame speed [94]. Nitrogen shroud co-flow was carried out at a static rate of 136 ml/min which was 1/20 to the least sooty flame test condition. At these physical conditions, flame ignition is only made possible by ambient air. Fortunately, the premixed structures exhibited at \emptyset less than 2.84 are still feasible for single-point calibration analysis due to homogeneity. Therefore the determination of the burner uniformity is not only dependent on the visual observations but also reliant on the soot distribution within the flame.

4.9.4 Normalised LII Profiles

MathLab[®] is employed to extract relevant values out of two-dimensional images from the ICCD camera. LII signals are averaged over 5 pixels on the image per mm and background intensity is taken into consideration. The radial profiles are normalized to the highest intensity at $\emptyset = 2.22$.

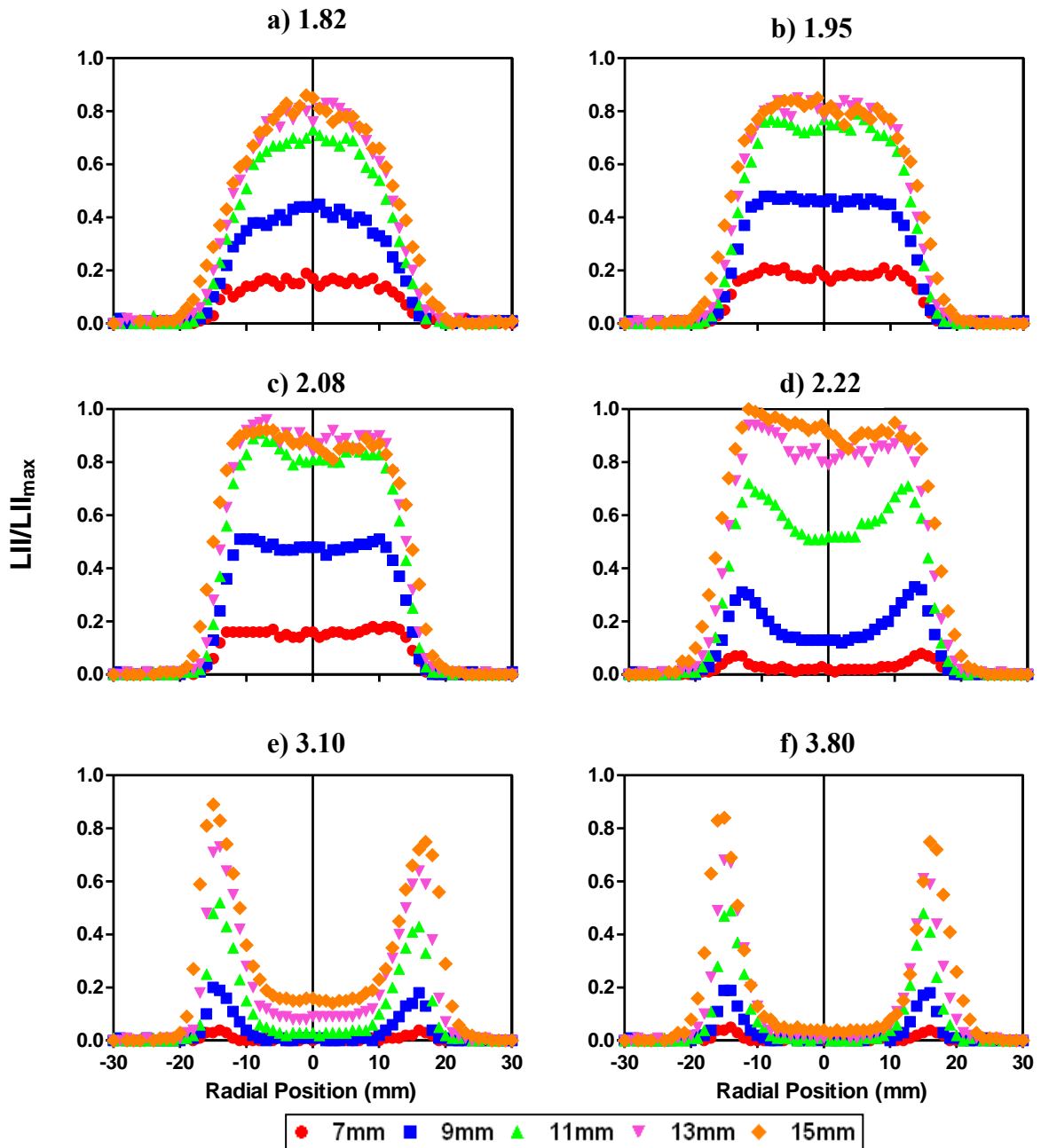


Figure 28 Normalized radial LII profiles, calibrated to the highest intensity at $\Theta = 2.22$

Figure 28 exhibits normalized LII radial profiles at various heights above burner in different flame locations. Throughout the flames development, they exhibit a cylindrical uniformity at least sooty conditions leading up to annular soot distributions at heavy sooty flames. The overall radial variation in the soot distribution is smaller in the centre than at the edges. In excess of fuel and ambient air mixing, soot particles are unable to undergo graphitization and oxidation. As a result, the LII signals decrease and lean towards the annular region of the flame as shown in Figure 28 (e) and (f).

The normalized radial profiles at $\varnothing = 3.10$ and 3.80 in Figure 28 exhibit trends of soot growth and oxidization similar to Quay and co-workers [12]. Strong LII signals at annular region of flame indicate soot particle net growth with increasing radial profile. This approximately corresponds to peak values observed at both ends of the radial profiles at radial position of 15mm . Further progress would result in a net destruction of soot particles through oxidation in the annular region, diminishing more rapidly than the centreline region. Another main cause for the annular trend at fuel-richer conditions is due to the lack of sufficient nitrogen shroud to prevent air entrainment. Given adequate shroud gas velocity, the expected structures at these conditions should be near uniform as flame test conditions at \varnothing less than 2.22 . However, two-dimensional incandescence imaging from Figure 27 suggests otherwise. It is the lack of air entrainment presence that allows ambient air to react with the burnt mixture and hence concentrating towards the flame edges. Consequently, this possesses difficulty in assessing single-point calibration to laser extinction in later stages as the latter assumes a homogeneous media for its calculations.

4.9.5 Single Point Calibration

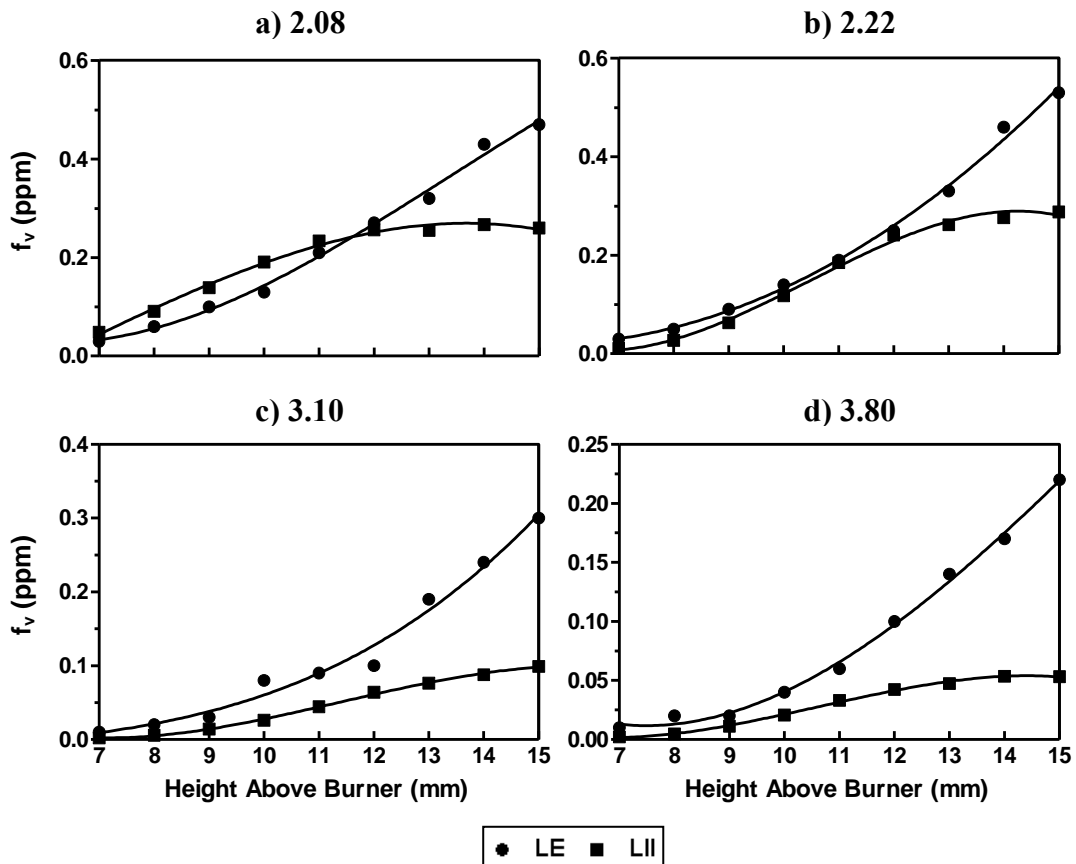


Figure 29 Soot volume fraction profiles (axial) as a function of HAB, calibrated to $\varnothing = 2.22$ of HAB 11 mm; lines: third-order polynomial fit

In order to calibrate the observed LII signals, the use of a single point calibration method with soot volume fractions obtained from laser extinction has been employed. This calibration method was employed by several authors [6, 7]. Laser extinction data from Flame Test 4 at $\phi = 2.22$ of HAB 11 mm is chosen as the single point calibration for the conversion of LII signals into soot volume fractions.

Figure 29 shows soot volume fraction profiles between laser-induced incandescence and laser extinction measurements. At low sooty conditions i.e. Figure 29 (a) and (b), calibrated LII profiles are in close agreement with those obtained by LE. This is in stark contrast to the fuel-rich conditions whereby the LII profiles underestimate LE profiles by a factor of three or more. This profound effect on the reduced soot volume fraction profiles can be attributed by two possible explanations. One potential reason is that the recently formed soot particles may contain significant material that is loosely associated with the core soot carbon structure, and this material would interact with the laser light during extinction measurements but would likely be volatilized under high laser irradiation with LII measurement [59]. Another explanation for the reduced profiles is the effect of non-uniform soot distribution. Comparison to fuel-rich conditions ($\phi = 3.10$ and 3.80) in Figure 28, it is obvious that the annular soot distributions in rich conditions will present difficulties in the calibration of soot volume fractions in the central section of the burner.

Other species other than soot capable of broad-band absorption in the visible and ultra-violet, may lead to a distortion in the measurement of the true soot volume fractions as determined by laser extinction. A computational study carried out by Wang and Frenklach [21] demonstrated that the importance of PAHs and their growth to particle nucleation and surface growth. This in turn, contributes to the particle mass at low HABs [78, 95]. Countless studies have been done to investigate soot volume fractions using visible wavelength light extinction [41, 42, 56, 96] though no local study is undertaken to investigate the effect of PAHs in the 1064 nm region. It is postulated that at 1064 nm wavelength, soot does not respond as strongly as those in the visible region and it may have a drastic effect on the soot volume fraction profiles by laser extinction which tends to be overestimated by a factor of two. However, during the write-up of this thesis, Kerbs and co-workers [166] recently published results, dealing with wavelength influence in extinction measurements.

4.9.6 Comparison of Radial Profiles

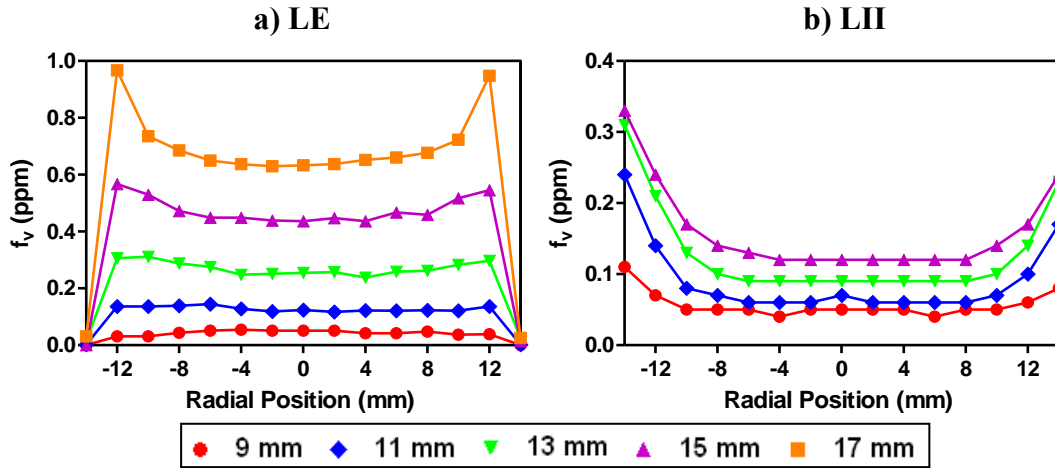


Figure 30 Comparison of radial soot volume fraction profiles between a) LE and b) LII at $\text{Ø} = 2.84$
(Note: LII profile is calibrated to $\text{Ø} = 2.22$ at HAB 11 mm)

Comparison of soot volume fraction radial profiles for both LE and LII measurements at $\text{Ø} = 2.84$ as a function of burner heights using tabulated results from APPENDIX C.1 and C.2 is shown in Figure 30. Observations into both trends suggest that the radial profile conducted by LII resembles more of a diffusion flame structure rather than a premixed one instead. Surprisingly, uniform soot distribution exists for HABs less than 13 mm over radial positions from -8 mm to +8 mm for both laser diagnostic techniques. This same trend in soot distribution was also observed in a recent article [40] using a similar stainless steel burner at $\text{Ø} = 2.76$. In later stages, the distribution is disrupted by the interdiffusion of ambient air into the flame due to low annular nitrogen co-flow. This is confirmed in Figure 30 (a) whereby the reaction zone near the stabilising plate above HAB 17 mm is uneven due to additional backward diffusion of gaseous products near stabilising plate. In response to both techniques, it is clear that the peak soot volume fraction range from 25 % (LE) to 50 % (LII) larger than the central region. This is due to the nature of diffusion flames on the onset of soot formation at flame edges.

4.10 Summary

Aside from laser extinction, laser-induced incandescence is another straightforward process to detect signals from soot incandescence which closely relates to the volume fraction by single-point calibration. This technique heavily relies on the use of a high energy pulsed laser to heat soot particles until incandescence whereby photodetection of the LII signals is made possible by an ICCD camera. This present study used a Gaussian profile pulsed laser of second harmonic wavelength at 532 nm with a pulse duration at 5 ns as main particle excitation

source. An interference filter of $410 \text{ nm} \pm 10 \text{ nm}$ was fitted to the ICCD camera, coupled with prompt gating, minimized potential hazards such as C_2 radical emission and background issues. Observations into the comparison of soot volume fraction profiles with laser extinction and the effect of soot distribution are discussed as follows:

- 1) Time-resolved measurements of LII signals were observed to follow a sharp rise in intensity followed by a relatively long decay ($\sim 300 \text{ ns}$) for peak laser fluence at $2.91 \times 10^8 \text{ W/cm}^2$. At this point, LII signals were found to be weakly dependent on laser fluences above the threshold limit.
- 2) Two-dimensional LII imaging of the soot incandescence provided an insight into the soot distribution with flame test conditions at \varnothing from 1.82 to 2.22, exhibiting a premixed uniform structure. Annular soot distributions observed for fuel-richer conditions were related to ambient air mixing due to insufficient nitrogen shroud.
- 3) Soot volume fraction profiles were in close agreement with flame test conditions at \varnothing from 1.82 to 2.22 but differences may arise up to a factor of three or more than those obtained by laser extinction for fuel-richer conditions. These significant differences were possibly attributed to the vaporisation of soot at high laser fluences and non-uniform soot distribution.
- 4) Insufficient time for further investigation into the impact of comparing laser extinction at both 532 and 1064 nm wavelengths compared against present LII measurements. The effect of between these two excitation wavelengths remained unknown but may be related to the presence of PAHs.

5 FLAME TEMPERATURES

This chapter addresses thermocouples as the main choice behind temperature measurements in flames. Manipulation of thermocouple values into temperature via heat transfer processes is considered. Factors influencing temperatures are reviewed. Axial and radial temperature profiles are discussed, including significant uncertainties such as ceramic cooling and low unburnt exit velocity.

5.1 Choice of Measurement

Flames are generally associated with temperatures and their importance to overall efficiency of the combustion process. For a one-dimensional flame, temperature measurement can be made as a function of height above burner. This temperature profile is categorised as a function of the incoming cold gas and is only secondarily affected by geometry, total flow rate, etc [32]. The thermal emission from flames can be attributed to the lack of equilibrium in the emission spectra of radicals present in the flame such as OH, C₂, and CH. These species show spectral vibrational and rotational temperatures in excess of the calculated adiabatic flame temperatures [97]. There are many methods of temperature detection but only a few possess sufficient reliability and spatial resolution for use in local flame measurements. A comparison on some of these methods is presented as below:

Table 4 Comparisons of methods used in flame temperature measurements [32]

Technique	Spatial Resolution	Precision (K or %)	Position Error (cm)	Applied Corrections	Cost
Thermocouple	10 ⁻² cm	1°	5 x 10 ⁻³	Radiation	Low-Mod
Resistance Probe	10 ⁻¹ cm	1°	10 ⁻²	Radiation	Mod
CARS	10 ¹³ cm ⁻³	1%	None	Non-Equilibrium Effects	High
X-Ray Absorption	5 x 10 ⁻¹ cm	3%	None	Molecular Weight	High

The thermocouple consists of two dissimilar metals co-joined at one end and can be simply inserted to any medium for immediate local measurement. This technique is similarly used in resistance thermometer but instead is dependent on the linear profile of the conductor inside. Besides these intrusive methods, the advantages of using spectroscopic detection techniques are that they are non-intrusive and have no high-temperature limit. One such technique is

Coherent Anti-Raman Scattering (CARS) that involves photodetection of molecules in their ground states. The fundamentals behind this method are much discussed in Kohse-Hoinghaus and Jeffries [98]. The X-ray absorption is another method which depends heavily on the density of the gas. However, the main drawbacks associated with these methods are that they have poor spatial resolution and encounter possible thermal interference from surroundings.

Temperature measurement by thermocouple still remains as the most versatile of all methods in much of the industry today, particularly petro-chemical industries. In practical uses, they are expendable with a low replacement cost and offers better accuracy and reliability than a pyrometer. Coupled with a suitable protective coat, the thermocouple can be exposed to either high temperature or corrosive environments.

5.2 Thermocouple Types

Considerations to the appropriate choice of materials used in the construction of the thermocouple have to be given in terms of type, insulation and probe construction. All of these have an effect on the measurable temperature range, namely accuracy and reliability of the readings. They are normally divided into two categories, noble metal and base metal thermocouples. Different alloy combinations will result in different combination of thermal emf versus temperature. An in-depth look into thermocouple types can be found in Kinzie [99]. Listed below is a summary of thermocouple types [100, 101].

Base Metal Thermocouples

Type E (Chromel / Constantan)

Type E is known for its high sensitivity at $58.5 \mu\text{V}/^\circ\text{C}$ at 0°C to $81 \mu\text{V}/^\circ\text{C}$ at 500°C . It has a lower drift rate than Type K thermocouples and it is well-suited for low temperature environments less than -250°C .

Type J (Iron / Constantan)

One of the most widely used thermocouples in industry due to relatively high sensitivity and low cost. Range is limited from 0°C to 760°C . Type J thermocouples should not be used in environments above 760°C as iron undergoes magnetic transformation which would cause permanent decalibration [101].

Type K (Chromel / Alumel)

Type K offers a high sensitivity and better resistance to oxidation than other base-metal thermocouples for up to 1260 °C. Thermocouples are available in the -200 °C to 1200 °C range. However, it is prone to attack in sulphurous and carbonaceous atmospheres.

Type T (Copper / Constantan)

For general applications, this combination can be used in oxidising and inert environments over temperature ranges from -250 °C to 850 °C. A useful attribute from Type T thermocouples is its high sensitivity at 40 $\mu\text{V}/^\circ\text{C}$ which remains constant over a wide range of temperature. They are excellent for use in sub-zero environments.

Noble Metal Thermocouples

Thermocouple types B, R, and S are all noble-based metals of platinum and rhodium in varying combinations. They are the most stable among all thermocouple and exhibit similar characteristics. Due to their low sensitivity and high durability, they are usually used for high temperature measurements.

Type S (Pt-10% Rh vs. Pt)

It is well-suited for high temperature measurements up to 1600 °C but low sensitivity at 10 $\mu\text{V}/^\circ\text{C}$ and high cost makes them unsuitable for general purpose use. It is normally used as the standard calibration for the melting point of gold (1063 °C).

Type R (Pt-13% Rh vs. Pt)

Type R thermocouple's characteristics are the same to Type S but offers a better stability than the latter.

Type B (Pt-30% Rh vs. Pt-6% Rh)

To widen the temperature range of Type R and S thermocouples, it is necessary to use an alloy negative arm instead of pure platinum. Type B thermocouples offer a melting point well above 1800 °C but exhibit the same output at 0 °C and 42 °C. This makes them redundant below 50 °C.

Stoichiometric premixed ethylene flames are known to reach adiabatic temperatures of about 2369 K [45]. Therefore in the selection of a suitable thermocouple type for high temperature measurements, the platinum-rhodium noble metal thermocouple type offers the best solution

for *in-situ* flame measurements. The properties and advantages of using Type R as the backbone for temperature measurements are elaborated in the next section.

5.3 Thermocouple Properties and Their Advantages

By inserting a thermocouple into the flame for local flame temperature measurements has been identified by far to be the most convenient of all temperature technique comparisons. In Figure 31, this technique utilises the use of thermoelectrical properties in dissimilar metals co-joined at a junction whereby if the junction experiences a different temperature than the opposite ends of the two wires, will result in a creation of a potential difference or emf which is proportional to a temperature difference. This potential is reproducible and is a function of the materials chosen for the wires [32, 102]. There are a variety of thermocouple pairs on the market but only a few which are suitable for flame studies such as Type S and R as previously discussed.

Figure 31 Basic thermocouple circuit [102]

The main advantages of employing this technique for flame temperature measurements as a function of height above burner are looked at. One, fine wire thermocouples can be made to achieve high resolution and minimise aerodynamic disturbances to the flames. Its adaptability to any location regardless of situation is almost boundless [99]. Second, they can be made out of a combination of materials to withstand high temperatures. Platinum alone showed a greater tendency towards catalytic activity than platinum-rhodium wire [103]. The addition of another noble element such as rhodium to platinum to form a binary alloy, usually improves the mechanical properties of the metal. Lastly, they offer a fast response time to a step change in temperature. An exposed bead offers a faster response but lacks chemical and mechanical protection.

Bare wire thermocouples in the presence of a flame can result in the promotion of chemical reactions and diffusion processes on the thermometer surface. This effect is known as catalytic oxidation. The abrupt temperature rises on the bead surface are due to the lower emissivity and catalytic heating [104, 105]. To combat this problem, a combination of yttrium

oxide and beryllium coating is found to yield the best protection when exposed to high temperatures for platinum-rhodium thermocouples [106]. Instead, silica is often used a coating to bare-wire thermocouples as the latter involves a much easier process of particle deposition at 1860 °C and fulfils the purpose of catalytic heating protection. Moreover, conduction cooling effect was observed to increase slightly for a Pt-10 % Rh vs. Pt thermocouple with silica coating [107].

Platinum-rhodium to platinum noble metal is often inferred as the main choice for thermocouple pair for typical temperature profile measurements. They are often used in comparison with thin-film pyrometry [108] as well as temperature impact on soot refractive index [66]. These measured temperature profiles are also used as starting estimates for kinetic modelling of ethylene flames [2, 50, 109] and propane flames [110]. Further developments in these kinetic models have been extended to include formation of the first polycyclic aromatics hydrocarbons [19, 21]. The key objective of using this noble metal combination manufactured as thermocouples as opposed to single elements is its ability to handle wider range of temperatures from -50 to 1760 °C [101] without undergoing any chemical reactions on the wire. The two commonly used platinum/rhodium combination type thermocouples exhibit the same temperature range but Type R is more susceptible to drift by interdiffusion [111]. Radiation correction procedure is applied to the thermocouple readings to estimate actual gas temperature. A possible source of error may arise from this procedure and depends heavily dependent on the energy balance and Nusselt number.

5.4 Measurement of Gas Temperature

The problem of heat radiation loss from the thermocouple bead still remains an important source of error in temperature measurements. The thermocouple does not measure the gas temperature but rather the temperature of the thermocouple junction instead. This temperature results from a balance between all of the heat transfer processes adding to or removing energy from that junction. For a simplified analysis, it is typical to isolate those processes to only consider convective and radiative heat transfer processes. At steady state, the energy balance for an uncoated thermocouple [107] assuming no catalytic effects can be written as follows:

Temperature Gain (Convection) = Temperature Loss (Radiation + Conduction)

$$h_c A_{bead} (T_{gas} - T_{bead}) = \varepsilon \sigma A_{bead} (T_{bead}^4 - T_{\infty}^4) + \frac{k_w A_{wire}}{x} (T_{bead} - T_{ref}) \quad \text{Equation 5.1}$$

The first term on the left represents the heat is added to the thermocouple junction through convection from the hot gases of the flame where h_c is the convective heat transfer between surrounding gas and thermocouple bead, T_{bead} is the thermocouple temperature and T_{gas} is the gas temperature of interest. The next term accounts for the heat is lost from the thermocouple junction through radiation at T_∞ where ε is the emissivity of the bare bead thermocouple that is a function of temperature, σ is the Stefan-Boltzmann constant at $5.67 \times 10^{-8} \text{ W/m}^2 \cdot \text{K}^4$ and T_∞ to be assumed at ambient environment of 298 K. The last term of the equation contributes to the heat loss due to thermal conduction along the leads of the thermocouple. It is difficult to estimate the temperature gradient at the interface of the thermocouple bead and wire therefore the application of a fine wire thermocouple is to minimize conduction errors [107]. The error due to radiation effects is as follows after simplifying Equation 6:

$$T_{gas} = T_{bead} + \frac{\varepsilon\sigma}{h_c} (T_{bead}^4 - T_\infty^4) \quad \text{Equation 5.2}$$

The dimensionless Nusselt number (Nu) is a function of two other dimensionless quantities: Reynolds number (Re) and Prandtl number (Pr). It combines the flow characteristics and properties of the flowing media in forced convection conditions [112]:

$$Nu = f(Re, Pr)$$

To evaluate the convective heat transfer coefficient in Equation 7, Nusselt number is used to estimate the forced convection over a sphere at low Reynolds number between the gas flow and thermocouple bead in Equation 8 [108]:

$$Nu = 2 + (0.2Re)^{0.82} \quad \text{Equation 5.3}$$

Valid for: $Pr = 0.71$ and $0.07 \leq Re \leq 20$

Other expressions for the Nusselt number for forced convection flows around a sphere are available in Holman [113]. Thermophysical properties are assumed to be those of air. Further details into the radiation correction procedure are highlighted in APPENDIX A.6. Finally, the energy balance in Equation 7 can then be solved for the actual flame temperature.

5.5 Factors Influencing Temperature

5.5.1 Velocity

Temperature dependence on velocity can be inferred from the continuity equation. The continuity equation requires that the burnt gas velocity to be greater than the velocity of the unburnt velocity gas [45]:

$$\rho_u S_L A \equiv \rho_u v_u A \equiv \rho_b v_b A \quad \text{Equation 5.4}$$

Where the subscripts denote u and b to the unburnt and burnt gases, assuming a one-dimensional structure and unburnt gas enters the flame in a perpendicular direction to the flame sheet. Based from this scenario, the density of the products is much smaller than the density of the reactants due to heating. This will result in a lower mass flux and temperature for the burnt gas. Furthermore the influence of the burning velocity may change the shape of the temperature curves [36].

Figure 32 Measured temperature profiles and their corresponding flowrates at $\phi = 2.07$ [114]

A drop in unburnt gas velocities can have a drastic impact on the downstream flame temperatures. Figure 32 illustrates the variation in the flame temperature by lowering the mass flow rate of the cold gas but keeping equivalence ratio constant. The maximum flame temperatures varied from 1600 to 1900 K for all six flames. It was noted that the standoff distance of the higher-velocity flames was smaller than that of the low-velocity flames. Nonetheless a mere three-fold difference in the cold gas velocity between C_1 and C_6 velocities would result in a 288 K temperature variation as a consequence of decreased cooling at higher cold gas velocity. For low gas velocities, there is less convective heat exchange between bare-bead thermocouple and the gas [115].

5.5.2 Equivalence Ratio/Fuel Type

The primary effect of equivalence ratio on laminar burning velocity, S_L for similar fuels will affect flame temperature. This is shown in Figure 33 as compiled by Law [94] for various fuels that are considered to be some of the reliable data to date. The compilation reveals flame speeds to be at maximum for slightly rich conditions and falling off as the fuel gains less oxidant. This reflects on the strain rate within the flame. The expectancy of a higher strain rate will result in higher temperatures due to molecular and mixing effects [45].

Figure 33 Effect of laminar burning velocities of ethane, ethylene and acetylene with air at atmospheric pressure as a function of equivalence ratio [94]

Different structures of the C_2 fuels have a significant impact on the laminar burning velocities. Laminar burning velocity trends for C_2 alkanes (single bond), alkenes (double bonds) and alkynes (triple bonds) are shown in Figure 33 as well. These unsaturated C_2 fuels differ in their number of carbon-carbon bonding sites. They all follow the same trends as a function of flame temperature. As the number of carbon-carbon bonding increases, flame speed dominates more to the fuel-rich side. This allows high flame temperatures to be achieved at fuel-rich conditions. A closer examination at ethylene/air combustion would expect adiabatic temperatures to be reached at equivalence ratio of 1.3. However, it was identified that the coupled effects of stretch and preferential diffusion could lead to systematic shifts in S_L [116]. This may result a shift in the curve depending on the unburnt gas velocity.

5.6 Experimental Description

This section covers the specifications of the thermocouple, in-house built amplifier and analogue hub.

5.6.1 Thermocouple Specifications

Experimental temperature profiles from flat flames eventually serve as starting estimates to kinetic modelling. This will result in close predictions of the chemical reactions involved in typical one-dimensional flames as compared to simulation only basis. Therefore a ceramic coated Pt-13 %Rh vs. Pt (Type R) thermocouple is used specifically for this purpose. This thermocouple is able to handle temperatures between $-50\text{ }^{\circ}\text{C}$ to $1760\text{ }^{\circ}\text{C}$. As illustrated in Figure 34, temperature measurements are made through the detection of the junction end of the thermocouple. Both bead and wire dimensions are approximately about 328 micron and 50 micron in diameter. The fine bead is exposed at 4 mm near the junction tip cemented in ceramic to prevent catalysis oxidation. The lead wires are encased in a ceramic insulating rod which measures at least 400 mm in length for sufficient probe intrusion in sooting flames. On the other hand, it is this ceramic coating that prevents the “true” measurement of the flame due the cooling effect experienced on the thermocouple wires. Moreover, this coating also obstructs *in-situ* temperature measurements from datum line to HAB 3 mm.

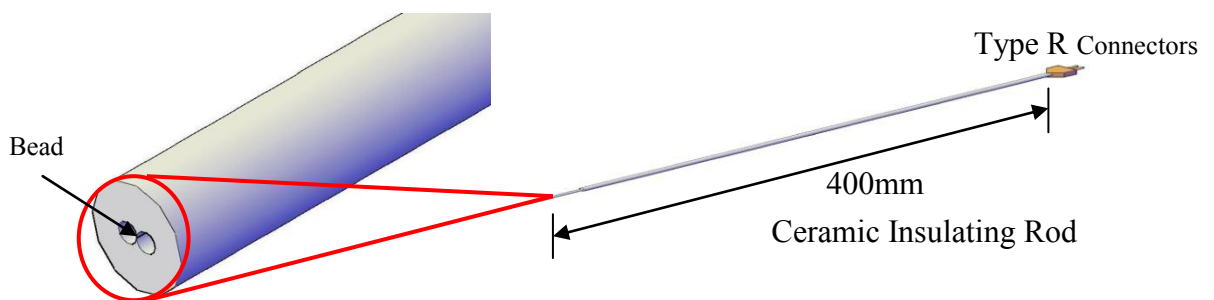


Figure 34 Cross-section of Type R thermocouple

Temperature readings are subjected to radiation losses with an assumed emissivity of unity due to the sooting nature of ethylene flames. Conduction effects through the 400mm lead wires are assumed negligible. To establish the output signals on the thermocouple, it is connected to an extension wire of about 2 metres to an in-house built amplifier which is then digitized and sent to a computer for subsequent post processing.

5.6.2 Amplifier and Data Acquisition

There are two components in this procedure that are required to fully extract the relevant temperature data. They are the in-house built Type R amplifier and the analogue hub.

The main aim of the amplifier is to amplify the thermocouple output signals and convert them to corresponding temperatures. Every 2.5 mV increment on the thermocouple junction end detected by the in-house built amplifier is equivalent to one degree increment. However, it is

important to note that the amplifier must be calibrated to zero or near zero values as drifts may occur once every 600 readings or more which roughly deviates by 2.12 °C [111]. Therefore it is of substantial requirement that the amplifier be regularly calibrated unless its offset is known otherwise. The analogue signals from the amplifier are transferred to an analogue hub through a data cable for digitization.

The analogue hub or MacLab/4 MK III acts a multi-functionality data logger with four different channels consisting of both positive and negative voltage inputs for use. Only the first channel of positive input is used here to measure the output signals from the amplifier. This channel converts the raw signals from analogue to digital and displays them as a function of time. CHART software [70] uses real-time plotting of voltage values as a result of this. An electronic low pass filter of 50 Hz is used to remove any background interference. This will filter out the irregular disturbances and average out the readings. The displayed data is saved and extracted out as text file (.txt) for offline processing.

5.7 Experimental Layout

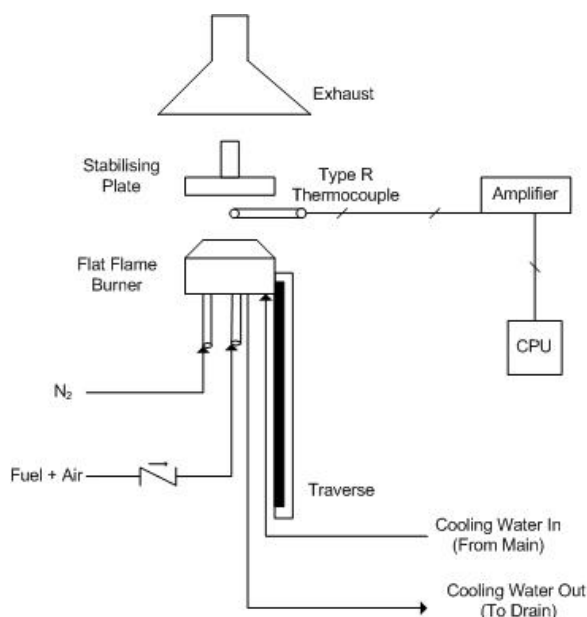


Figure 35 Thermocouple placement layout

The experimental layout for the temperature measurements in laminar premixed flat flames is shown in Figure 35. The fuel and air supply are T-jointed in the stainless steel premixed line at least 1 metre in length prior to the burner. This is to ensure smooth and thorough mixing before combustion. Adjustments are made to the thermocouple axial heights via movable vertical traverse.

Thermocouple insertion into the stabilised flame must be achieved with minimum interferences to flame body. To carry this out, the thermocouple is first attached to a retort stand with end connections made to the amplifier. A balance ruler is used to ensure the thermocouple horizontal horizon. With height modifications made only to the vertical traverse, the thermocouple is inserted into the centreline of the stabilised flame with a rotation of the retort stand arm. With a bead contact volume of 0.01 mm^3 , the bead contact area will only occupy about $1.4 \times 10^{-3} \%$ of the flame reaction zone.

Satisfactory results cannot be obtained unless some form of iteration is made to the CHART software [70]. Depending on the axial height of the thermocouple, the voltage range is adjusted accordingly until the readings are detected with one suitable voltage range set. The data logger collects the measurements with a sampling rate of 10 Hz for duration of 1 minute. The raw data is then saved and later processed for radiation correction.

5.8 Thermocouple Interruption

Inaccuracies in the flame disturbance and bead emissivity will lead to a reduced effect on the temperature profiles. A small disturbance to the flame was observed in Figure 36 during probing and may interrupt the forced convection flow to the exposed thermocouple bead. In addition, the sooting nature of ethylene flames constantly coats the exposed bead which results in the decrease in actual temperatures.

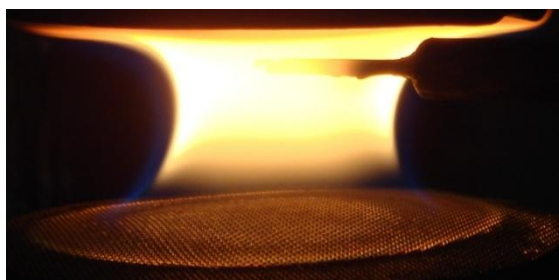


Figure 36 Flame disruption by thermocouple

Furthermore the ceramic coating of the thermocouple wires resulted in a major temperature difference error as opposed to an unshielded one. A separate comparison test was conducted using an unshielded different bead diameter ($800 \mu\text{m}$) constructed of the same materials and tested in a stoichiometric premixed natural gas flame. Preliminary results revealed that the presence of this ceramic coating occur an error difference of 205 K to the smaller thermocouple. Therefore in the light of this matter, this major error is also included in radiation correction losses procedure (See APPENDIX A.6) to account for ceramic cooling.

5.9 Results and Discussions

In-situ temperature measurements are performed using a ceramic coated Pt-10 %Rh vs. Pt thermocouple with an exposed spherical bead inserted perpendicular to the flame. Voltage signals amplified from the thermocouple is converted. The next step involves applying appropriate correction to account for radiation heat losses and ceramic wire cooling effects. Corrected temperatures are presented as either a function of HAB or radial positions in APPENDIX C.3. Discussions into both axial and radial temperature profiles are presented. Major gas uncertainties including physical and experimental correlations are addressed.

5.9.1 Temperature Profiles

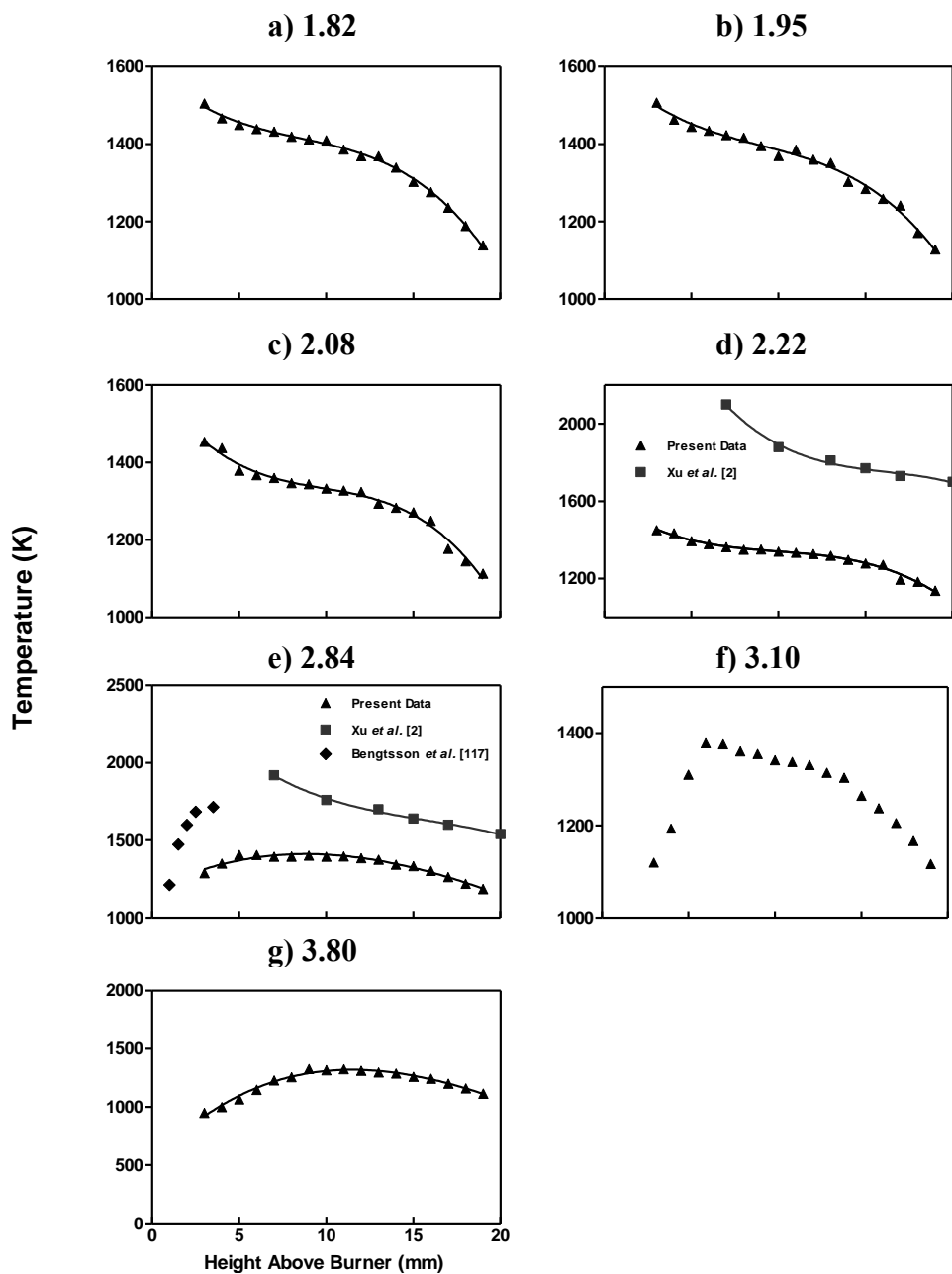


Figure 37 Temperature profiles (axial) at $\varnothing = 1.82$ to 3.80 from HAB 3 to 19 mm at flame centreline; symbols: measurements; lines: third-order polynomial fit

Factors such as mass flow and heat transfer to burner plate can not only cause dissimilar temperature patterns but also result in a difference in temperatures. Measured temperatures per above burner height are subjected to radiation correction and ceramic coat compensation as summarised in APPENDIX C.3. These corrected temperatures, Tables 23 to 29, are profiled against height above burner for each fuel ratio. Figure 37 shows axial temperature profiles for HAB 3 to 19 mm from slight to heavy sooty conditions. Temperature profiles at flame test conditions at ϕ from 1.82 to 2.22 show evidence of higher temperatures near the burner surface followed by a relatively constant plateau near the mid-section of the reaction zone which then drops drastically approaching to the stabilising plate due to oxidation. As the flowrates associated with these conditions are higher, the distances between the burner plate and flame reaction zone are higher hence reducing heat transfer to the burner plate. However, these profiles offer a different distinction from those observed at much sootier flames (ϕ greater than 2.84). The temperatures are 200 K lower than those at slightly sooty conditions, with the maxima reaching the centre of the flame reaction zone at HAB 10 mm. A low nitrogen co-flow resulted in the ambient air mixing with the gas mixture at fuel-rich conditions and reacts to form the annular soot distribution as depicted from 2-D LII images in Figure 27. Temperatures near the burner plate are much lower as a result of lower mass flow rates which inadvertently increase burner plate heat transfer.

The degree and curvature of the temperature profiles can be attributed to both measurement technique and stoichiometry conditions. Overall as the flame gets sootier, maximum axial temperatures shift from 1400 to 1500 K near burner surface to slightly over 1100 K at HAB 10mm. Flame test conditions at ϕ greater than 2.84 are seen to exhibit different curvature patterns as opposed to that obtained at less sooty conditions. This shift in pattern is reasoned to be from significant heat loss to the burner plate. As burning velocities decrease with increasing ϕ , the heat flux to burner plate increases and hence significantly reducing temperatures near burner surface shown in Figure 37 (e) to (g). The difference in temperatures can range from 334 to 360 K depending on flow conditions as previously determined by Prucker *et al.* [37]. The present work is compared to axial temperature profiles of past works [2, 117] shown in Figure 37 (d) and (e) even though Bengtsson *et al.*'s work [117] was carried out at equivalence ratio of 2.52. Focusing on Figure 37 (e), it seems that there are no similarity in both trends and temperatures. Both previous articles used different spectroscopic techniques such as multi-line emission [2] and CARS thermometry [117] to yield fairly accurate temperatures within ± 50 K as opposed to thermocouple measurements. In addition, due to the nature and characteristics associated with the present burner and burner plate heat flux uncertainty, may result in a large difference in temperatures and trends.

5.9.2 Radial Profile at $\varnothing = 2.84$

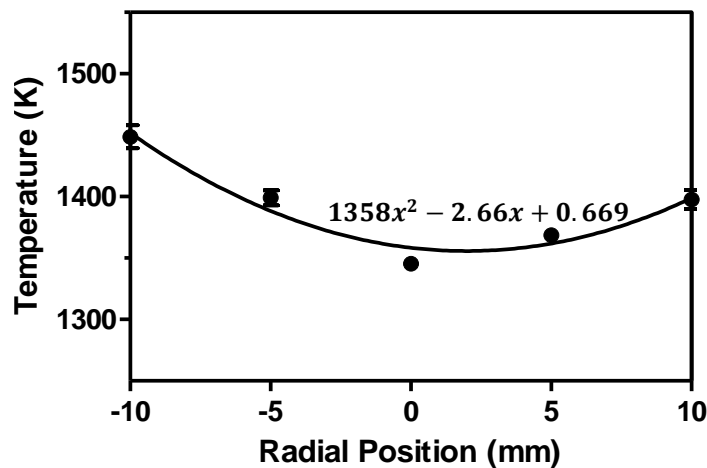


Figure 38 Temperature profile (radial) at $\varnothing = 2.84$ at HAB 15 mm; line: second-order polynomial fit

Thermocouple measurements are performed for $\varnothing = 2.84$ at HAB 15 mm in the radial direction parallel to burner plate. Their results are shown in Table 30 of APPENDIX C.3. Figure 38 shows the radial temperature profile described by a second-order polynomial fit of the radial position, assuming that the heat flux from the flame to the burner plate is uniformly distributed and the axial temperature variation is much smaller than the radial variation. The general shape of the profile is similar to the radial profile as demonstrated by LII in Figure 30 (b). This is consistent with the presence of soot interaction with the ambient environment. The non-uniform trend suggests that soot distribution revolves around an annular structure, which in effect reflects lesser flame strain and lower burnt gas velocity. This corresponds more to a diffusion flame structure as determined by LII.

5.9.3 Gas Temperature Uncertainties

Gas temperatures are obtained through the use of an energy balance relationship based on a spherical bead exposed to the combustion environment. This relationship involves the convective heat transfer between the thermocouple and the gas, radiative loss from bead back to the ambient environment and conductive term along thermocouple wires. The importance of a used McKenna burner condition is regarded negligible as temperatures were found to vary by an average of 26 K [37]. Therefore it is important to identify other potential errors and their influence on the accuracy of the gas temperature measurement. The major sources of uncertainty identified are convective heat transfer coefficient (h_c), low burner exit velocity (U_o) and ceramic cooling.

The convective heat transfer coefficient is directly related to the Nusselt number correlation for heat transfer which is related to the bead diameter, d_{bead} as shown in Equation 9 (See Appendix A.6). There are several issues involving Nusselt number calculations which some of the methods used are as similar to Struk and co-workers [108]. First, the correlations are meant for bulk heat transfer. Second, Reynolds Number required for the correlation requires knowledge of the burnt gas velocity. For this present study, an estimate of the actual gas velocity is determined from the software provided [53]. Lastly, both Re and Nu correlations are estimated at film temperature using thermophysical properties of air as no effort was made to measure the composition of the burnt gas at each flame test condition.

Another obvious difference is the output of unburnt gas velocity to the combustion reaction. An increment in the combustion volume will increase the distance between the flame and the burner matrix (Δh) and thus encounter less temperature differences to adiabatic. However, it is this heat transfer to burner plate by conduction [49] which allows the premixed flat flames to stabilise. This may induce heat recirculation back to the unburnt mixture which is difficult to measure. Reynolds number depends heavily on the unburnt gas velocity and air viscosity which indirectly relates to the heat transfer coefficient, h_c . Any slight changes to either component would significantly alter the gas temperatures from 126 K to 436 K in magnitude.

Not forgetting that the effect of ceramic coating on the thermocouple wires can have a substantial cooling effect on the temperature profile. Upon thermocouple probe insertion, the exposed spherical bead and a small section of the encased wires about 4 mm were subjected to the flames. This consequently lowers the thermal emf to the amplifier and thus producing a reduction in temperatures. This effect is termed “ceramic cooling” effect. This effect is examined using a different size thermocouple constructed of the same material. This resulted in a 205 K difference to the smaller size thermocouple. This temperature difference closely resembles to that obtained by Coherent Anti-Stokes Raman Scattering (CARS) for CH₄/air flames [37]. This difference is added in on top of the radiation correction procedure as compensation.

5.10 Summary

Temperature measurement by thermocouple has proven to be the most simplest and versatile method among all other techniques for measuring temperatures in one-dimensional flames as a function of height. Type R (Pt-13 % Rh vs. Pt) thermocouple was chosen as the main tool for *in-situ* thermocouple measurements due to its stability to handle high temperatures in a

broad spectrum. Radiation correction for the thermocouple is based on a steady-state energy balance which uses forced convection over a sphere at low Reynolds number for heat transfer coefficient, h_c . Ceramic coating on thermocouple lead wires resulted in a cooling effect on the wires. Discussions pertaining to the effect of unburnt gas velocity and ceramic cooling on temperature profiles are discussed as follows:

- 1) Results revealed that axial temperature profiles from \emptyset less than 2.22 were in stark contrast to those at very sooty conditions (\emptyset at 2.84 onwards).
- 2) A higher unburnt gas velocity would result in longer distances between flame reaction zone and burner plate, effectively reducing heat transfer to the burner plate. This was found to influence the magnitudes and shapes of the temperature profiles.
- 3) Radial temperature profile at $\emptyset = 2.84$ at HAB 15 mm revealed that there was indication of soot interaction with ambient environment due to insufficient nitrogen co-flow which resulted in a non-uniform trend along the radial profile.
- 4) The major uncertainties associated with convective heat transfer coefficient, h_c include air properties specified in Reynolds and Nusselt correlations, variations in unburnt cold gas velocity and a make-up difference of 205 K due to ceramic cooling.

6 SOOT MORPHOLOGY

Analysis of soot structure is the main purpose behind this chapter. To understand this objective, literature reviews into soot development are reviewed. Thermophoretic sampling particle deposition and its layout are briefly described. Soot structure and diameters are considered for four flame test conditions.

6.1 Development of Soot

This section reviews the physical and chemical processes associated with soot production from flames. Background research into soot development has identified that soot evolves from initial molecular fragments which undergoes surface growth to the formation of polycyclic aromatic hydrocarbons.

6.1.1 Introduction to Soot

The formation of soot, as a resultant from fuel-rich combustion hydrocarbon processes, is black in appearance with composition similar to that of graphite. Soot usually forms in temperatures from 1000 to 2500 °C with an approximate density value of 1.8 g/cm³ after mass growth [23] and is dependent on fuel ratio [27]. Other elements such as hydrogen are present (about 10% when young) in soot as well [28]. Comprehensive reviews and literature regarding soot formation in premixed flames are available [1, 28, 46, 118]. As reviewed, soot is made up of numerous clusters of soot particles which are too small to examine under the naked eye. With the use of an electron microscope, a typical soot structure consisting of these clusters can be examined in Figure 39.

Figure 39 Electron micrographs of soot particles chains. Mean diameter of particle ca. 200 Å [1]

A closer inspection into soot under electron microscopy in Figure 39 reveals that the building blocks of soot are spherical or near spherical in shape with mean diameters around 20 – 30 nm, corresponding to 10^6 carbon atoms [1]. These particles are classified as primary soot particles, sometimes referred as spherules [48]. They have a tendency to adhere to each other to form either straight or branched aggregates chains. These aggregates may contain as many as several tens to hundreds of primary soot particles. However, it is the clustering of aggregates into agglomerates that forms the visible, fluffy characteristic [28] of soot.

Significant research efforts into the formation and growth of aromatic hydrocarbons into the development of soot for atmospheric premixed laminar flames have been reviewed in recent years [19, 21, 119-121]. Although there remains some issues regarding the formation of PAH and soot, there is still a general consensus on the physical and chemical processes involved. A schematic reaction path leading to soot formation from molecular basis leading up to the final particulate form for premixed flames is shown in Figure 40.

Figure 40 Schematic reaction path for soot formation in premixed flames [47]

In summary, the premixed hydrocarbon fuel is degraded into smaller hydrocarbon radicals during combustion. The formation of the first aromatic ring, from aliphatic fuels, is suggested to evolve from either propargyl radicals (C_3H_3) recombination [20] or vinyl (C_2H_3) addition by acetylene (C_2H_2) [122]. The growth of this aromatic ring to larger sizes occurs mainly via

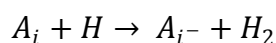
the addition of C₂, C₃ species, among which acetylene has received much attention, to PAH radicals, and reactions among the growing aromatic species, such as PAH-PAH radical recombination and addition reactions [47, 48, 121]. All of these processes occur within molecular length scales. Primary soot particles soon take shape by coagulation and surface growth, whilst picking up growth components from the gas phase. The sticky collisions between particles during the mass growth process attribute to the final size of the soot particles with a decline in particle number. At longer reaction times, the oxidation of PAHs and soot particles compete with the formation of soot. It decreases the mass of PAH and soot material through the formation of CO and CO₂. The main oxidant reactants contributing to the oxidation process are possibly be O, OH and O₂, particularly for fuel-rich conditions where OH radicals is proposed to be the main contributor [55].

There have been several proposals made with respect to the general nature of soot particle inception that include chemical ions [27] or PAHs [28] as key gaseous precursors to soot. However, it is the latter rate-limiting step of PAH formation and surface growth that lends itself to the present development of a single soot particle.

6.1.2 Particle Inception

Soot inception evolves from the transformation of a hydrocarbon fuel into that of a particulate, usually of carbon nature. In the early stages of soot development ($T \leq 1500$ K), soot inception begins with the thermal decomposition of fuel molecules into the formation of unsaturated hydrocarbons particularly acetylene and condensed unsaturated ring systems such as polycyclic aromatic hydrocarbons [1, 28]. These species are thermodynamically stable [123] and capable of further growth at higher temperatures. They consist of heavy PAHs of molecular weights from 500 to 1000 amu. The growth of small molecules such as benzene into larger PAHs is widely accepted to be either by acetylene addition to PAH radicals or PAH-PAH radical recombination and addition reactions [47, 48, 121]. Particle inception rates are estimated to be between 5×10^{15} and 5×10^{16} cm⁻³s⁻¹ [44] and expected to increase for surface area growth with respect to fuel equivalence [124].

The growth of larger aromatic species follows quintessentially the H-abstraction-C₂H₂-addition (HACA) mechanism as previously introduced by Frenklach and Wang [24]. It involves a repetitive reaction sequence of two principal steps: (1) abstraction of a hydrogen atom from the reacting hydrocarbon by a gaseous hydrogen atom represented by:



Equation 6.1

Followed by (2) addition of a gaseous acetylene molecule to the radical site formed:



where the notation for A_i is an aromatic molecule with i peri-condensed rings and A_{i-} is its radical as previously reported [121, 125]. The significance of the HACA reaction path is to activate a stable aromatic molecule by converting it first into a radical followed by acetylene addition, thus promoting continual molecular growth and cyclization of PAH as shown in Figure 41.

Figure 41 H-abstraction- C_2H_2 -addition mechanism for PAH Growth [48]

Under the PAH model hypothesis [48], PAH monomers begin to stick to each other during collision after reaching sufficient sizes, thus forming PAH dimers. The PAH dimers continue to collide with other PAH molecules to form PAH trimers or with other dimers, and so on. Eventually, the PAH clusters evolve into solid particles as they increase in size via molecular chemical growth reactions.

6.1.3 Particle Growth and Coagulation

After the formation of nascent soot particles, the mass of these particles are increased via addition of gas species such as acetylene and PAH, including PAH radicals [47]. In comparison to the nucleation kinetics, considerable amount of soot loading is observed during surface growth [126]. The reactions associated with surface growth has been treated comparatively to the planar growth of PAHs [24] which is described earlier by the HACA mechanism but instead applied to the heterogeneous surface growth of soot particles. Abstraction of the hydrogen atoms activates the surface of soot radicals which promotes the surface reaction process. It is established in experimental studies of laminar premixed flames that acetylene is the dominant gas species that reacts at the particle surface and that the carbon deposition process follows 1st order kinetics [3, 71, 120]. The total growth rate of soot is limited by the availability of surface area [3].

During the coagulation process, the colliding particles fuse and form into large particles, reducing the number of soot particles without a change in total mass. This occurs almost immediately after soot particle formation or when soot particles are still relatively “young” [126]. There is still a continuation of the molecular addition of gas phase species after the early formation of composite particles via sticking particle-particle collisions [47, 48], partially hiding the identity of primary particulate units in electron microscopy images of soot particles.

After particle coagulation, soot particles are observed to agglomerate, i.e. stick to each other to form chain-like structures. This process does not occur early in the flame at particle inception but rather at longer residence times when soot particles are mature. It converts the initial amorphous soot to a more progressive carbon material, with a slight decrease in particle mass but not affecting particle number. Measurement of these chain-like structures in terms of fractal geometry and dimensions [16, 127, 128] has been of great interest lately. The *ex-situ* technique responsible for this analysis of soot aggregates is termed thermophoretic sampling [16] and is often combined with transmission electron microscopy (TEM) to determine soot size and morphology.

6.2 Thermophoretic Sampling Particle Deposition

Laser scattering and extinction technique has been widely used to determine number densities and particle sizes in non-isothermal flame conditions due to its non-intrusive behaviour [42, 126, 129]. However, the optical technique requires proper interpretation of the refractive index throughout the soot field in order to correctly model the soot aggregates. Therefore to complement the above optical technique, a rapid extraction of soot particles followed by subsequent electron microscopy analysis, developed by Dobbins and Megaridis [16], was used to measure the size and morphology of flame-generated soot. This technique was further developed by Koylu and co-workers [17] to extend modifications into its sampling times and spatial resolution. This revised sampling technique is now known as thermophoretic sampling particle deposition (TSPD). The main advantage of TSPD technique is that it is able to isolate each type of morphology as soot evolves from translucent precursor particles to mature carbonaceous aggregates respective of burner heights without prior knowledge of particle bulk density and refractive index.

The TSPD technique is based on a theoretical extension of Eisner and Rosner [18], who established that soot deposition rates to cold surfaces immersed in flames are dominated by particle thermophoresis. This same principle was also applied to absolute measurements of

soot based on temperature responses of thermocouple beads in various non-premixed flames [130]. Thermophoresis is a phenomenon whereby small spherical particles suspended in a gas are characterized by a temperature gradient, $\text{grad } T_g$, and drift in the direction opposite to that of $\text{grad } T_g$ [131]. The local particle velocity can be expressed in terms of a thermophoretic diffusivity D_T , local gas temperature T_g , and temperature gradient, $\text{grad } T_g$ as reported in Gomez and Rosner [131]:

$$u_T = D_T \left(-\frac{\text{grad } T_g}{T_g} \right) \quad \text{Equation 6.3}$$

Where D_T for a spherical particle in the free molecular regime is expressed as:

$$D_T = \frac{3}{4} \left(1 + \frac{\pi}{8} \alpha_{mom} \right)^{-1} v_g \quad \text{Equation 6.4}$$

With α_{mom} being the momentum accommodation coefficient and v_g the momentum diffusivity of gas mixture at T_g . As a result from the above equations, the rapid insertion of a cold probe surface into a particle-laden hot gas will result in a drift of particle mass across the thermal boundary layer.

6.3 Sampling Layout

The fundamental purpose of the TSPD technique used in flame combustion is to insert a probe surface at room temperature into the soot-laden flames with a single and swift action so that deposited soot particles still retain their morphological characteristics.

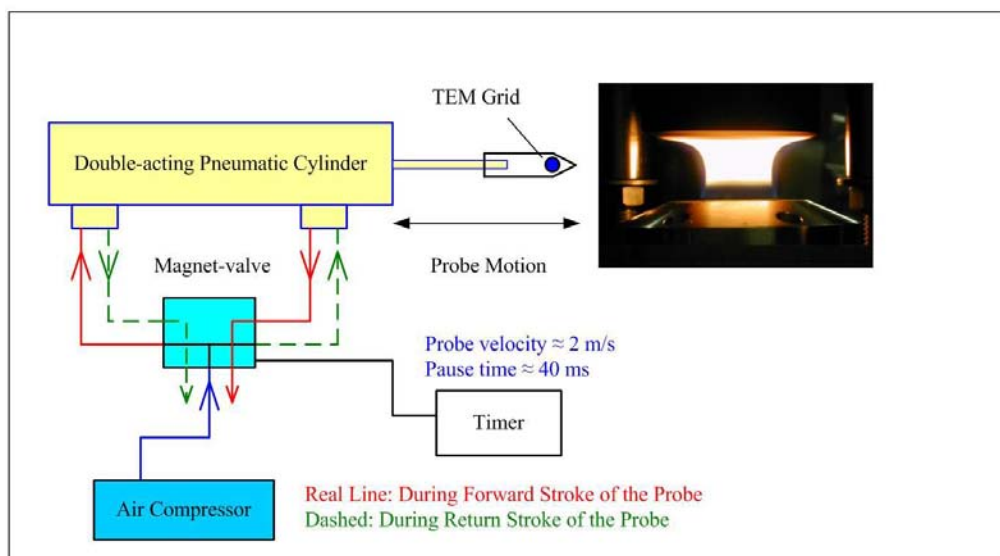


Figure 42 TSPD experimental arrangement

The experimental arrangement for TSPD is illustrated in Figure 42. A 3 mm diameter circular porous TEM grid (Electron Microscopy Sciences Copper based-carbon film coated, 200 mesh) is used as the main sampling grid for particle deposition as previously employed [16, 17]. Carbon films employed as TEM sampling grids are highly recommended due to their stability and image clarity when exposed to high magnitudes of electrons during magnification. The 200 mesh copper grid is made up of $40\mu\text{m}$ bars forming $85\mu\text{m}$ square holes. The markings on the TEM grid made it possible to obtain 1mm position correspondence between flame and microscope co-ordinates. Koylu and co-workers [17] employed the use of stainless steel substrate, 4 mm wide and 0.4 mm thick, as a grid holder to minimize flame disruptions. A pair of stainless steel tweezers, as shown in Figure 43, is used as a holder for the TEM grid instead to reproduce the same effect. The tweezers or probe is aligned perpendicular outside the flame prior to insertion.

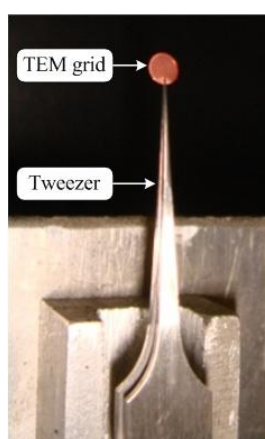


Figure 43 TEM grid holder

A double-acting pneumatic cylinder of 200 mm stroke, operating through a two-directional electromagnetic valve and a timer, is used to insert the TEM grid into the flame for a time period of about 40 ms. This short exposure time is sufficient enough to present the cold TEM grid into the flame and hinder the heterogeneous reactions of the captured soot. This prevents further changes in the soot morphology after particles have impacted on the cold surface [16]. The positioning of each sampling height is determined by aligning the TEM grid to the laser extinction beam at flame centerline before combustion. Sampling starts at HAB 9 mm and ends at HAB 17 mm with 2 mm intervals, resulting in a total of 5 representative samples per flame test condition.

Magnification of soot aggregates on the TEM grid is done via transmission electron microscopy. The sampling grid is examined with a transmission electron microscope (Philips Model CM100), equipped with a side-mounted digital camera, which has a point-to point

resolution of 0.24 nm. TEM magnifications used for the present measurements are 10,500 and 64,000. The higher resolution of 64,000 is instead employed for present measurements to obtain clearer representative samples of soot aggregates (See APPENDIX A.7). In spite of the 3 mm diameter sampling grid, the actual analysed area under the electron microscopy is less than 0.01 mm². The TEM photographs are digitized with a scanner and saved on a personal computer as tagged image format (TIF) files for statistical analysis. These images are quantitative analysed using an imaging analysis software (analySIS[®], Olympus Soft Imaging Product). Each magnified digitized image is converted from pixel size to nanometer scale using a calibration scale of 200 nm. The image quality as opposed to those made from silicon oxide, produced a higher contrast ratio [16]. This allows statistical analysis such as size and morphology to be performed for soot particles as a function of flame co-ordinates. Primary particle diameters are measured in terms of apparent sphericity of the soot particles near the periphery of soot aggregates.

6.4 Results and Discussions

Thermophoretic sampling followed by TEM analysis is performed for four flame test conditions at five sampling heights. TEM micrographs are further magnified by 64,000 times for closer inspection at soot structure. Mean primary size diameters are determined from the apparent spherical shape of the soot particles near the periphery of soot aggregates. It is found that soot particles are near spherical at low heights but aggregate in later stages of the flame. The characterisation of these particles at different stages of the flame is considered.

6.4.1 TEM Micrographs

Figure 44 shows a series of TEM images of soot samples obtained at five sampling heights for $\text{Ø} = 1.82, 2.22, 2.84$ and 3.80 . These representative results are initially taken at a previous resolution of 10,500 but magnified to 64,000 times to provide a closer examination of particle sphericity and occurrence. It is apparent that there exists two types of soot with different physical and chemical structures in the flame [17, 132]. The first type is referred to as precursor particles, translucent under the electron beam (See Figure 44 (a) and (b)). The second type is the commonly known carbonaceous aggregates whereby amorphous soot graphitizes into carbon material and consists of agglomerated mono-disperse spherical particles (See Figure 44 (c) to (e)).

TEM photographs in Figure 44 (a) and (b) reveal near spherical primary particles at low and intermediate heights are made up of precursor particles with non-uniform sizes. These

precursor particles transition into larger primary particles with a higher definition in sphericity and uniformity with increasing opaqueness at HAB 13 mm (Figure 44 (c)). This results in a broadening of the size distribution and reduction in number concentration of aggregates after inception as reasoned by Dobbins and Megaridis [16]. As the primary particles progresses upward, a varying number of these particles undergo carbonisation to mature soot by colliding and sticking to form agglomerates in Figure 44 (d). The presence of only Type 2 (opaque) particles observed at HAB 17 mm in Figure 44 (e), implies that particle inception has ceased and results in a decrease in aggregate concentration by coagulation. The dominant growth of soot at this stage is possibly from surface growth. Consequently, it is noted that the effect of particle carbonization may affect bulk density and refractive index [17] due to apparent physical and chemical changes of soot morphological throughout the flame.

The degree of aggregation is subjected to mean number of primary particles per agglomerate with increasing residence time and propensity to soot. It can be clearly seen in Figure 44 from HAB 13 to 17 mm for all flame conditions onwards; the agglomerates start to develop into either straight or branched chains and gradually form “fluffy” soot flocculates. As a function of soot propensity at HAB 17 mm, all soot particles are strongly agglomerated at $\phi = 1.82$ which opposes differently to fuel-richer conditions at $\phi = 2.84$ where soot particles exhibit coagulation with a relatively constant occurrence instead. This is attributed to the transport effects of insufficient oxygen which is needed for surface growth and soot loading [28]. For both conditions, this is followed by a phase of soot oxidation into gaseous products such as CO_2 and H_2O at longer residence times whereby the large clusters exhibit smaller dominance of primary particle size and a higher degree of agglomeration. In this case, $\phi = 1.82$ in Figure 44 (e) display lesser number of agglomerates with smaller base units than that of fuel-richer counterpart and had been observed in the past [132].

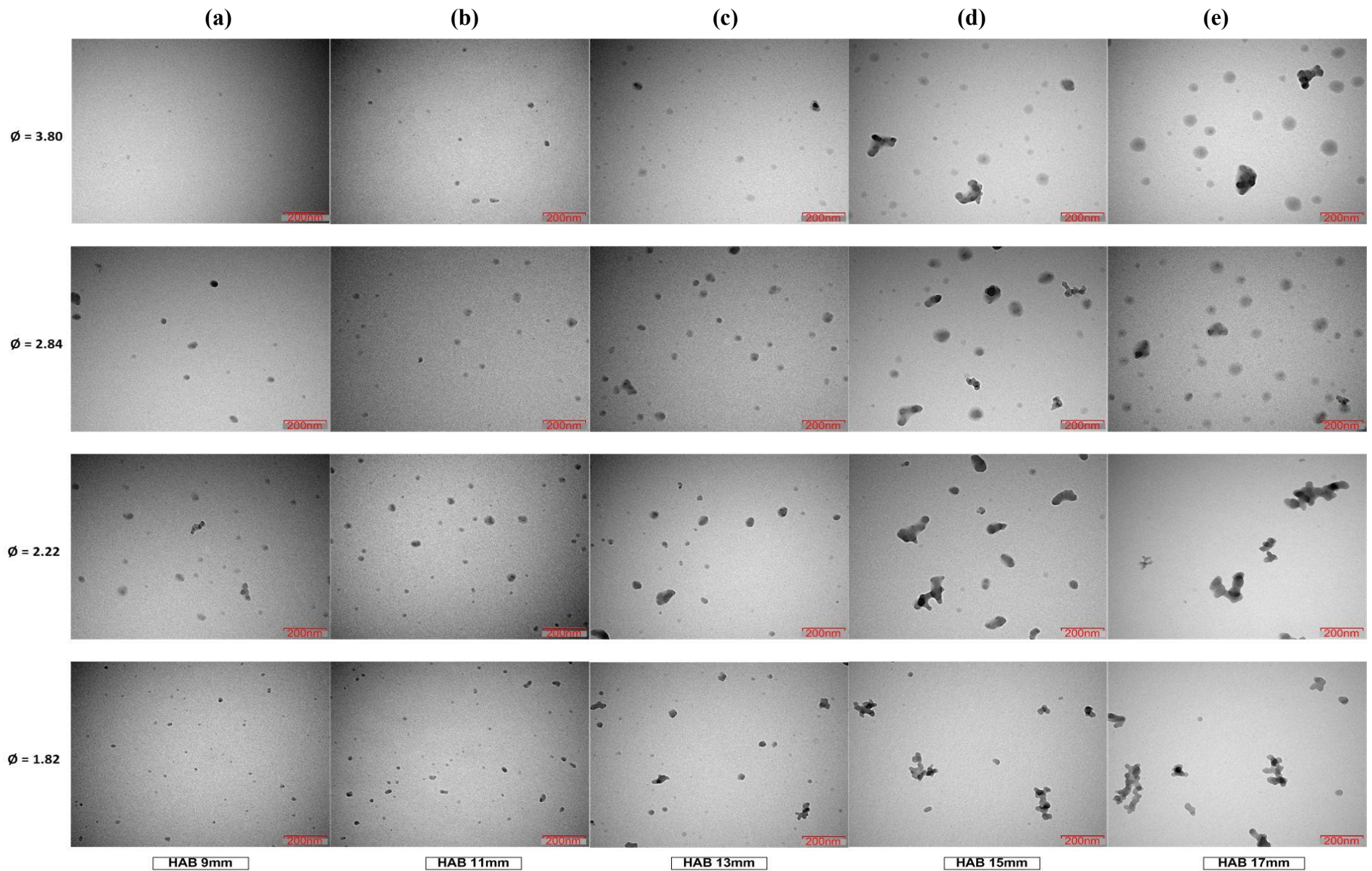


Figure 44 TEM photographs (with a resolution of 64,000) of soot sampled at $\text{Ø} = 1.82, 2.22, 2.84$ & 3.80 as function of HAB at (a) 9mm, (b) 11mm, (c) 13mm, (d) 15mm, (e) 17mm

6.4.2 Particle Size

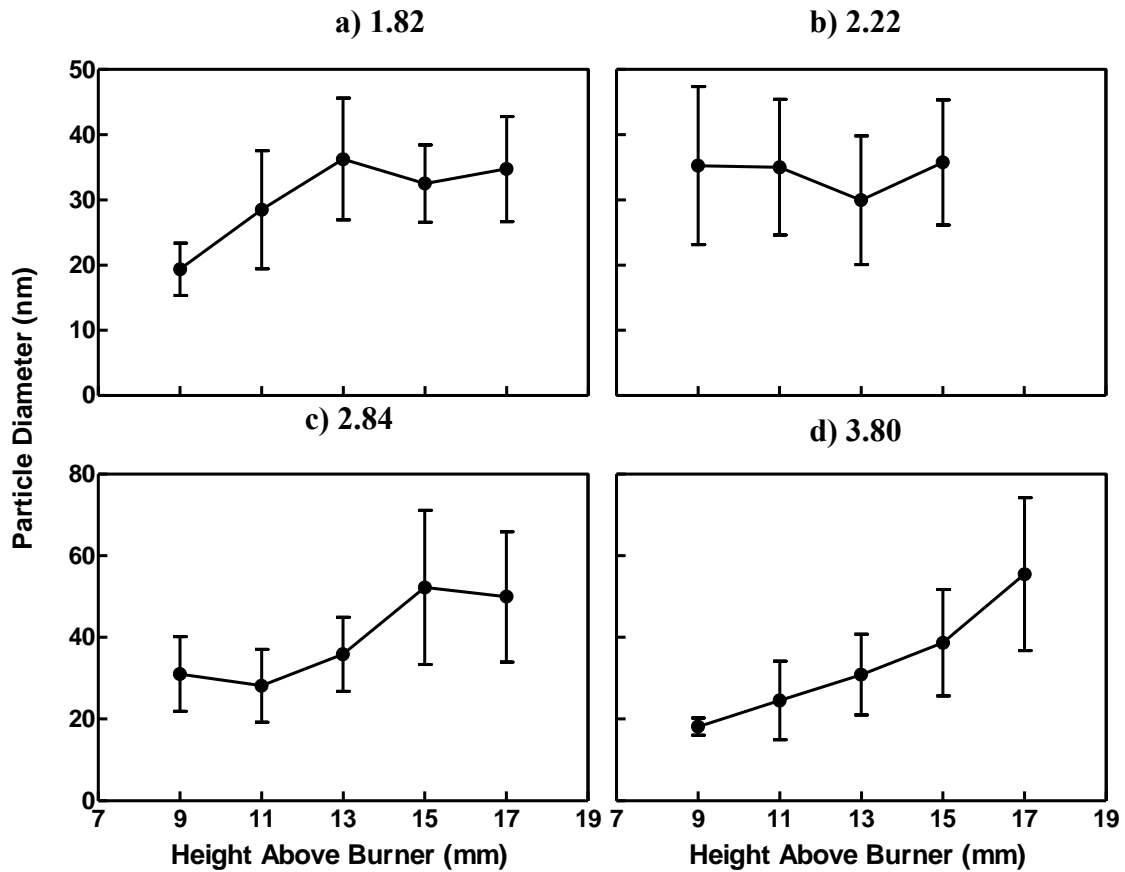


Figure 45 Mean particle size diameter as function of HAB as determined from TEM Photographs at (a) 1.82, (b) 2.22, (c) 2.84, (d) 3.80. (Note: black lines: standard deviation error bars)

Primary size diameter (d_p) is determined by identifying the apparent spherical shape of the soot particles near the periphery of soot aggregates. Figure 45 compares the average primary particle size profiles at flame centreline as visually determined from TEM images for all four flame test conditions. Size measurements are averaged in each TIFF image per HAB with their error bars corresponding to the standard deviation of the mean size distribution.

There is no obvious trend in the soot primary size distribution as a function of burner height. It is observed that mean particle diameter increases with distance from burner surface for the majority of the investigated flames. This trend coincides with soot volume fraction measurements previously performed by laser extinction (See Figure 14). Soot inception occurs at low height in the flame and develops in size by surface growth and coagulation [124]. The primary particle size increases as the particles move towards higher regions of the flame. At the peak of HAB 15 mm, „young“ soot primary particles undergo carbonisation to mature soot in Figure 44 (d). This presents difficulty in visual measurements as the spherical primary particles collide and stick closely. These agglomerates continue to grow in nature by

surface growth and cluster-cluster aggregation [127, 133]. The continual growth of these aggregates may result in densification [17, 133] as observed by the slight drop shown in Figure 45 (c) at HAB 15 mm. However, other flame test conditions reflect otherwise. Due to the complex interactions among soot nucleation, surface growth and oxidation, the progression of a typical primary soot particle is difficult to predict.

6.4.3 Soot Structure

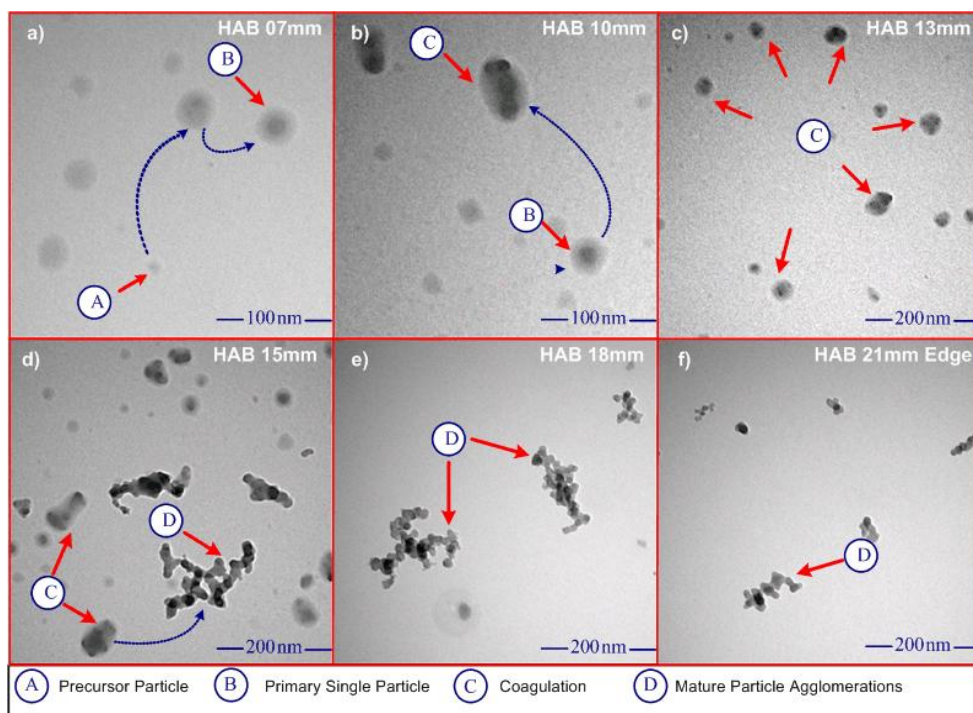


Figure 46 Primary particle development at $\text{Ø} = 2.84$ for six HABs on flame centreline

Figure 46 describes the particle structure and density for six HABs measured at flame centreline at $\text{Ø} = 2.84$. It depicts the five different states of soot evolution: (A) inception, (B) surface growth, (C) coagulation and (D) agglomeration as previous reported [114, 134]. From Figure 46 (a) and (b), it is easily seen that the particles are not clearly defined and that they are suggested to be surrounded by a clear film which is best described as a “halo” [114]. This “halo” is a resultant effect of liquid-like particles which flattens after sampling and gives a three-dimensional hill-like structure. Nonetheless, these single particles still exhibit near spherical structure during soot inception at near burner surface. The transition in particle mass from Figure 46 (b) to (c), is mainly attributed to the PAH model addition hypothesis [95, 121]. This causes a rapid broadening of the size distribution and a gradual reduction in number concentration. Later, the primary particles undergo further surface growth by cluster-cluster aggregation better described as agglomerates in Figure 46 (d) and (e). This surface growth effect is due to the heterogeneous reactions on the exposed surfaces of primary

particles that cause material deposition whilst retaining their near spherical form [16, 133]. At this stage these agglomerates are more of carbonaceous material; commonly referred as Type 2 particles [17]. As the mature soot progresses higher towards the flame, TEM image at HAB 21 mm at radial edge in Figure 46 (f) shows only mature aggregates with smaller particle distribution at a diminished occurrence rate. This significant loss of soot material with increasing height shows that oxidation reactions have taken place. Final products such as CO, CO₂ and H₂O are usually formed in the process.

6.5 Summary

The thermal oxidation of hydrocarbon fuel into mature soot particulates was investigated. It follows a series of elementary steps starting from particle inception to surface growth to carbonisation. The inception process is responsible for the formation of the 1st PAH via acetylene addition and PAH recombination, undergoes coagulation into a base unit. The nascent particle undergoes surface growth by H-abstraction-C₂H₂-addition (HACA) mechanism as suggested by Frenklach and Wang [24]. The continual growth and collisions of these particles into chain-like structures, observed at longer residence times, are defined as agglomerates. To determine their size and morphology, thermophoretic sampling particle deposition (TSPD) was employed. The technique is based on a simple and rapid insertion of a porous sampling grid into a flame. The deposited soot on the grid is subsequently examined under transmission electron microscopy. Statistical analysis on the soot particle size diameters and soot structure can thus be conducted. The results are as follows:

- 1) The TSPD method was able to yield vital information about soot structure in premixed flames. At low HABs, there was a dominant presence of small spherical primary particles described as Type 1 particles. As these particles moved higher towards the flame, they underwent heterogeneous surface reactions and cluster-cluster aggregation into carbonaceous material. Number concentrations of agglomerates differed in terms of fuel equivalence and oxidation effects.
- 2) There were no obvious trends in the particle size distribution. Mean particle diameters increased as a function of height. The observed trends were similar to previously performed soot volume fraction measurements by laser extinction.
- 3) A clear film is observed to surround the soot structure at low HABs which is described best as a “halo”. Coagulation of soot particles increases size distribution and reduces

number density. The carbonaceous aggregates were commonly referred to as Type 2 particles.

- 4) The distinctive ability of TSPD is that it is able to identify each type of soot particle and subsequently be measured for size and morphology.

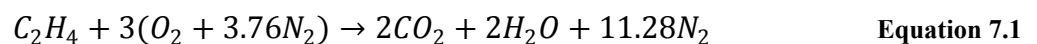
7 COMPUTATIONAL MODELLING

The chemical reactions involved in combustion are aplenty and sometimes complex in nature. To resolve this issue, kinetic modelling is usually carried out. This chapter reviews the kinetic hierarchy of hydrocarbon oxidation and identifies relevant intermediate species essential for soot formation. The descriptions and advantages of using CHEMKIN[®] for this study are addressed. Discussions relating to PAHs formation and their mass growth to soot are considered. Sensitivity analysis is determined to observe the impact of temperatures on chemical species.

7.1 Chemical Kinetics

In order to comprehend the principles of combustion, it is essential to understand the chemical kinetics behind it [45]. Combustion involves two types of reactions: global and elementary. A global reaction depicts an overall reaction of the fuel and an oxidiser to form combustion products whereas an elementary reaction involves breaking or formation of possible intermediate species. The cumulative of these elementary reactions eventually lead up to form the global reaction.

The global reaction for ethylene combustion maybe expressed as:



Even though this reaction appears quite straightforward, Westbrook and co-workers [135] have determined this global reaction to pertain about 93 elementary reactions among 26 chemical species within laminar flames. This global reaction is later modified by Wang and Frenklach [21], subsequently by Appel and co-workers [19] to accommodate 100 chemical species with 544 elementary reactions to better describe ethylene and acetylene oxidation at atmospheric, taking place within the overall reaction.

A greater understanding into the construction of a reaction mechanism must be considered as many of the reactions do not occur or occur with very small rates. The combustion of hydrocarbon fuels consists primarily of sequential fragmentation of the initial fuel molecule into smaller intermediate species which are then converted into final products, usually H₂O and CO₂ [136]. In many cases, these intermediate species can be fuels themselves [136]. For

instance, ethylene (C₂H₄) is the main intermediate in the combustion of propane (C₃H₈) and higher hydrocarbons, but it can also undergo thermal decomposition as main primary fuel.

Figure 47 Simple hydrocarbon fuels oxidation mechanism hierarchy [136]

The oxidation of H₂ and O₂ plays a predominant part in the process of hydrocarbon combustion [33]. It consists of the four well-known chain reactions producing active particles H, O, OH and their reverse reactions which form the basis of hydrocarbon oxidation. They are:



These basic steps can be used in great advantage towards establishing complex kinetic mechanisms for higher hydrocarbon fuels shown in Figure 47. If the fuel is of higher complexity, it will decompose first before undergoing the basic sub-elements towards the top of the hierarchy.

The thermal decomposition of ethylene into smaller hydrocarbons can be similarly described by ethane oxidation at atmospheric in Figure 48. One of the important intermediates in C₂ species is methyl (CH₃) radical which is seen to be in the destruction path of methane and ethane. Another important radical common to all hydrocarbon oxidation is formaldehyde (CH₂O). It can be seen predominantly in pyrolysis of both methane and ethane oxidation and also identified as the third main body in the mechanism hierarchy in Figure 47. In the pyrolysis of C₂-hydrocarbons, the fuel undergoes H-abstraction for each sub-element down the mechanism with the formation of intermediate species leading up to CO and CO₂. Evidently, the hierarchy of a simple hydrocarbon oxidation can be made complicated by the

introduction of a higher hydrocarbon fuel and hence affect judgement on the reaction pathways.

Figure 48 Reaction mechanism for a stoichiometric C₂H₆-air oxidation [137]

7.2 Flame Radicals

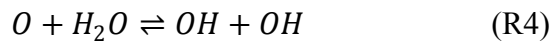
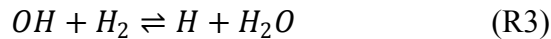
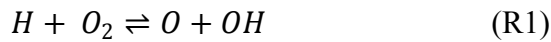
Intermediate species or free radicals are molecular fragments comprising of one or more unpaired electrons in its outer structure. These unpredictable radicals must undergo recombination elementary reactions within the main combustion zone chemistry to convert into stable species. Importantly, the formation and interaction of these radicals are fundamental to the flame structure and largely determine the global properties of the flame. Especially ethylene combustion, some of these intermediates may include: H, O, OH, CH, CH₂, CH₃, amongst many others. Below listed are some of the important radicals vital to the formation of polycyclic aromatics hydrocarbons. Corresponding reaction kinetics data and reaction numbers are taken from Wang and Frenklach [21].

7.2.1 Hydroxyl Radical (OH)

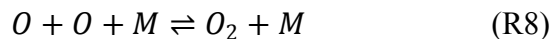
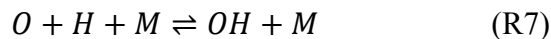
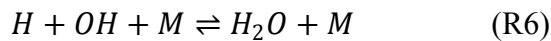
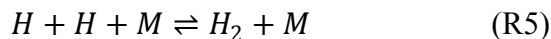
Hydroxyl (OH) radical is an important precursor towards combustion chain chemistry. Referring to Figure 47, it is apparent that the basis for any hydrocarbon fuel oxidation must undergo a $H_2 - O_2$ submechanism, among which OH radicals are evolved. It is also one of the main contributors towards the chemiluminescence effect observed in hydrocarbon flames [32]. In addition, the reactive nature of OH radicals near burner surface has been known to oxidize soot in excess [54]. Due to its importance to both physical and chemical combustion chemistry, therefore numerous investigations into OH radicals have been carried out.

The important reactions for hydrogen oxidation and their rates have been extensively studied and documented [136, 138, 139]. A total of 19 elementary reactions describe the oxidation of H_2 . The elementary reactions for hydrogen oxidation follow the chain-branching and terminating steps that results in the evolution of O, H and OH radicals.

Chain-branching reactions:



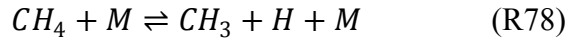
Chain-terminating reactions:



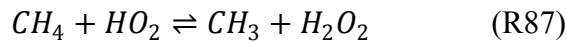
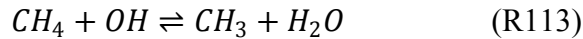
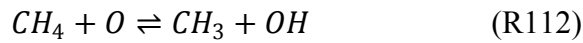
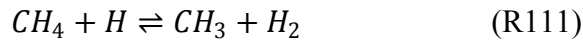
where M refers to any available third body species, required to conserve both momentum and energy as reported [136]. In lean and moderately rich hydrocarbon flames where high temperatures are usually encountered, the combustion chemistry reaction rates are mainly controlled by two elementary reactions; (R1) and (R24) [137, 139]. The chain-branching steps of the oxyhydrogen reactions produce alkyl radicals with high concentrations of CO_2 [136]. Any other competition that interferes with reaction (R1) would serve as hindrance to OH production and hence inhibit combustion.

7.2.2 Methyl Radical (CH₃)

The formation of methyl (CH₃) radicals is a direct resultant from decomposition of methane at high temperatures. Due to its lack of carbon-carbon bonds and low sooting nature, methane flames are often used as a useful platform for evaluating aromatics formation mechanisms [140]. Methane primarily undergoes thermal decomposition to form methyl radicals [136]:



Formation of methyl radicals not only occurs through via H-atom abstraction from methane, but also evolved from other several reactions, including [136]:



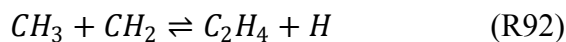
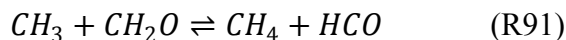
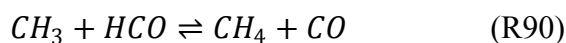
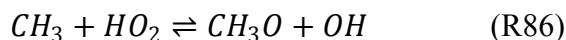
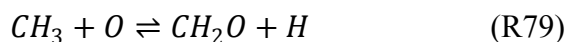
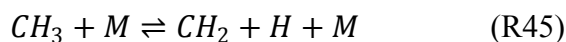
It was established that the most important secondary process in the consumption of methyl radical consumption is radical-radical recombination reaction [136]. About 30 % of methyl radicals are consumed by recombination in lean or stoichiometric flames, with the percentage increasing to 80 % in fuel-rich flames [33].



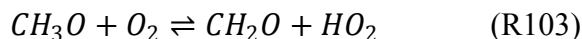
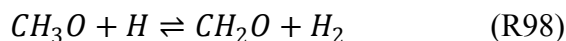
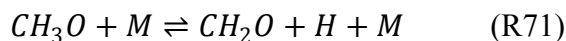
Ethane formed by methyl recombination reaction, decomposes to less saturated C₂ hydrocarbons. This is then followed by a complex network of coupled larger hydrocarbons (C₂ +C₁, C₂ +C₂, etc.) consisting of two or more carbon atoms which possibly leads to the formation of benzene precursors [140]. One of these examples is the global reaction of cyclopentadienyl radical with methyl radical into benzene [141] as shown in Figure 49.

Figure 49 Schematic diagram of cyclopentadienyl radical reaction with methyl [140]

Methyl radicals may dissociate at very high temperatures (R45) or may be consumed through a variety of channels [136]:



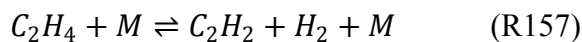
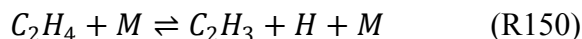
It is apparent from this set of reactions that methyl radicals continue to undergo chain-branching reactions to form formaldehyde (CH_2O) radicals and even form stable ethylene intermediates. Formaldehyde (CH_2O) radicals are further enhanced by the rapid decomposition of methoxy (CH_3O) radicals [136]:



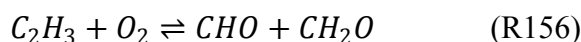
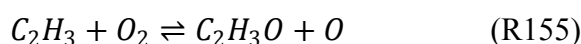
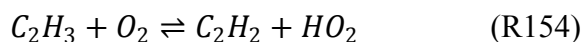
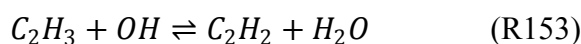
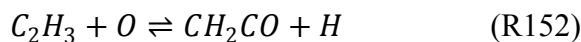
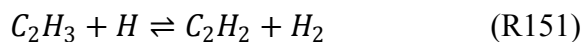
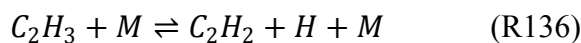
7.2.3 Vinyl Radical (C_2H_3)

The vinyl (C_2H_3) radical is the first critical intermediate identified in ethylene combustion process [19]. Ethylene not only acts as a key intermediate to the combustion of higher hydrocarbons but it also lends itself as a primary fuel. Comprehensive reaction mechanisms involving ethylene oxidation and pyrolysis over a wide range of operating conditions, including shock tubes, laminar flames and plug flow reactors have been well-documented and modelled [135, 142]. The importance of ethylene and acetylene towards the formation of soot has been studied in great details [2, 19, 119, 122]. Even substantial kinetic modelling has been demonstrated to realise the importance of C_2 hydrocarbons towards the formation of the first polycyclic aromatic hydrocarbons (PAHs) [20, 22, 143, 144].

Ethylene undergoes thermal dissociation to form vinyl radicals [136, 145]:



where the reaction rate of (R157) proves to be the fastest among the two. Further decomposition and oxidation of vinyl radicals yield stable products such as acetylene (C_2H_2), formaldehyde (CH_2O) and ethanol (C_2H_3O) [21, 136].



The reaction sequence of (R136) and (R151) forms inert H_2 in the coolest part of the flames, which may affect thermal diffusion [146]. Since concentrations of vinyl radicals are little, additional reactions of (R152) and (R153) do not occur as often as opposed to reactions (R136) and (R154) [136]. The rate constants of reactions channels of (R154 – 156) have been modified, as recommended by Miller and Melius [20], to better agree Appel-Bockhorn-Frenklach (ABF)'s model [19] with experimental data.

7.2.4 Propargyl Radical (C_3H_3)

Computational simulation of fuel-rich premixed flames that involves detailed chemistry kinetics and aromatic formation has been of concern lately. The main fuels of interest include ethylene [22], acetylene [20] or even both [19, 21]. All of the simulations concluded that the propargyl recombination reaction is the major benzene/phenyl formation route. In one scenario, benzene is indirectly produced by a sequential H-atom addition to phenyl [20, 22]; whereas in another scenario, benzene is directly produced [19, 21]. Despite the complexity of propargyl radicals' self-reactions, it still underlines as the main dominant route towards formation of polycyclic aromatic hydrocarbons.

Propargyl (C_3H_3) radicals belong to a group of resonantly-stabilised free radicals that possess multiple electronic structures that correspond to the same nuclear structure [147]. For each species, the two structures exist with the same number of carbon and hydrogen atoms, but differ in the single bonds rotation on the radical site and higher order C-C bonds as shown in Figure 50.

Figure 50 Resonantly-stabilized radicals with multiple electronic configurations [140]

These resonance hybrids are much thermodynamically stable than non-resonant radicals. The formation of such resonant structures results in the delocalized of an unpaired electron. This implicates the resonantly-stabilised radicals into forming weak bonds with stable molecules [20]. The net result from the formation of such free radicals may accumulate to such high concentrations [148] that it is suggested that the recombination of resonantly-stabilised propargyl radicals forms the basis of the first aromatic ring in flames [20, 22, 148] in Figure 51. Similarly, both cases require H-atom isomerization.

(R227)

(R227')

Figure 51 Schematic diagram of propargyl recombination channels that form single-ring aromatic hydrocarbons [140]

7.3 Computational Procedure

A flexible but powerful computational approach is needed to simulate complex gas-phase kinetics in premixed flames. CHEMKIN[®] is one such software to do so. Literature reviews into the PREMIX flow model, Appel-Bockhorn-Frenklach gas-phase mechanism and the relationship of these elements into CHEMKIN[®] are presented. An outline of this computational approach using experimental temperatures as estimates is discussed.

7.3.1 CHEMKIN Software

The lack of access to generic data or information pertaining complex chemical reactions in different combustion configurations has recently given rise to the development of CHEMKIN[®] [30]; a software compatible with open-source libraries to tackle the information gap. This holistic approach is specifically developed for simulation of detailed chemical kinetics in various experimental scenarios with minimal time and effort. CHEMKIN[®] once originated as a combustion code from Sandia National Libraries before gradually evolving into a modern-day user-friendly interface that offers better performance in calculation speed and accuracy. CHEMKIN[®] is designed to analyse chemical kinetics and molecular transport, especially in processes that involve chemically reacting flow and heterogeneous reactions at surfaces. CHEMKIN subroutine libraries [149] are designed to use thermodynamic and

transport data from open-source libraries to provide relevant data for combustion modelling. These open-source libraries bridge the gaps between different levels of combustion regardless of flame combustion or 0-D (Closed homogeneous and PSR; steady-state and transient) reactors. Some recent examples of similar community-wide efforts to construct open-source software or data libraries for CHEMKIN[®] are GRI-MECH version 3.0 [150], Konnov Release 0.5 [151] and Appel-Bockhorn-Frenklach (ABF) gas-phase combustion mechanism [29].

The application of CHEMKIN[®] has been a long running standard for the description of reactions, thermodynamics and transport properties. It is important to note that present version of CHEMKIN 4.1 reacts much faster than CHEMKIN II [152], when tested out using identical reactor models and mechanisms. On the other hand, solver enhancements in CHEMKIN-PRO even offer better solution speeds over CHEMKIN 4.1 shown in Figure 52. Benchmarks for all cases were run using the same Linux 64-bit platform.

Figure 52 Solution speed comparisons between different versions of CHEMKIN[®] (Linux 64-bit Platform)

One of these enhancements in modern CHEMKIN includes Freely Propagating (FREE) and Burner-Stabilized (BURN) flame reactors which oversee significant performances in initial conditions in setup and heat-loss specification options. Another capability of CHEMKIN-PRO is its Particle Tracking feature where particle nucleation, coagulation and surface growth

can be numerically simulated. Unfortunately, economic strain has limited present study to only undertake CHEMKIN 4.1.1, absence of soot particle tracking and reaction path analysis.

7.3.2 Flame Code

CHEMKIN[®] software has been the forefront for past kinetic modelling studies, particularly in the combustion of aliphatic hydrocarbons. These studies usually involve predictions of species concentration profiles in fuel-rich premixed flames [2, 19, 21, 22, 26, 153] and even extend to fuel-lean mixtures as well [50]. All simulations employ the PREMIX [154] flow model which is primarily for burner-stabilized premixed laminar flames. PREMIX or “BURN” flame code computes the concentration profiles using cold mass flow rates through the burner, feed-gas compositions, pressure, and an estimated solution file as input. Figure 53 shows such an arrangement from inlet source to “BURN” program to product outlet in CHEMKIN 4.1.1.



Figure 53 Simulation pathway in PREMIX flame code

Coupled with thermochemical information from CHEMKIN[®] database [149] and open-source libraries such as ABF combustion mechanism [29], insight into the complex chemical kinetics behind laminar premixed flames can thus be observed. Additional information such as solution grid parameters and iteration values has to be determined prior to simulation convergence.

Simulation of chemical species profiles can be made easy if temperature measurements in sooty regions are available. However, in sooty-free regions (HAB 0 – 3 mm), it is necessary to estimate temperature distributions near burner surface in order to complete calculations. Linear extrapolation of the measured temperatures to the burner surface is carried out, assuming unburnt exit mixture to be at 298 K. Significant heat losses to the environment are taken into account as it might impede the correct modelling of well-defined laminar flame conditions. As a result, no significant changes are made to the species concentration in the soot formation region.

7.3.3 Program Structure

To fully understand the solution convergence behind PREMIX, a thorough awareness of the relationship between CHEMKIN[®] and thermochemical database such as thermodynamics and transport properties must be known. As reported in Kee and co-workers [154], PREMIX program runs in conjunction with CHEMKIN 4.1.1 software and TRANSPORT [149] subroutine libraries. In order to solve for PREMIX, the user must execute two pre-processor programs that have access to thermodynamics and transport databases. Figure 54 reflect the relationships between the gas-phase mechanism, thermodynamic and transport databases to the PREMIX flame code.

Figure 54 Relationship of PREMIX program to CHEMKIN and TRANSPORT pre-processors, and to the associated input and output files [154]

PREMIX is written as a subroutine directive that opens all appropriate linking files, input parameters and allocates the working storage before activating the flame code through its subroutine interface. Before PREMIX can start to define the flame chemistry and its associated chemical reactions, the CHEMKIN Interpreter or „chem.exe“ has to be performed first. The Interpreter first analyses the user-supplied gas-phase mechanism which then extracts relevant information about the chemical species“ thermodynamic properties or „therm.dat“. This information is stored in the CHEMKIN Linking File or „chem.asc“ which subsequently

activates TRANSPORT property fitting program, „tran.exe“, and later by CHEMKIN subroutine library. Similar to CHEMKIN Interpreter, the TRANSPORT property fitting program produces a Linking File „trans.asc“; its purpose is to evaluate the polynomial representations of the temperature-dependent parts of the individual species“ properties such as viscosities, thermal conductivities and binary diffusion coefficients. Combined with solver parameters (APPENDIX B.1), PREMIX will proceed to read both CHEMKIN and TRANSPORT subroutine libraries and set up the internal working and storage space needed by all subroutines in the libraries. Consequently, the flame code will produce a printed output and saves the solution in a binary save file. Alternatively, this binary save file can be used to restart PREMIX as a starting estimate for different flame conditions.

7.3.4 Gas-Phase Mechanism

An accurate description of a laminar premixed flame structure requires a detailed chemical kinetic model based on reliable predictions on major and minor species development in soot formation. Recently, detailed studies of soot formation, involving the formation and growth of polycyclic aromatic hydrocarbons (PAHs), in laminar premixed flames of C₂ hydrocarbons have been looked at [19, 21]. For this present study, the Appel–Bockhorn–Frenklach (ABF) mechanism [19], previously developed by Wang and Frenklach [21] or WF model, is employed as the main chemical kinetic gas-phase mechanism required for PREMIX modelling. It has even been extended to include numerical modelling of soot particles via Method of Moments [155]. However, this modelling step is only available in the aforementioned Particle Tracking feature of CHEMKIN-PRO.

The ABF gas-phase mechanism consists of 544 reversible elementary reactions among 100 chemical species. As cited in their work [19], the updated mechanism describes the pyrolysis and oxidation of C₁ and C₂ species, formation of higher hydrocarbon up to C₆ species. It includes the formation of benzene and phenyl by reactions of C₄ species with acetylene, cyclization reactions with C₆ species and propargyl recombination reactions. The formation of pyrene starting with benzene follows the reaction sequence of H-abstraction-C₂H₂-addition (HACA) mechanism, along with ring-ring “condensation”. The H/O, C₁H_x and C₂H_x sub-mechanism in ABF mechanism was partially taken from GRI-MECH version 3.0 [150] by which minor improvements are made to better describe acetylene and ethylene oxidation. The reaction channels and rate coefficients for the even-carbon-atom aromatics formation and the HACA growth are those of Wang and Frenklach [156], improved with a set of thermodynamic data [157] and transport properties [158] of aromatic species. The odd-carbon-atom formation of the first aromatic ring is widely accepted to be propargyl-propargyl

radical recombination [148] and is treated as an overall, single irreversible step with the rate constant fitted to the ABF model.

7.3.5 Computational Outline

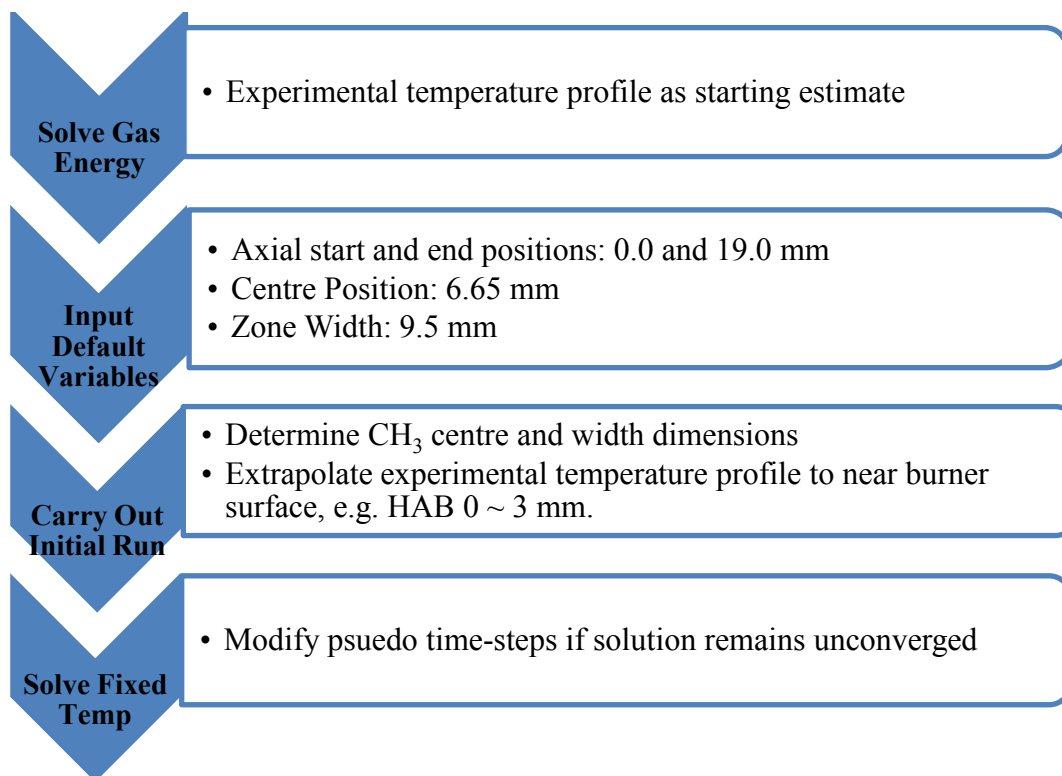


Figure 55 PREMIX procedural outlines

All computations are performed using CHEMKIN 4.1.1. and PREMIX [154] flame code. A step-by-step procedure involving experimental temperature profiles as starting estimates is outlined in Figure 55. Thermodynamic [157] and transport [158] properties of aromatic and non-aromatic species are taken from the ABF mechanism. All flame calculations are performed with correction velocity formalism on the convective terms with windward differencing, and multi-component diffusion formulas, and include H and H₂ thermal diffusion [154].

Experimental temperature profiles are introduced as starting estimates to eliminate significant heat losses which are often difficult to determine. By doing so, it will eliminate the need to model heat losses in the gas energy equation computation. Elaborate details of the modified Newton's method, Jacobian matrix equations, multi-component transport properties and finite difference approximation are provided [154]. Prior to any calculations, the energy equation requires initial estimations of grid approximations and input variables. This is supplied with 381 adaptive mesh points with maximum gradient and curvature set at 0.1 each. Additional

estimations of the combustion zone, such as centre position and zone width, are given to complement the energy equation iteration. Actual mass flowrates from premixed cold gas inlet are specified for inlet stream property with assumed mass fractions of $C_2H_4/O_2/N_2$ as reactant species" compositions. Combined with solver parameters (APPENDIX B.1) in both modified Newton"s method and Jacobian matrix, PREMIX initializes CHEMKIN and TRANSPORT subroutine libraries to create starting estimates for computations.

Once the gas energy equation has been determined, relevant information from intermediate species and extrapolated-temperature profiles can be re-used as starting estimates for fixed gas temperature computation. First, starting estimates for location and thickness of reaction zone has to be determined. This reaction zone is assumed to be located where the reactants transition to the product phase, usually involving intermediate species. These intermediates or short-lived radicals are assumed to have a Gaussian profile that peaks in the centre of the reaction zone as depicted in Figure 56. The peak height corresponds to the centre position of the reaction zone whereas the zone width corresponds to the width at $1/10^{\text{th}}$ of the peak value. For this present study, the peak height and zone width of methyl (CH_3) radical is chosen.

Figure 56 Starting estimate to the zone width and centre [154]

Second, by incorporating a fixed temperature profile in the modelling of burner-stabilized flames, the converged solutions offer better reliance to the species" profiles. Kee and co-workers [154] determined that incorrect portrayal of the temperature profile can result in severe non-linearities in the reaction rates of the chemical species. A rough estimation of temperature distribution can be derived from initial energy equation computation from burner surface to HAB 3 mm where thermocouple measurements are inaccessible. Burner surface temperature is assumed to be that of unburnt mixture at 298 K. This revised temperature

profile is later employed as the new starting estimate to fixed gas temperature iterations instead. If iterations results in solution errors, appropriate changes are made to the number and size of the pseudo time-stepping. Preliminary results suggest that any changes to the pseudo time-steps had negligible effects on the concentration outcomes i.e., less than 10^{-7} %.

7.4 Results and Discussions

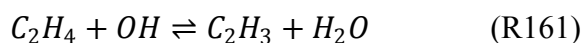
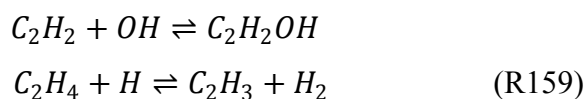
Flame simulations are performed using PREMIX flame code, combined with experimental temperature profiles as starting estimates for CHEMKIN 4.1.1. computation. Appel-Bockhorn-Frenklach (ABF) gas-phase mechanism [29] is used as main chemical kinetic model to better describe the formation of aromatics in laminar premixed C_2 hydrocarbon flames. Observations into some of the minor, intermediate and aromatic species concentration profiles that are actively involved in the formation of PAHs are discussed. References to elementary reactions numbering can be found in both published articles [19, 21].

7.4.1 Minor Species Profiles

The comparisons between respective minor species for a range of flame conditions are shown in Figure 57. These species consist of hydrogen (H), oxygen (O), hydroxyl (OH), methyl (CH_3) and vinyl (C_2H_3) radicals. It is clear that the peak heights of all minor species dominate at low burner heights regardless of stoichiometry. On the other hand, the zone widths are found to increase with soot propensity. The behaviours of OH and H mole fractions are reasonably within estimates of each other and decreases sharply when approaching HAB 5 mm. The production of OH radicals is hypothesized to occur near burner surface via [21]:



whereas concurrent routes towards the removal of OH radicals include: (1) low-temperature OH consumption and (2) ethylene fuel removal by H-abstraction reactions. They are:



This may result in a loss of H and OH radicals near burner surface. However, there are still other unknown reactions that may participate in the H and OH removal in which the current ABF model does not take into account.

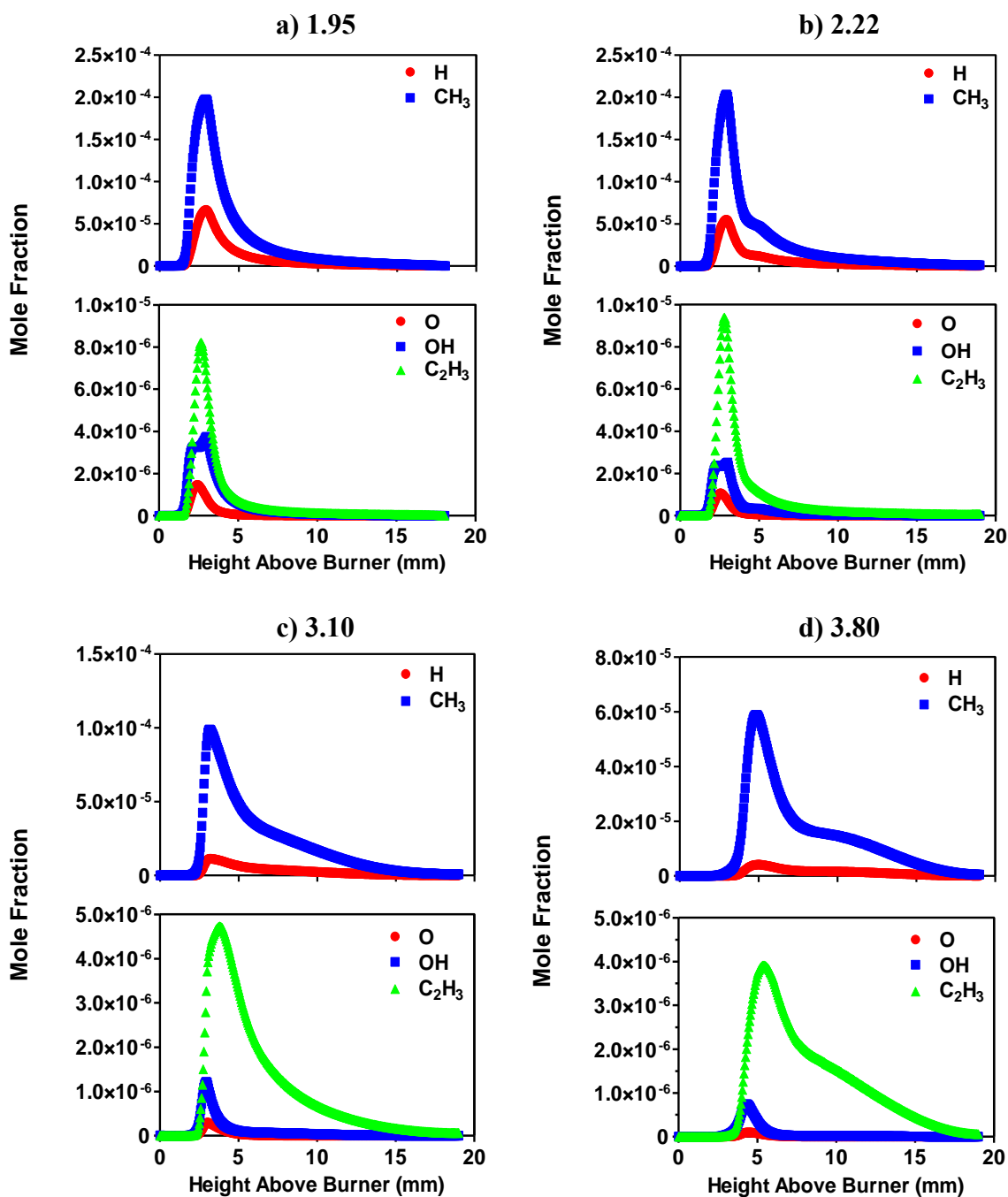


Figure 57 Minor species profiles at a) 1.95, b) 2.22, c) 3.10 & d) 3.80

There exists an indirect relationship between vinyl and methyl radicals. This probably contributed to the loss of H, O, and OH radicals near burner. Possible routes for the formation of methyl radicals have been reviewed [136] as production occurs near burner surface in reactions (R111-113). Referring to Table 6 in APPENDIX B.2, the peak height of the methyl radical increasingly deviates from burner surface with a narrower zone width as a function of equivalence ratio. This results in less area for chemical reactions within the flame. Other implications such as formation of formaldehyde (CH_2O), methoxy (CH_3O) radicals and benzene (A_1) may result in a decrease in their concentrations. Similar to methane oxidation,

ethylene fuel is removed mainly by H-abstraction reactions, (R159) and (R161), to produce vinyl radicals. Oxidation of vinyl radicals by O atoms eventually leads to the formation of methyl radicals via [21]:



Alternatively, the vinyl radicals may undergo additional reactions (R136) and (R151) to dissociate into $C_2H_2 + H / H_2$, essential for soot surface growth.

7.4.2 Intermediate Species Profiles

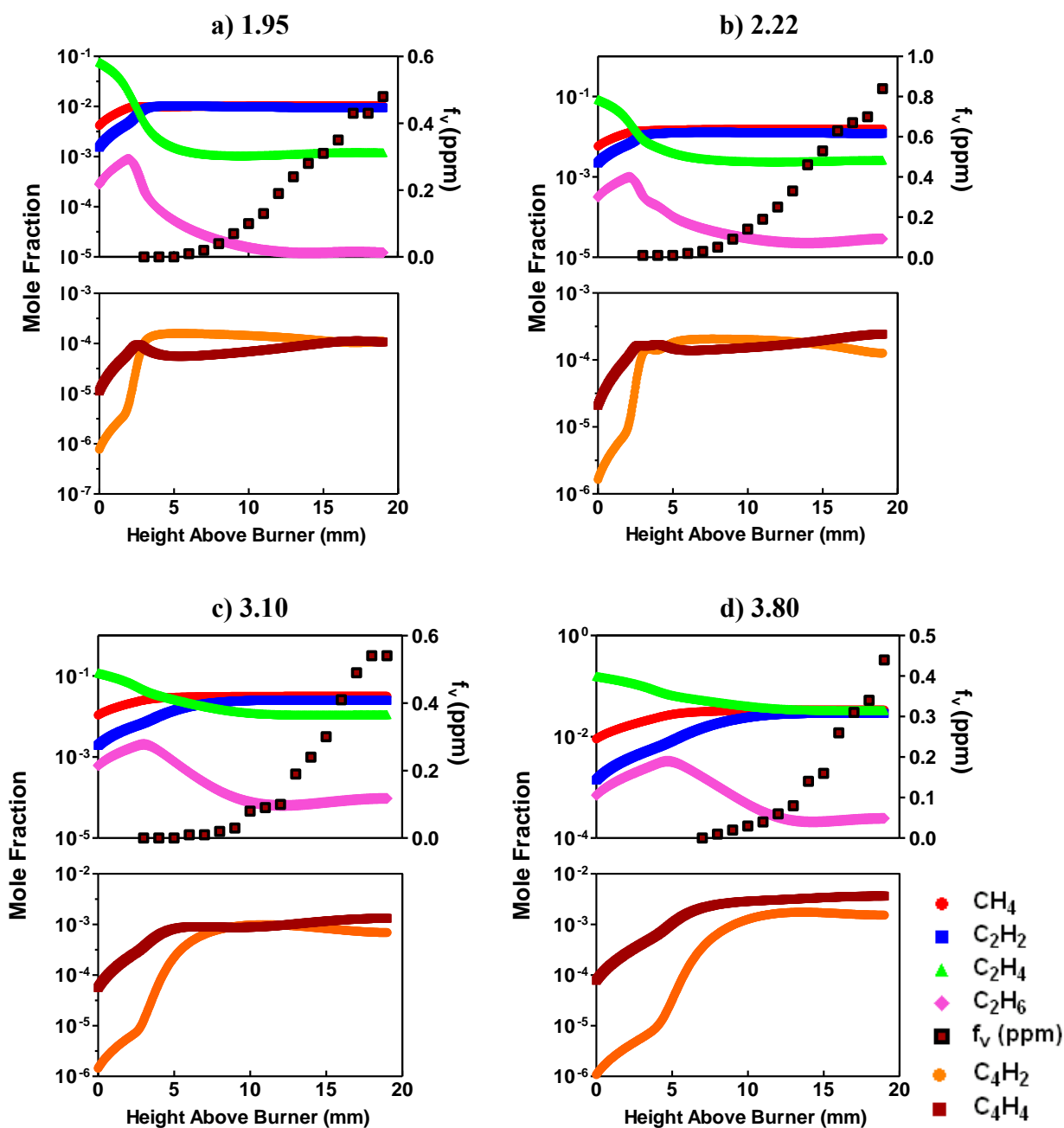
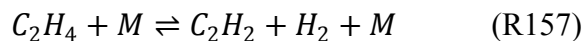
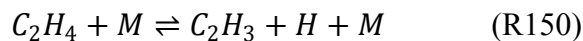


Figure 58 Intermediate species profiles at a) 1.95, b) 2.22, c) 3.10 & d) 3.80

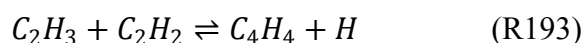
The comparisons between intermediate species in both slightly and heavy sooty flames are shown in Figure 58. The thermal decomposition of ethylene fuel yields C₁ and C₂ and C₄ species through a series of elementary reactions. For C₂ species, it is evident that acetylene (C₂H₂) corresponds closely to methane (CH₄) regardless of stoichiometry whereas ethane (C₂H₆) exhibit a similar trend to that of ethylene (C₂H₄). For C₄ species, propargyl diacetylene (C₄H₂) species demonstrate an immediate increase at HAB 3 mm followed by a gradual decrease near HAB 5 – 10 mm in contrast to that of vinylacetylene (C₄H₄). To observe the effect of acetylene on soot growth, soot volume fraction profiles from laser extinction (Figure 14) is compared as well.

It is established that acetylene is the dominant species that reacts on the particle surface via heterogeneous reactions that results in an increase in molecular mass. This carbon deposition process follows first-order kinetics [71] and often attribute to the mass growth of soot. From Figure 58, it clearly shows that the trends for both acetylene and soot volume fraction are totally different except for near burner surface where there is a gradual increase in both concentrations regardless of stoichiometry. Modelling results seems to suggest that acetylene concentration remain constant throughout the later parts of the flame but these results are loosely based on free-flowing flames stabilised on a burner. In contrast to actual experimental conditions, laminar premixed flames were stabilised in the presence of an overtop burner plate. In addition, the input of reduced temperature profiles as starting estimates and mature soot coagulation are possible factors which may affect modelling results.

The formation of acetylene and vinyl species from ethylene fuel occurs through a series of elementary reactions of decomposition and oxidation which often contributes to the formation of larger species. Ethylene fuel undergoes thermal decomposition through two elementary reactions, namely [145]:

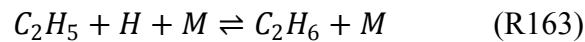
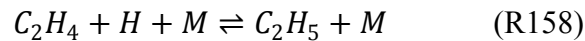


The formation of vinyl radicals from reaction (R150), undergo further decomposition and reactions with other radicals (R151 and R153) that result in the production of acetylene. On the contrary, vinyl radicals may react with acetylene to form vinylacetylene through reaction (R193) via:



This reaction is suggested to be the dominant contributor towards vinylacetylene in low temperature pre-heat zone [21]. Evidently, the immediate increase in vinyl radicals observed in Figure 57 at near HAB 5 mm coincides with vinylacetylene at slightly sooty conditions (ϕ at 1.95 and 2.22) in Figure 58.

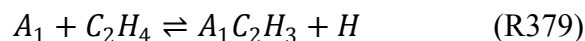
As observed in the concentration profiles of ethylene (C_2H_4) and ethane (C_2H_6), both profiles exhibit the same behaviour but differ by an order of magnitude. This can be elucidated by the formation of ethane via sequential reaction of ethylene via H-addition reaction:



Other reactions with CH_3 or O_2 in low temperature regions [136] may account for the low concentrations of ethane as well.

7.4.3 Aromatics Profiles

Figure 59 shows the comparisons between respective aromatics and their other counterparts in from slightly to heavy sooty flames. The ABF gas-phase describes the formation of the first polycyclic aromatic hydrocarbon (PAHs) and their subsequent growth up to pyrene (A_4). It is evident that aromatic species (A_1 - A_4) exhibit the same trend of gradual increase before levelling-off in all flame test conditions. It is interesting that this same phenomenon was also observed in Figure 58 for methane (CH_4) and acetylene (C_2H_2). The contribution of C_2H_2 to PAH reactants is deemed significant towards soot growth [23]. Present simulations of phenylacetylene (A_1C_2H) and biphenyl (P_2) exhibit behaviours similar to $A_1 - A_4$ aromatics but styrene ($A_1C_2H_3$) in contrast, experience double peaks behaviour instead. This is probably due to the relatively long lifetimes of excited styrene that involves collisional stabilization [159] via:



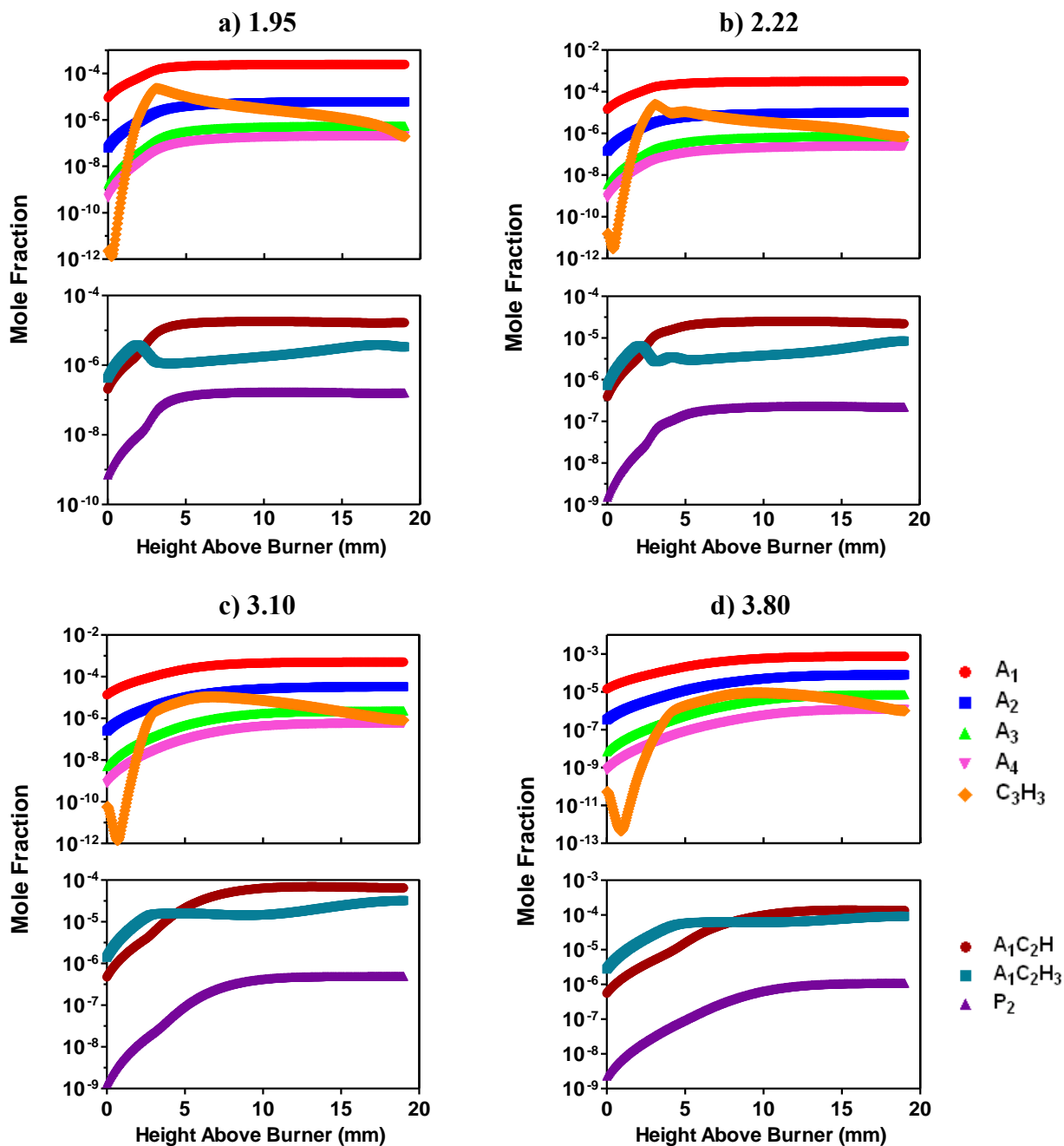
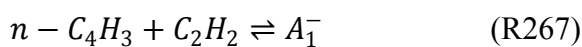


Figure 59 Aromatic species profiles at a) 1.95, b) 2.22, c) 3.10 & d) 3.80

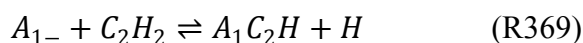
As observed in the work of Wang and Frenklach [21], benzene (A_1) is preceded to be dominated by propargyl recombination reactions in atmospheric ethylene flames via:



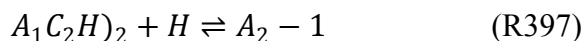
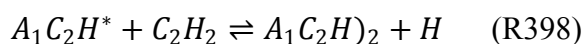
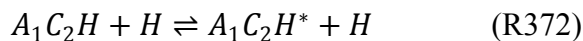
The ABF mechanism predicts that the main bulk of benzene formation takes place in the main reaction zone of ethylene flame through recombination of propargyl radicals, (R227). The

contribution of propargyl (C_3H_3) species towards the formation of aromatics seems to agree reaction (R227) as shown in Figure 59. In all flame conditions, the consensual concentration decrease in propargyl radicals after HAB 5 mm possibly suggests the formation of benzene via propargyl recombination reaction. This reaction has been suggested and accepted to be the main source of benzene in premixed flames [20, 22]. Other contributing reactions such as (R267) and (R365) takes place only in the pre-heat zone (HAB 0 to 2 mm) where temperatures encountered are less than 1400 K in richer flames [21]. Reaction rates for propargyl recombination (R227) occur more rapidly than reactions (R267) and (R365) as they require H atoms in order to proceed. Ultimately, reaction (R227) should be treated as a global reaction for the formation of the first polycyclic aromatic hydrocarbons.

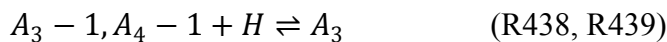
The mass growth of aromatics starts from the partial equilibrium of the phenyl (A_1) reaction with acetylene to form phenylacetylene (A_1C_2H) [21]:



The subsequent reaction of phenylacetylene and 1,2-diethynylbenzene (A_1C_2H)₂ results in the formation of naphthalene (A_2) at HAB less than 6 mm via H-addition- C_2H_2 -addition mechanism.



Consequently, phenanthrene (A_3) and pyrene (A_4) are produced via H-addition of A_3-1 , A_4-1 radicals and C_2H_2 addition of A_3-4 radicals.



Due to the large exothermic reactions involved, reaction (R444) is irreversible [21]. Additional route to phenanthrene involves: $P_2 - 1 + C_2H_2 \rightleftharpoons A_3 + H$ (R459), which eventually leads to PAH condensation on the particle surface and mass growth. Therefore it is

clear that the reaction pathways to the larger ring aromatics are very much dependant on the initial production of benzene which accounts for the similarity in trends.

7.5 Sensitivity Analysis

Due to major uncertainties involving premixed flames impinging near the burner plate, it is difficult to estimate the correct flame temperatures. The reduced temperature profiles can have a profound effect on the species and aromatics profiles. The temperature differences between adiabatic and maximum temperatures for Flame Tests 1 to 4 can range from 280 K to over 435 K. To determine the minimum errors associated with reduced temperatures in terms of species concentrations, the lower end of the spectrum of 280 K is only considered. Increasing the main bulk of the temperature profile from HAB 3 to 19 mm of Flame Test 4 (\varnothing at 2.22) by 280 K to near adiabatic temperatures, a sensitivity analysis can be carried out.

7.5.1 Minor Species Comparisons

Figure 60 compares the minor species profiles using the original and augmented temperature profiles as starting estimates. It is observed that there is no change in the species' profiles from HAB 0 to 3 mm as both temperature profiles in this region remains unchanged. It is typical that the radicals exhibit an instantaneous increase before experiencing the same level of decline as well. Clearly from these profiles, the influence of an increased temperature profile results in higher peak concentrations for all species by a factor of two to three. Surprisingly, the modification of temperature does not affect the concentration of vinyl (C_2H_3) radicals.

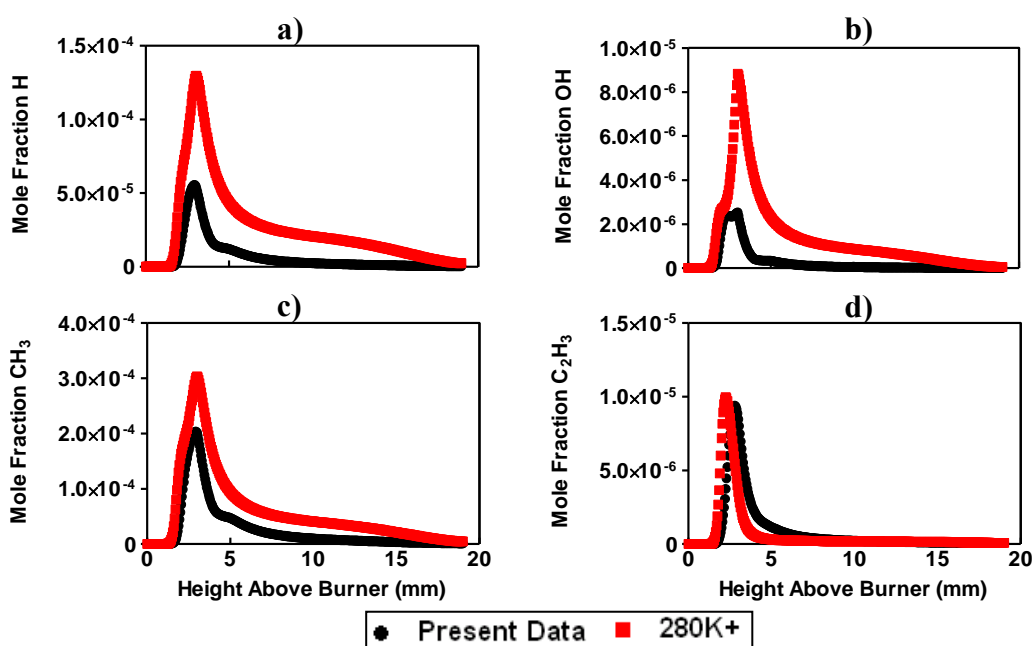


Figure 60 Effect of reduced temperature on minor species profiles at $\varnothing = 2.22$ as a function of HAB

Changes in the temperature profile may tend to affect soot development. Comparison to their work at C/O at 0.78 [2], their predicted H concentrations exhibit comparable curvature patterns from HAB 0 to 10 mm. Despite similarity, there is a difference in peak concentrations by a factor of 18 times between present study and their work. This is attributed to their high unburnt velocities which concur to higher temperatures. Moreover, the low concentrations of the vinyl radicals as observed in Figure 60 (d), combined with low H radicals, may result in a decrease in acetylene production via reaction (R151); essential for soot surface growth [3, 20, 160]

At higher temperatures, the peak concentration for OH mole fraction increases by a factor of three and above. This increase in OH radicals near burner surface is postulated to contain a higher amount of oxidising strength for soot removal [54]. This may cause soot particle size to decrease which indirectly affects soot volume fraction profiles. The increase in OH radicals favour the forward reaction rates of (R113) and (R161) which may account for the same increase observed in Figure 60 (a) and (c).

7.5.2 Acetylene Comparison

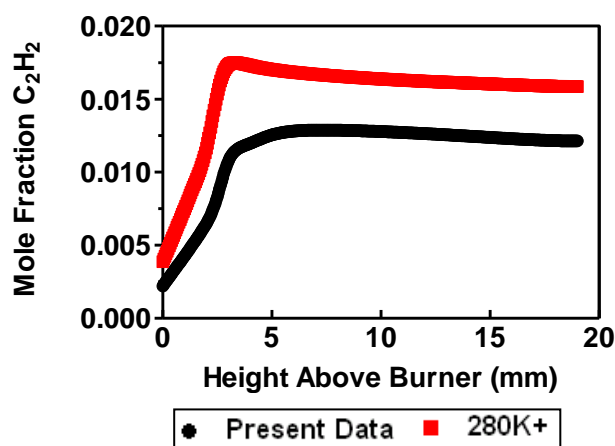
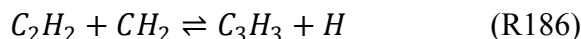


Figure 61 Effect of reduced temperature on acetylene at $\phi = 2.22$ as a function of HAB

It is established that acetylene is vital to the planar growth of PAHs via H-abstraction- C_2H_2 -addition mechanism [24]. Figure 61 reflects the impact of altering the temperatures in the simulation of acetylene growth species. It is apparent that acetylene profiles are under-predicted from HAB 5mm onwards by an order of magnitude. Despite the difference, the behaviours of both profiles still exhibit the same levelling effect after 5 mm of gradual production. Increasing 280 K to the main temperature bulk promotes the formation of PAHs in the main reaction zone. The increased concentrations of hydrogen and vinyl radicals in Figure 60 seem to suggest the reaction sequences of (R136) and (R151) to produce acetylene.

This increase in acetylene eventually leads to the formation of resonantly-stabilised propargyl radicals via [21]:



This reaction step subsequently contributes to the formation of the 1st PAH through reaction (R227). The formation of phenylacetylene (A_1C_2H) via reaction (R369) is also expected to grow as well. This continual growth even eventually extends to the formation of pyrene (A_4). Therefore changes in thermodynamics can significantly alter the planar growth of PAH-addition species.

7.5.3 Aromatics Comparisons

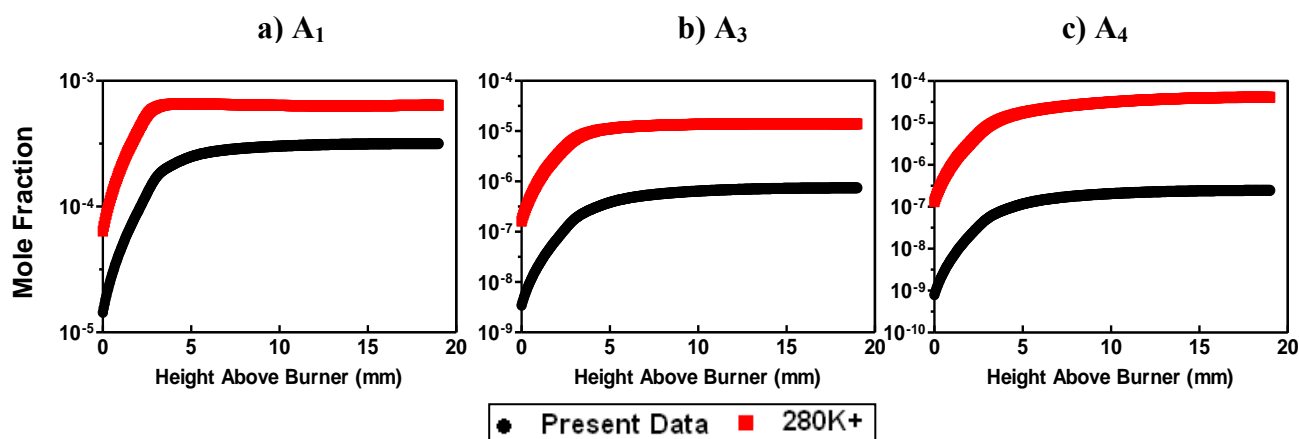


Figure 62 Effect of reduced temperature on aromatics growth at $\phi = 2.22$ as a function of HAB

By changing the main bulk of the temperature profile, only magnitude changes to the aromatics profiles can be observed in Figure 62. It is clear that there is an increasing factor difference between present data and 280 K temperature profiles for benzene (A_1), phenanthrene (A_3) and pyrene (A_4), ranging from by a factor of two for benzene to over 166 times for pyrene. The factor increase for benzene can be attributed to other associated reactions present in the ABF model which defers alternate routes to benzene formation; One such reaction is $n - C_4H_5 + C_2H_2 \rightleftharpoons A_1 + H$ (R290) at 700 K [21]. The increased benzene formation extends to the formation of naphthalene and subsequently phenanthrene via reactions (R438 and R439). The formation of pyrene is achieved through C_2H_2 -addition to the 4-phenanthryl (A_3-4) radical via reaction (R444). For all three profiles, they all exhibit the gradual increase followed by a levelling-off, similar to that of acetylene in Figure 61.

7.6 Summary

Numerical predictions of minor and major chemical species in laminar premixed sooting ethylene flames were reported. The formation and development of the first PAHs into larger ring aromatics such as pyrene was also looked at. Flame simulations were performed using CHEMKIN[®] software as the main operating platform. Other complementary computations include PREMIX flame code using temperatures measured from thermocouples (Chapter 5) as starting estimates and a recently updated reaction mechanism from Appel-Bockhorn-Frenklach (ABF) [19] which extended to the formation and growth of PAHs in laminar premixed C₂ hydrocarbon flames. Among the 100 chemical species involved in the ABF model, only 19 of them were of importance pertaining only to their elementary reactions and contributions to PAH development. Observations into their behaviours revealed the following:

- 1) The peak heights of all minor species increasingly deviated from burner surface with a narrower width as a function of soot propensity.
- 2) It had been established that ethylene fuel was removed by H-abstraction reactions and thermal decomposition. A comparison between acetylene species (C₂H₂) and experimental soot volume fraction profiles seemed to be in differing agreement. This was attributed to the reduced temperature profiles as starting estimates and the inability of CHEMKIN[®] to consider the presence of an overtop burner plate.
- 3) Computational results revealed that benzene (A₁) concentrations were well-predicted within the main reaction zone via propargyl recombination reaction, (R227), in comparison to propargyl (C₃H₃) species. The mass growth of PAHs up to pyrene was well-described via H-addition and C₂H₂-addition.
- 4) A sensitivity analysis was conducted at $\Phi = 2.22$ to examine the importance of thermodynamics on the species' concentrations. It was shown that the minor species exhibited an instantaneous increase and decline within HAB 5 mm and observed temperature differences by a factor of two to three. However, it was worthy to note that temperature does not have much effect on vinyl (C₂H₃) radicals. Acetylene (C₂H₂) and benzene (A₁) were within agreement of each other but a huge difference was observed for pyrene (A₄) profile.

8 CONCLUSION OVERVIEW

The motivations behind this research were the collective elements of soot measurements and species modelling in laminar premixed flat flames. A database of these elements is proposed to be embedded into Virtual Combustion Laboratory (VCL) – a user-friendly interface that surfaces as teaching tool for students and combustion researchers alike. This research focused on the soot concentrations, structures and chemical species modelling in laminar premixed ethylene/air flames at atmospheric pressure using a commercialised McKenna flat flame burner. The flame test conditions involved were from ϕ at 1.82 to 3.80, indicative of slight to heavy soot conditions. A detailed chemical kinetic model describing the pyrolysis and oxidation of ethylene, benzene formation and PAH mass growth was employed for CHEMKIN[®] simulation. In addition, experimental temperatures from thermocouples were used as starting estimates. An overview into the respective chapters of this study is as follows:

- 1) Present measurements of soot volume fractions for both LII and LE were in close agreement for lean conditions but at fuel-rich conditions, LII underestimated LE by a factor of three. This was attributed to the soot particles under detection and soot distribution. It was determined that soot distribution remained relatively uniform in the range ϕ at 1.82 to 2.22 whereas the observed annular distributions in fuel-rich conditions were attributed to ambient air mixing due to low nitrogen shroud. Variable changes to the refractive index of soot, m resulted in potential errors between 3 to 11 % for soot volume fractions.
- 2) TEM images from thermophoretic sampling revealed a noticeably increase in soot particle size distribution and reduction in aggregate number concentration after inception in accordance with Dobbins and Megaridis [16] for all flame test conditions. The largest particle primary diameter was measured to be 56nm whereas the smallest was measured to be 18 nm for ϕ at 3.80. However, no obvious trends could be determined. It was argued that the leeward side of the agglomerates at higher HABs may cause differential values in K_{ext} [4, 5, 73] which clearly inhibited the use of a constant refractive index throughout the flame.
- 3) The adverse effect of low velocity premixed mixture and low nitrogen shroud not only resulted in changes to the magnitude and shape of the temperature profiles via burner plate heat transfer [49] but also caused non-uniformity along the radial axis. Ceramic

coating on the thermocouple wires was found to decrease temperatures by 205 K. Other uncertainties involved estimation of correlations by air properties at film temperature.

- 4) The ABF gas-phase mechanism [19] gave in-depth predictions of the minor, intermediate and aromatic species using PREMIX [154]. The model was able to effectively simulate the chemical reactions associated with ethylene oxidation at atmospheric conditions regardless of stoichiometry and HABs. Computational results revealed that there was little correlation between acetylene and soot volume fraction. However, benzene concentrations were reasonably well-predicted via propargyl recombination pathway ($C_3H_3 + C_3H_3 \rightarrow C_6H_6$) which agreed with past works [20, 22]. The mass growth of PAHs into larger components was well-structured via H-addition C_2H_2 -addition mechanism.

- 5) A temperature differential analysis on minor species showed an instantaneous increase and decline at less than HAB 5 mm with two-times difference to present data. Particularly, predictions of mole fraction H exhibited similar curve patterns to that of Xu and co-workers [2] but with a magnitude difference of 18 times. Acetylene (C_2H_2) and benzene (A_1) were within agreement of each other except for pyrene.

Finally, this study has fully addressed the formation of soot in laminar premixed flames between experimental measurements and theoretical computations. However, there are still some elements in this study that can be further improved or expanded to include other soot detection techniques.

9 POTENTIAL WORK RECOMMENDATIONS

This research not only focused on the soot concentrations by non-intrusive laser diagnostics but also looked at chemical species by theoretical computations using a single reaction model. Several issues identified in this study that needs further work on are:

- The effect of PAHs on soot volume fractions remained unknown therefore utilising an infra-red continuous wave laser at 1064 nm would resolve differences in present results by LE and LII in the visible region.
- Other suitable soot detection techniques could be employed for laminar flames such as gravimetric sampling. This technique could either be used to calibrate LII signals [77] or be calibrated by LE [43].
- Temperatures by other non-intrusive techniques such as CARS and TLAF should be performed for comparison to those by thermocouples. Multi-line emission offers better accuracy than the latter in less than 50 K uncertainty. This would derive a closer depiction of the flame structure and species computation.
- Gas sampling for major chemical species should be employed for comparison to similar species as simulated using the ABF gas-phase mechanism.

10 NOMENCLATURE

10.1 Symbols

A_{bead}	Bead Area	m^2
A_{burner}	Burner Area	m^2
d_{bead}	Bead Diameter	m
d_{burner}	Burner Diameter	m
d_p	Mean Particle Diameter	Nm
f_v	Soot Volume Fraction	ppm
h_c	Heat Transfer Coefficient	$\text{W}/\text{m}^2 \cdot \text{K}$
k	Imaginary Part of Refractive Index	-
K_{abs}	Absorption Coefficient	-
K_e	Dimensionless Extinction Coefficient	-
K_{ext}	Extinction Coefficient	mm^{-1}
K_a	Dimensionless Absorption Coefficient	-
\bar{I}_O	Time-Averaged Incident Intensity	V
\bar{I}_T	Time-Averaged Transmitted Intensity	V
L	Laser Path	mm
m	Refractive Index of Soot	-
n	Real Part of Refractive Index	-
Nu	Nusselt Number	-
Pr	Prandtl Number	-
q_{rad}	Radiative Heat Transfer	W
Re	Reynolds number	-
T_{gas}	Gas Temperature	K
T_{∞}	Ambient Temperature	K
T_{tc}	Thermocouple Temperature	K
U_o	Burner Exit Velocity	m/s

10.2 Greek Symbols

ϕ	Equivalence Ratio	-
λ	Wavelength	nm
k_{air}	Thermal Conductivity of Air	W/m ² .K
ρ_{air}	Density of Air	kg/m ²
α_{air}	Thermal Diffusivity of Air	m ² /s
ν_{air}	Kinematic Viscosity of Air	m ² /s
ε	Emissivity	-
σ	Stefan-Boltzmann Constant	W/m ² .K ⁴

10.3 Acronyms

ABF	Appel–Bockhorn–Frenklach Model
HAB	Height Above Burner
HACA	H-Abstraction-C ₂ H ₂ -Addition
LE	Laser Extinction
LII	Laser-Induced Incandescence
PAHs	Polycyclic Aromatic Hydrocarbons
TEM	Transmission Electron Microscopy
TIFF	Tagged Image Format File
WF	Wang & Frenklach Model

10.4 Chemical Species Acronyms

OH	Hydroxyl	A₁	Benzene
CH₃	Methyl	A₁⁻	Phenyl
CH₄	Methane	A₂	Naphthalene
C₂H₂	Acetylene	A₃	Phenanthrene
C₂H₃	Vinyl	A₃ - 1, A₃ - 4	Phenanthryl
C₂H₄	Ethylene	A₄	Pyrene
C₂H₆	Ethane	A₁C₂H	Phenylacetylene
C₃H₃	Propargyl	A₁C₂H)₂	1,2- diethynylbenzene
C₄H₂	Diacetylene	A₁C₂H₃	Styrene
C₄H₄	Vinylacetylene	P₂	Biphenyl

11 BIBLIOGRAPHY

- [1] H. G. Wagner, "Soot formation in combustion," *Symposium (International) on Combustion*, vol. 17, pp. 3-19, 1979.
- [2] F. Xu, P. B. Sunderland, and G. M. Faeth, "Soot formation in laminar premixed ethylene/air flames at atmospheric pressure," vol. 108, pp. 471-493, 1997.
- [3] S. J. Harris and A. M. Weiner, "Surface Growth of Soot Particles in Premixed Ethylene Air Flames," *Combustion Science and Technology*, vol. 31, pp. 155-167, 1983.
- [4] G. W. Mulholland and M. Y. Choi, "Measurement of the mass specific extinction coefficient for acetylene and ethene smoke using the large agglomerate optics facility," *Symposium (International) on Combustion*, vol. 27, pp. 1515-1522, 1998.
- [5] J. Y. Zhu, M. Y. Choi, G. W. Mulholland, S. L. Manzello, L. A. Gritzko, and J. Suo-Antila, "Measurement of visible and near-IR optical properties of soot produced from laminar flames," *Proceedings of the Combustion Institute*, vol. 29, pp. 2367-2374, 2003.
- [6] J. Appel, B. Jungfleisch, M. Marquardt, R. Suntz, and H. Bockhorn, "Assessment of soot volume fractions from laser-induced incandescence by comparison with extinction measurements in laminar, premixed, flat flames," *Symposium (International) on Combustion*, vol. 26, pp. 2387-2395, 1996.
- [7] B. Axelsson, R. Collin, and P.-E. Bengtsson, "Laser-Induced Incandescence for Soot Particle Size Measurements in Premixed Flat Flames," *Appl. Opt.*, vol. 39, pp. 3683-3690, 2000.
- [8] B. Axelsson, R. Collin, and P. E. Bengtsson, "Laser-induced incandescence for soot particle size and volume fraction measurements using on-line extinction calibration," *Applied Physics B-Lasers and Optics*, vol. 72, pp. 367-372, Feb 2001.
- [9] P. E. Bengtsson and M. Alden, "Soot-Visualization Strategies Using Laser Techniques - Laser-Induced Fluorescence in C₂ from Laser-Vaporized Soot and Laser-Induced Soot Incandescence," *Applied Physics B-Lasers and Optics*, vol. 60, pp. 51-59, Jan 1995.

-
- [10] P. E. Bengtsson and M. Aldén, "Application of a pulsed laser for soot measurements in premixed flames," *Applied Physics B: Lasers and Optics*, vol. 48, pp. 155-164, 1989.
- [11] R. L. Vander Wal and K. J. Weiland, "Laser-induced incandescence: Development and characterization towards a measurement of soot-volume fraction," *Applied Physics B: Lasers and Optics*, vol. 59, pp. 445-452, 1994.
- [12] B. Quay, T. W. Lee, T. Ni, and R. J. Santoro, "Spatially resolved measurements of soot volume fraction using laser-induced incandescence," *Combustion and Flame*, vol. 97, pp. 384-392, 1994.
- [13] C. R. Shaddix and K. C. Smyth, "Laser-induced incandescence measurements of soot production in steady and flickering methane, propane, and ethylene diffusion flames," *Combustion and Flame*, vol. 107, pp. 418-452, 1996.
- [14] S. Will, S. Schraml, and A. Leipertz, "2-Dimensional Soot-Particle Sizing by Time-Resolved Laser-Induced Incandescence," *Optics Letters*, vol. 20, pp. 2342-2344, Nov 15 1995.
- [15] L. A. Melton, "Soot diagnostics based on laser heating," *Appl. Opt.*, vol. 23, pp. 2201-2208, 1984.
- [16] R. A. Dobbins and C. M. Megaridis, "Morphology of Flame-Generated Soot as Determined by Thermophoretic Sampling," *Langmuir*, vol. 3, pp. 254-259, Mar-Apr 1987.
- [17] Ü. Ö. Köylü, C. S. McEnally, D. E. Rosner, and L. D. Pfefferle, "Simultaneous measurements of soot volume fraction and particle size / microstructure in flames using a thermophoretic sampling technique," *Combustion and Flame*, vol. 110, pp. 494-507, 1997.
- [18] A. D. Eisner and D. E. Rosner, "Experimental studies of soot particle thermophoresis in nonisothermal combustion gases using thermocouple response techniques," *Combustion and Flame*, vol. 61, pp. 153-166, 1985.
- [19] J. Appel, H. Bockhorn, and M. Frenklach, "Kinetic modeling of soot formation with detailed chemistry and physics: laminar premixed flames of C2 hydrocarbons," *Combustion and Flame*, vol. 121, pp. 122-136, 2000.
-

-
- [20] J. A. Miller and C. F. Melius, "Kinetic and thermodynamic issues in the formation of aromatic compounds in flames of aliphatic fuels," *Combustion and Flame*, vol. 91, pp. 21-39, 1992.
- [21] H. Wang and M. Frenklach, "A detailed kinetic modeling study of aromatics formation in laminar premixed acetylene and ethylene flames," vol. 110, pp. 173-221, 1997.
- [22] M. J. Castaldi, N. M. Marinov, C. F. Melius, J. Huang, S. M. Senkan, W. J. Pitt, and C. K. Westbrook, "Experimental and modeling investigation of aromatic and polycyclic aromatic hydrocarbon formation in a premixed ethylene flame," *Symposium (International) on Combustion*, vol. 26, pp. 693-702, 1996.
- [23] T. G. Benish, A. L. Lafeur, K. Taghiadeh, and J. B. Howard, "C₂H₂ and PAH as soot growth reactants in premixed C₂H₄-air flames," *Symposium (International) on Combustion*, vol. 26, pp. 2319-2326, 1996.
- [24] M. Frenklach and H. Wang, "Detailed modeling of soot particle nucleation and growth," *Symposium (International) on Combustion*, vol. 23, pp. 1559-1566, 1991.
- [25] N. M. Marinov, W. J. Pitz, C. K. Westbrook, M. J. Castaldi, and S. M. Senkan, "Modeling of aromatic and polycyclic aromatic hydrocarbon formation in premixed methane and ethane flames," *Combustion Science and Technology*, vol. 116, pp. 211-287, 1996.
- [26] A. D'Anna and A. Violi, "Detailed modeling of the molecular growth process in aromatic and aliphatic premixed flames," *Energy & Fuels*, vol. 19, pp. 79-86, Jan-Feb 2005.
- [27] H. F. Calcote, "Mechanisms of soot nucleation in flames--A critical review," *Combustion and Flame*, vol. 42, pp. 215-242, 1981.
- [28] B. S. Haynes and H. G. Wagner, "Soot Formation," *Progress in Energy and Combustion Science*, vol. 7, pp. 229-273, 1981.
- [29] University of California Berkeley, "Appel-Bockhorn-Frenklach gas-phase combustion mechanism ", 2008.
- [30] CHEMKIN, "Reaction Design," 2007.
-

-
- [31] Earth Policy Institute, "Carbon Dioxide Emissions Accelerating Rapidly," 2009.
- [32] R. M. Fristrom and A. A. Westenberg, *Flame structure*. USA: McGraw-Hill, Inc., 1965.
- [33] J. Warnatz, "Flame velocity and structure of laminar hydrocarbon-air flames," *Progress in Aeronautics & Astronauts*, vol. 76, pp. 501 - 521, 1979.
- [34] HOLTHUIS & ASSOCIATES, "Flat Flame Burner ", 2007.
- [35] R. J. Cattolica, "OH radical nonequilibrium in methane---air flat flames," *Combustion and Flame*, vol. 44, pp. 43-59, 1982.
- [36] S. Prucker, W. Meier, and W. Stricker, "A Flat Flame Burner as Calibration Source for Combustion Research - Temperatures and Species Concentrations of Premixed H-2/Air Flames," *Review of Scientific Instruments*, vol. 65, pp. 2908-2911, Sep 1994.
- [37] P. Weigand, R. Lückcrath, and W. Meier, "Documentation of flat premixed laminar CH4/air standard flames: Temperatures and species Concentrations," 2007.
- [38] G. Sutton, A. Levick, G. Edwards, and D. Greenhalgh, "A combustion temperature and species standard for the calibration of laser diagnostic techniques," *Combustion and Flame*, vol. 147, pp. 39-48, 2006.
- [39] E. W. Kaiser, W. G. Rothschild, and G. A. Lavoie, "Effect of Fuel-Air Equivalence Ratio and Temperature on the Structure of Laminar Propane-Air Flames," *Combustion Science and Technology*, vol. 33, pp. 123-134, 1983.
- [40] F. Migliorini, S. De Iuliis, F. Cignoli, and G. Zizak, "How "flat" is the rich premixed flame produced by your McKenna burner?," *Combustion and Flame*, vol. 153, pp. 384-393, 2008.
- [41] A. D'Alessio, A. Di Lorenzo, F. Beretta, and C. Venitozzi, "Optical and chemical investigations on fuel-rich methane-oxygen premixed flames at atmospheric pressure," *Symposium (International) on Combustion*, vol. 14, pp. 941-953, 1973.
- [42] B. S. Haynes, H. Jander, and H. G. Wagner, "Optical Studies of Soot-Formation Processes in Premixed Flames," *Berichte Der Bunsen-Gesellschaft-Physical Chemistry Chemical Physics*, vol. 84, pp. 585-592, 1980.
-

-
- [43] M. Y. Choi, G. W. Mulholland, A. Hamins, and T. Kashiwagi, "Comparisons of the soot volume fraction using gravimetric and light extinction techniques," *Combustion and Flame*, vol. 102, pp. 161-169, 1995.
- [44] S. J. Harris, A. M. Weiner, and C. Cleveland Ashcraft, "Soot particle inception kinetics in a premixed ethylene flame," *Combustion and Flame*, vol. 64, pp. 65-81, 1986.
- [45] S. R. Turns, *An introduction to combustion: concepts and applications*, 2nd ed. Singapore: McGraw-Hill Book Co, 2000.
- [46] J. C. Street and A. Thomas, "Carbon formation in premixed flames," *Fuel*, vol. 34, pp. 4 - 36, 1955.
- [47] H. Richter and J. B. Howard, "Formation of polycyclic aromatic hydrocarbons and their growth to soot - a review of chemical reaction pathways," *Progress in Energy and Combustion Science*, vol. 26, pp. 565-608, 2000.
- [48] J. Xi and B. J. Zhong, "Soot in diesel combustion systems," *Chemical Engineering & Technology*, vol. 29, pp. 665-673, Jun 2006.
- [49] L. P. H. Degoey, A. Vanmaaren, and R. M. Quax, "Stabilization of Adiabatic Premixed Laminar Flames on a Flat Flame Burner," *Combustion Science and Technology*, vol. 92, pp. 201-207, 1993.
- [50] J.-L. Delfau, J. Biet, M. Idir, L. Pillier, and C. Vovelle, "Experimental and numerical study of premixed, lean ethylene flames," *Proceedings of the Combustion Institute*, vol. 31, pp. 357-365, 2007.
- [51] Air Liquide, "Pure Gases MSDS," 2008.
- [52] C. Morley, "GASEQ version 0.79." vol. 2008.
- [53] ABB Automation, "Specification: Variable Area Flowmeters Purgemaster Series 10A6130LK," 2009.
- [54] R. Millikan, "Non-equilibrium soot formation in premixed flames," *Journal of Physical Chemistry*, vol. 66, pp. 2719-2719, 1962.

-
- [55] K. G. Neoh, J. B. Howard, and A. F. Sarofim, "Effect of oxidation on the physical structure of soot," *Symposium (International) on Combustion*, vol. 20, pp. 951-957, 1985.
- [56] J. H. Kent and S. J. Bastin, "Parametric effects on sooting in turbulent acetylene diffusion flames," *Combustion and Flame*, vol. 56, pp. 29-42, 1984.
- [57] B. Lacaze and M. Chabert, "Power spectra for laser-extinction measurements," *Optics Express*, vol. 14, pp. 6011-6019, Jun 26 2006.
- [58] A. D'Alessio, A. Di Lorenzo, A. F. Sarofim, F. Beretta, S. Masi, and C. Venitozzi, "Soot formation in methane-oxygen flames," *Symposium (International) on Combustion*, vol. 15, pp. 1427-1438, 1975.
- [59] E. J. Santoro and C. R. Shaddix, "Laser-induced incandescence," in *Applied Combustion Diagnostics*, K. Kohse-Höinghaus and J. B. Jeffries, Eds. USA: Taylor & Francis, 2002, pp. 252 - 286.
- [60] W. H. Dalzell and A. F. Sarofim, "Optical constants of soot and their application to heat-flux calculations," *Journal of Heat Transfer*, vol. 91, pp. 100 - 104, 1969.
- [61] S. C. Lee and C. L. Tien, "Optical constants of soot in hydrocarbon flames," *Symposium (International) on Combustion*, vol. 18, pp. 1159-1166, 1981.
- [62] T. T. Charalampopoulos and J. D. Felske, "Refractive-Indexes of Soot Particles Deduced from Insitu Laser-Light Scattering Measurements," *Combustion and Flame*, vol. 68, pp. 283-294, Jun 1987.
- [63] Z. Q. Zhou, T. U. Ahmed, and M. Y. Choi, "Measurement of dimensionless soot extinction constant using a gravimetric sampling technique," *Experimental Thermal and Fluid Science*, vol. 18, pp. 27-32, Sep 1998.
- [64] S. Chippett and W. A. Gray, "The size and optical properties of soot particles," *Combustion and Flame*, vol. 31, pp. 149-159, 1978.
- [65] Z. G. Habib and P. Vervisch, "On the Refractive-Index of Soot at Flame Temperature," *Combustion Science and Technology*, vol. 59, pp. 261-274, 1988.

-
- [66] T. T. Charalampopoulos, H. Chang, and B. Stagg, "The Effects of Temperature and Composition on the Complex Refractive-Index of Flame Soot," *Fuel*, vol. 68, pp. 1173-1179, Sep 1989.
- [67] Thorlabs Inc, *HRP 350 HeNe - Laser Systems*, 2005.
- [68] Stanford Research Systems, *Model SR 540 Optical Chopper*, 1997.
- [69] M. Bass, E. W. Stryland, D. R. Williams, and W. L. Wolfe, "Fundamentals, Techniques and Design," in *Handbook of optics*. vol. 1 USA: McGraw-Hill, Inc, 1995.
- [70] ADInstruments, "PowerLab Data Acquisition Systems," 2008.
- [71] S. J. Harris and A. M. Weiner, "Determination of the Rate-Constant for Soot Surface Growth," *Combustion Science and Technology*, vol. 32, pp. 267-275, 1983.
- [72] J. S. Wu, S. S. Krishnan, and G. M. Faeth, "Refractive indices at visible wavelengths of soot emitted from buoyant turbulent diffusion flames," *Journal of Heat Transfer-Transactions of the Asme*, vol. 119, pp. 230-237, May 1997.
- [73] G. W. Mulholland and R. D. Mountain, "Coupled dipole calculation of extinction coefficient and polarization ratio for smoke agglomerates," *Combustion and Flame*, vol. 119, pp. 56-68, 1999.
- [74] H. Chang and T. T. Charalampopoulos, "Determination of the Wavelength Dependence of Refractive-Indexes of Flame Soot," *Proceedings of the Royal Society of London Series a-Mathematical Physical and Engineering Sciences*, vol. 430, pp. 577-591, Sep 8 1990.
- [75] A. C. Eckbreth, "Effects of laser-modulated particulate incandescence on Raman scattering diagnostics," *Journal of Applied Physics*, vol. 48, pp. 4473-4479, 1977.
- [76] M. Y. Choi and K. A. Jensen, "Calibration and correction of laser-induced incandescence for soot volume fraction measurements," *Combustion and Flame*, vol. 112, pp. 485-491, 1998.
- [77] R. L. Vander Wal, Z. Zhou, and M. Y. Choi, "Laser-induced incandescence calibration via gravimetric sampling," *Combustion and Flame*, vol. 105, pp. 462-470, 1996.
- [78] R. L. Vander Wal and M. Y. Choi, "Pulsed laser heating of soot: morphological changes," *Carbon*, vol. 37, pp. 231-239, 1999.
-

-
- [79] P. E. Bengtsson and M. Alden, "Soot Particle Measurements in Premixed Ethylene Flames Using a Pulsed Laser Method," *Journal of Aerosol Science*, vol. 19, pp. 959-962, 1988.
- [80] B. Mewes and J. M. Seitzman, "Soot volume fraction and particle size measurements with laser-induced incandescence," *Appl. Opt.*, vol. 36, pp. 709-717, 1997.
- [81] N. H. Qamar, G. J. Nathan, Z. T. Alwahabi, and K. D. King, "The effect of global mixing on soot volume fraction: measurements in simple jet, precessing jet, and bluff body flames," *Proceedings of the Combustion Institute*, vol. 30, pp. 1493-1500, 2005.
- [82] P.-E. Bengtsson and M. Aldén, "Optical investigation of laser-produced C₂ in premixed sooty ethylene flames," *Combustion and Flame*, vol. 80, pp. 322-328, 1990.
- [83] R. L. Vander Wal, "Laser-induced incandescence: detection issues," *Appl. Opt.*, vol. 35, pp. 6548-6559, 1996.
- [84] S. De Iuliis, F. Migliorini, F. Cignoli, and G. Zizak, "Peak soot temperature in laser-induced incandescence measurements," *Applied Physics B-Lasers and Optics*, vol. 83, pp. 397-402, Jun 2006.
- [85] T. Ni, J. A. Pinson, S. Gupta, and R. J. Santoro, "Two-dimensional imaging of soot volume fraction by the use of laser-induced incandescence," *Appl. Opt.*, vol. 34, pp. 7083-7091, 1995.
- [86] R. L. Vander Wal, M. Y. Choi, and K.-o. Lee, "The effects of rapid heating of soot: Implications when using laser-induced incandescence for soot diagnostics," *Combustion and Flame*, vol. 102, pp. 200-204, 1995.
- [87] R. L. Vander Wal, T. M. Ticich, and A. B. Stephens, "Optical and microscopy investigations of soot structure alterations by laser-induced incandescence," *Applied Physics B-Lasers and Optics*, vol. 67, pp. 115-123, Jul 1998.
- [88] C. J. Dasch, "Continuous-wave probe laser investigation of laser vaporization of small soot particles in a flame," *Appl. Opt.*, vol. 23, pp. 2209-2215, 1984.
- [89] N. P. Tait and D. A. Greenhalgh, "2D laser induced fluorescence imaging of parent fuel fraction in nonpremixed combustion," *Symposium (International) on Combustion*, vol. 24, pp. 1621-1628, 1992.
-

-
- [90] Quantel, *Model Brilliant B Nd:YAG Twins*. France, 2008.
- [91] PI/Acton, "PI-Max ICCD Spectroscopy Cameras," 2008.
- [92] Gentec-eo, "Laser Power Meter & Laser Energy Meter," 2008.
- [93] PI/Acton, "WinView," 2008.
- [94] C. Law, "A Compilation of Experimental Data on Laminar Burning Velocities," in *Reduced Kinetic Mechanisms for Applications in Combustion Systems*, 1993, pp. 15-26.
- [95] B. Öktem, M. P. Tolocka, B. Zhao, H. Wang, and M. V. Johnston, "Chemical species associated with the early stage of soot growth in a laminar premixed ethylene-oxygen-argon flame," *Combustion and Flame*, vol. 142, pp. 364-373, 2005.
- [96] R. J. Santoro, H. G. Semerjian, and R. A. Dobbins, "Soot particle measurements in diffusion flames," *Combustion and Flame*, vol. 51, pp. 203-218, 1983.
- [97] R. M. Fristrom, "The structure of laminar flames," *Symposium (International) on Combustion*, vol. 6, pp. 96-110, 1957.
- [98] T. Drier and P. Ewart, "Coherent Techniques for Measurements with Intermediate Concentrations," in *Applied Combustion Diagnostics*, K. Kohse-Höinghaus and J. B. Jeffries, Eds. USA: Taylor & Francis, 2002, pp. 69-97.
- [99] P. A. Kinze, *Thermocouple Temperature Measurement*. Canada: John Wiley & Sons, Inc., 1973.
- [100] T. J. Quinn, *Temperature*. New York: Academic Press Inc., 1983.
- [101] Pico Technology Limited, "Thermocouple application note," 2009.
- [102] J. D. Lenk, *ABC's of thermocouples*. England: W.Foulsham & Co. Ltd., 1968.
- [103] R. Friedman, "Measurement of the temperature profile in a laminar flame," *Symposium (International) on Combustion*, vol. 4, pp. 259-263, 1953.
- [104] W. E. Kaskan, "The dependence of flame temperature on mass burning velocity," *Symposium (International) on Combustion*, vol. 6, pp. 134-143, 1957.

-
- [105] R. Friedman and E. Burke, "Measurement of Temperature Distribution in a Low-Pressure Flat Flame," *The Journal of Chemical Physics*, vol. 22, pp. 824-830, 1954.
- [106] J. H. Kent, "A noncatalytic coating for platinum-rhodium thermocouples," *Combustion and Flame*, vol. 14, pp. 279-281, 1970.
- [107] D. Bradley and K. J. Matthews, "Measurement of high temperatures with fine wire thermocouples," *Journal of Mechanical Engineering Science*, vol. 10, pp. 299-305, 1968.
- [108] P. Struk, D. Dietrich, R. Valentine, and I. Feier, "Comparisons of gas-phase temperature measurements in a flame using thin-filament pyrometry and thermocouples," in *41st Aerospace Sciences Meeting Exhibit*, 2003.
- [109] S. J. Harris, A. M. Weiner, and R. J. Blint, "Formation of small aromatic molecules in a sooting ethylene flame," *Combustion and Flame*, vol. 72, pp. 91-109, 1988.
- [110] J. Biet, J.-L. Delfau, A. Seydi, and C. Vovelle, "Experimental and modeling study of lean premixed atmospheric-pressure propane/O₂/N₂ flames," *Combustion and Flame*, vol. 142, pp. 197-209, 2005.
- [111] A. J. Mortlock, "Error in temperature measurement due to the interdiffusion at the hot junction of a thermocouple," *Journal of Scientific Instruments*, vol. 35, pp. 283-284, 1958.
- [112] H. Kramers, "Heat transfer from spheres to flowing media," *Physica*, vol. 12, pp. 61-80, 1946.
- [113] J. P. Holman, *Heat Transfer*, 9th ed. New York: McGraw-Hill Companies, Inc, 2002.
- [114] A. D. Abid, N. Heinz, E. D. Tolmachoff, D. J. Phares, C. S. Campbell, and H. Wang, "On evolution of particle size distribution functions of incipient soot in premixed ethylene-oxygen-argon flames," *Combustion and Flame*, vol. 154, pp. 775-788, 2008.
- [115] S. Brohez, C. Delvosalle, and G. Marlair, "A two-thermocouples probe for radiation corrections of measured temperatures in compartment fires," *Fire Safety Journal*, vol. 39, pp. 399-411, Jul 2004.
- [116] C. K. Law, "Dynamics of stretched flames," *Symposium (International) on Combustion*, vol. 22, pp. 1381-1402, 1989.
-

-
- [117] P.-E. Bengtsson, M. Aldén, S. Kröll, and D. Nilsson, "Vibrational CARS thermometry in sooty flames: Quantitative evaluation of C2 absorption interference," *Combustion and Flame*, vol. 82, pp. 199-210, 1990.
- [118] U. Bonne, K. H. Homann, and H. G. Wagner, "Carbon formation in premixed flames," *Symposium (International) on Combustion*, vol. 10, pp. 503-512, 1965.
- [119] L. Baumgärtner, D. Hesse, H. Jander, and H. G. Wagner, "Rate of soot growth in atmospheric premixed laminar flames," *Symposium (International) on Combustion*, vol. 20, pp. 959-967, 1985.
- [120] S. J. Harris and A. M. Weiner, "Chemical-Kinetics of Soot Particle Growth," *Annual Review of Physical Chemistry*, vol. 36, pp. 31-52, 1985.
- [121] M. Frenklach, "Reaction mechanism of soot formation in flames," *Physical Chemistry Chemical Physics*, vol. 4, pp. 2028-2037, 2002.
- [122] M. Frenklach, D. W. Clary, J. W. C. Gardiner, and S. E. Stein, "Detailed kinetic modeling of soot formation in shock-tube pyrolysis of acetylene," in *Twentieth Symposium (International) on Combustion*, vol. 20, 1985, pp. 887-901.
- [123] S. Stein, "On the High Temperature Chemical Equilibria of Polycyclic Aromatic Hydrocarbons," *The Journal of Physical Chemistry*, vol. 82, pp. 566-571, 1978.
- [124] S. J. Harris and A. M. Weiner, "A picture of soot particle inception," *Symposium (International) on Combustion*, vol. 22, pp. 333-342, 1989.
- [125] M. Frenklach, T. Yuan, and M. K. Ramachandra, "Soot formation in binary hydrocarbon mixtures," *Energy & Fuels*, vol. 2, pp. 462-480, 1988.
- [126] G. Prado, J. Jagoda, K. Neoh, and J. Lahaye, "A study of soot formation in premixed propane/oxygen flames by in-situ optical techniques and sampling probes," *Symposium (International) on Combustion*, vol. 18, pp. 1127-1136, 1981.
- [127] R. Puri, T. F. Richardson, R. J. Santoro, and R. A. Dobbins, "Aerosol Dynamic Processes of Soot Aggregates in a Laminar Ethene Diffusion Flame," *Combustion and Flame*, vol. 92, pp. 320-333, Feb 1993.
-

-
- [128] P. Pandey, B. P. Pundir, and P. K. Panigrahi, "Hydrogen addition to acetylene-air laminar diffusion flames: Studies on soot formation under different flow arrangements," *Combustion and Flame*, vol. 148, pp. 249-262, 2007.
- [129] H. Bockhorn, F. Fetting, G. Wannemacher, and H. W. Wenz, "Optical studies of soot particle growth in hydrocarbon oxygen flames," *Symposium (International) on Combustion*, vol. 19, pp. 1413-1420, 1982.
- [130] C. S. McEnally, Ü. Ö. Köylü, L. D. Pfefferle, and D. E. Rosner, "Soot volume fraction and temperature measurements in laminar nonpremixed flames using thermocouples," *Combustion and Flame*, vol. 109, pp. 701-720, 1997.
- [131] A. Gomez and D. E. Rosner, "Thermophoretic Effects on Particles in Counterflow Laminar Diffusion Flames," *Combustion Science and Technology*, vol. 89, pp. 335-362, 1993.
- [132] P. B. Sunderland, Ü. Ö. Köylü, and G. M. Faeth, "Soot formation in weakly buoyant acetylene-fueled laminar jet diffusion flames burning in air," *Combustion and Flame*, vol. 100, pp. 310-322, 1995.
- [133] C. M. Megaridis and R. A. Dobbins, "Morphological Description of Flame-Generated Materials," *Combustion Science and Technology*, vol. 71, pp. 95-109, 1990.
- [134] L. E. Murr and K. F. Soto, "A TEM study of soot, carbon nanotubes, and related fullerene nanopolyhedra in common fuel-gas combustion sources," *Materials Characterization*, vol. 55, pp. 50-65, Jul 2005.
- [135] C. K. Westbrook, F. L. Dryer, and K. P. Schug, "Numerical modeling of ethylene oxidation in laminar flames," *Combustion and Flame*, vol. 52, pp. 299-313, 1983.
- [136] C. K. Westbrook and F. L. Dryer, "Chemical kinetic modelling of hydrocarbon combustion," *Progress in Energy and Combustion*, vol. 10, pp. 1-57, 1984.
- [137] J. Warnatz, "Hydrocarbon oxidation at high temperatures," *Deutsche Bunsen-Gesellschaft Fur Physikalische Chemie*, vol. 87, pp. 1008 -1022, 1983.
- [138] C. K. Westbrook and F. L. Dryer, "Simplified Reaction-Mechanisms for the Oxidation of Hydrocarbon Fuels in Flames," *Combustion Science and Technology*, vol. 27, pp. 31-43, 1981.
-

-
- [139] V. V. Lissianski, V. M. Zamansky, and W. C. Gardiner Jr, "Combustion Chemistry Modeling," in *Gas-Phase Combustion Chemistry*, W.C. Gardiner Jr, Ed. New York: Springer-Verlag, Inc, 2000.
- [140] C. S. McEnally, L. D. Pfefferle, A. Burak, and K. Kohse-Hoinghaus, "Studies of aromatic hydrocarbon formation mechanisms in flames: Progress towards closing the fuel gap," *Progress in Energy and Combustion Science*, vol. 32, pp. 247-294, 2006.
- [141] L. V. Moskaleva, A. M. Mebel, and M. C. Lin, "The CH₃+C₅H₅ reaction: A potential source of benene at high temperatures," *Symposium (International) on Combustion*, vol. 26, pp. 521-526, 1996.
- [142] C. K. Westbrook, F. L. Dryer, and K. P. Schug, "A comprehensive mechanism for the pyrolysis and oxidation of ethylene," *Symposium (International) on Combustion*, vol. 19, pp. 153-166, 1982.
- [143] S. J. Harris, W. Anita M, R. J. Blint, and J. E. M. Goldsmith, "Concentration profiles in rich and sooting ethylene flames," *Symposium (International) on Combustion*, vol. 21, pp. 1033-1045, 1988.
- [144] J. M. Levy, B. R. Taylor, J. P. Longwell, and A. F. Sarofim, "C₁ and C₂ chemistry in rich mixture, ethylene/air flames," *Symposium (International) on Combustion*, vol. 19, pp. 167-179, 1982.
- [145] T. Tanzawa and W. C. Gardiner Jr, "Thermal decomposition of ethylene," *Combustion and Flame*, vol. 39, pp. 241-253, 1980.
- [146] J. A. Miller, R. E. Mitchell, M. D. Smooke, and R. J. Kee, "Toward a comprehensive chemical kinetic mechanism for the oxidation of acetylene: Comparison of model predictions with results from flame and shock tube experiments," *Symposium (International) on Combustion*, vol. 19, pp. 181-196, 1982.
- [147] R. T. Morrison and R. N. Boyd., *Organic Chemistry*, 6th ed. Englewood Cliffs, New Jersey: Prentice-Hall, Inc, 1992.
- [148] S. E. Stein, J. A. Walker, M. M. Suryan, and A. Fahr, "A new path to benzene in flames," *Symposium (International) on Combustion*, vol. 23, pp. 85-90, 1991.

-
- [149] R. J. Kee, G. Dixon-Lewis, J. Warnatz, M. E. Coltrin, J. A. Miller, and H. K. Moffat, "A Fortran computer code package for the evaluation of gas-phase, multicomponent transport properties," *Sandia National Laboratories Report SAND86-8246B*, 1998.
- [150] GRI-MECH version 3.0, "GRI-MECH Releases," 2007.
- [151] A. A. Konnov, "Detailed reaction mechanism for small hydrocarbons combustion, Release 0.5," 2000.
- [152] R. J. Kee, F. M. Rupley, and J. A. Miller, "Chemkin-II: A Fortran chemical kinetics package for the analysis of gas phase chemical kinetics," *Sandia National Laboratories Report SAND89-8009*, 1989.
- [153] A. D'Anna, A. Violi, and A. D'Alessio, "Modeling the rich combustion of aliphatic hydrocarbons," *Combustion and Flame*, vol. 121, pp. 418-429, May 2000.
- [154] R. J. Kee, J. F. Grear, J. A. Miller, and E. Meeks, "Premix: a Fortran program for modelling steady laminar one-dimensional premixed flames." vol. 2009, 1998.
- [155] J. Appel, H. Bockhorn, and M. Wulkow, "A detailed numerical study of the evolution of soot particle size distributions in laminar premixed flames," *Chemosphere*, vol. 42, pp. 635-645, Feb-Mar 2001.
- [156] H. Wang and M. Frenklach, "Calculations of Rate Coefficients for the Chemically Activated Reactions of Acetylene with Vinylic and Aromatic Radicals," *Journal of Physical Chemistry*, vol. 98, pp. 11465-11489, Nov 3 1994.
- [157] H. Wang and M. Frenklach, "Enthalpies of Formation of Benzenoid Aromatic-Molecules and Radicals," *Journal of Physical Chemistry*, vol. 97, pp. 3867-3874, Apr 15 1993.
- [158] H. Wang and M. Frenklach, "Transport properties of polycyclic aromatic hydrocarbons for flame modeling," *Combustion and Flame*, vol. 96, pp. 163-170, 1994.
- [159] A. Fahr and S. E. Stein, "Reactions of vinyl and phenyl radicals with ethyne, ethene and benzene," *Symposium (International) on Combustion*, vol. 22, pp. 1023-1029, 1989.

-
- [160] M. Frenklach, "On surface growth mechanism of soot particles," *Symposium (International) on Combustion*, vol. 26, pp. 2285-2293, 1996.
- [161] Matlab, "MatLab ver 7.1," 2008.
- [162] F. P. Incropera and D. P. De Witt, *Fundamentals of Heat and Mass Transfer*, 3rd ed.: John Wiley & Sons, 1990.
- [163] D. Bradley and A. G. Entwistle, "Determination of the emissivity, for total radiation, of small diameter platinum-10% rhodium wires in the temperature range 600-1450 degrees C," *British Journal of Applied Physics*, vol. 12, pp. 708-711, 1961.
- [164] J. F. Grcar, "The Twopnt program for boundary value problems," *Sandia National Laboratories Report SAND91-8230*, 1992.
- [165] Bronkhorst High Tech B.V., "Digital Mass Flow/Pressure instruments laboratory style/ IN-FLOW," 2009.
- [166] J. Zerbs, K.P. Geigle, O. Lammel, J. Hader, R. Stirn, R. Hader and W. Meker, "The influence of wavelength in extinction measurements and beam steering in laser-induced incandescence measurements in sooting flames," *Applied Physics B*, vol. 96, pp. 683-694, 2009.

APPENDIX A

A Premixed Flame Calculations

In this appendix describes in details the calculations needed for soot refractive index, soot volume fraction, two-dimensional LII image processing, temperature radiation correction losses and statistical analysis of soot morphology.

A.1 Refractive Index of Soot

On the basis of $m = 1.57 - 0.56i$ used as the real and imaginary parts of refractive index as discussed in Chapter 3.2, the complex index $E(m)$ is calculated based on the assumption that light scattering is negligible for a single soot particle within the Rayleigh limit which makes extinction comparable to absorption [60, 61, 65].

$$K_a = \frac{36\pi n_\lambda k_\lambda}{(n_\lambda^2 - k_\lambda^2 + 2)^2 + 4n_\lambda^2 k_\lambda^2} = K_e = 6\pi E(m) \quad \text{Equation 3.4}$$

Rearranging:

$$E(m) = \frac{6n_\lambda k_\lambda}{(n_\lambda^2 - k_\lambda^2 + 2)^2 + 4n_\lambda^2 k_\lambda^2} \quad \text{Equation 3.5}$$

By substituting $n_\lambda = 1.57$ and $k_\lambda = 0.56$ into the rearranged equation would yield an approximate value of 0.47. This value would then be placed into Equation 3, combined with transmission measurements across the flame, soot volume fraction can thus be determined.

A.2 Visual Determination of Laser Path

To determine the laser path through the flame, a single visual shot of the flame condition is taken. Using one of the flame conditions at $\phi = 2.22$ as an example,

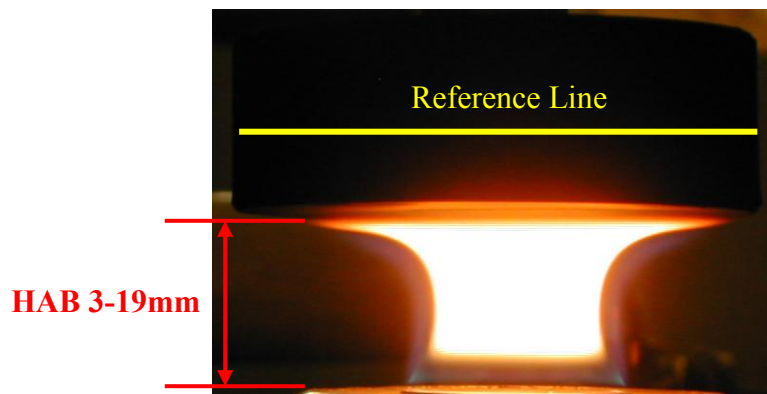


Figure 63 Measurement of laser path at $\phi = 2.22$

A reference line is drawn in Figure 63 to illustrate that the line measurement on the photograph corresponds to the 65 mm diameter stainless steel plate. By incorporating this reference line as datum to the image pixels, laser paths through the flame for each burner height can be determined by measuring the width of the luminosity. This can only be considered if the laser path through that particular height is assumed to be of a uniform absorption path length. A summary of the line measurements as determined from photographs is presented in Table 5.

Table 5 Summary of laser optical path through luminous part of flame

HAB (mm) \ Ø	Flame Width (mm)						
	1.82	1.95	2.08	2.22	2.84	3.10	3.80
3	34.4	33.8	32.7	31.2	31.0	31.9	30.2
4	31.9	32.5	31.6	30.4	29.1	29.9	28.9
5	30.6	31.2	30.6	29.3	27.6	29.1	27.2
6	28.8	29.1	28.8	28.0	26.6	27.8	26.3
7	27.6	27.8	27.3	27.2	25.5	26.9	25.9
8	27.3	26.9	26.7	26.5	24.9	26.1	25.5
9	26.7	26.1	25.8	26.1	24.0	25.7	25.3
10	26.3	25.7	25.4	25.2	23.8	25.2	25.1
11	25.8	25.2	24.8	25.2	23.6	25.2	25.1
12	25.8	24.8	24.8	25.2	23.6	25.2	25.1
13	25.4	24.8	24.8	25.2	23.8	25.2	25.5
14	25.4	24.8	24.8	25.7	24.2	25.7	25.7
15	25.4	25.4	25.2	26.3	24.6	26.1	26.3
16	26.3	26.1	25.4	26.9	25.5	26.9	27.2
17	27.1	26.9	27.1	28.2	26.8	28.2	28.9
18	28.4	28.7	28.4	29.9	28.0	29.7	31.9
19	30.6	30.6	30.1	31.6	30.6	31.6	35.7

A.3 Flame Extinction

Laser extinction through the flame can be derived by proper extraction of experimental data from both incident (\bar{I}_o) and transmitted (\bar{I}_T) laser intensities. For a time frame of 12.75 seconds for 3 sweeps per burner height, 3 peak-to-peak amplitudes are encountered for each sweep which amounts to a total of 768 samples. The maxima correspond to the experimental data together with background intensity whilst the minima correspond to the background only when the chopper blocks the laser from passing through the flame. The difference between the

two values would yield the „true“ value of the time-averaged laser intensity respectively. Furthermore to define a better estimate of the intensities, isolation of the peak-to-peak amplitudes is divided into 3 individual sections with a time range of 20 ms each.

As both transmitted and incident intensities are measured using different photodetectors, a photodetector compensation value has to be calibrated to a factor of 2.08 as measured prior to experiment. As mentioned previously (See Chapter 3.5), a trade-off value of 2.27 must be accounted for the conversion from transmitted to incident photomultiplier for the flameless procedure:

$$\frac{I_T}{I_0} \times \frac{2.08}{2.27} \quad \text{Equation A.1}$$

Consequently, the extinction coefficient, K_{ext} for any particular height can be calculated using Bouguer’s law [59], combined with the visually determined laser path length, L .

$$\frac{I_T}{I_0} = e^{-K_{ext} L} \quad \text{Equation 3.2}$$

A.4 Soot Volume Fraction

Soot volume fraction profiles are calculated by the use of a standardised formula [6-8] developed specifically for extinction measurements. Combined with earlier calculations on soot refractive index and extinction coefficient per height and intensity, soot volume fractions can thus be calculated for light extinction/scattering:

$$f_v = \frac{K_{ext} \lambda}{6\pi E(m)} \quad \text{Equation 3.3}$$

A.5 Treatment of LII Signals

400 two-dimensional accumulated raw images in the form of 8-bit tagged image format file (TIFF), measuring 300 by 200 pixels, are obtained from the LII measurements of laminar premixed flames for each burner height per equivalence ratio. 3 to 5 mm of the LII image at both ends is cut off to account for the unstable energy variation in the laser sheet thereby reducing the main reaction zone from HAB 7 to 15 mm instead. On top of that, the first 10 images of each file are neglected to account for flame instability. To facilitate the extraction of intensity values from each raw image file, a custom-written programme (MathLab[®]) [161]

has been developed for this purpose. It is found that for every 5 pixels in the image represents 1mm. Taking into account of background interference/dark charges, the intensity values are averaged and normalized to the highest intensity value at $\phi = 2.22$ of HAB 11 mm.

A.6 Radiation Heat Losses Correction

Measured temperature profiles are corrected for radiation and conduction losses using a balanced steady-state energy equation for small thermocouple bead. Assuming no catalytic effects on the fine wires and neglecting thermocouple oxidation, a simplified approach is drawn around the thermocouple bead [107]. Conduction effect around the lead wires is to be considered negligible as there is no knowledge of the temperature gradient at the interface of the bead and wire.

$$h_c A_{bead} (T_{gas} - T_{bead}) = \varepsilon \sigma A_{bead} (T_{bead}^4 - T_{\infty}^4) + \frac{k_w A_{wire}}{x} (T_{bead} - T_{ref}) \quad \text{Equation 5.1}$$

Rearranging Equation 6 to solve for gas temperature for fine wire thermocouples,

$$T_{gas} = T_{bead} + \frac{\varepsilon \sigma}{h_c} (T_{bead}^4 - T_{\infty}^4) \quad \text{Equation 5.2}$$

To determine the heat transfer coefficient, h_c , Nusselt number for forced convection over a sphere at low Reynolds number is used [108]:

$$Nu = 2 + (0.2Re)^{0.82} \quad \text{Equation 5.3}$$

Valid for: $Pr = 0.71$ and $0.07 \leq Re \leq 20$

The Nusselt, Reynolds and Prandtl numbers are given, respectively, by the following equations:

$$Nu = \frac{h_c d_{bead}}{k_{air}} \quad \text{Equation A.2}$$

$$Re = \frac{U_o d_{bead}}{v_{air}} \quad \text{Equation A.3}$$

$$Pr = \frac{v_{air}}{\alpha_{air}} \quad \text{Equation A.4}$$

Where d_{bead} is the thermocouple bead diameter, U_o is the burnt gas velocity, k_{air} , ν_{air} and α_{air} are the thermal conductivity, viscosity and thermal diffusivity of air, respectively. To solve for Equation 8, the thermophysical properties of the burnt gas must be known. Film temperature is evaluated to be the average value between the thermocouple and gas temperature. The thermophysical properties of the burnt gas are to be assumed to be those of air at film temperature as measurements were not done on the gas composition. The thermophysical properties are obtained from Incropera and De Witt [162]. The exit gas velocity U_o used in the Reynolds number is interpolated from nominal to actual conditions at 298 K and 1.013 bar. Thermocouple emissivity is a function of temperature and ranged between $0.16 \leq \varepsilon \leq 0.22$ for a Pt-10 %Rh vs. Pt thermocouple [163]. As soot constantly coats the bare thermocouple bead when exposed to sooty flame conditions, ε is assumed to be at unity for this temperature analysis.

Moreover, the presence of the ceramic coating around the thermocouple wires deters the „true“ determination of gas temperature. A major discrepancy value of 205 K as highlighted in Chapter 5.8 is added to the radiation correction profile for each measured temperature.

A.7 Soot Microscopy Statistical Analysis

Captured soot particles on the carbon film are analysed by transmission electron microscopy (TEM) under a magnification of 10,500 and 64,000 times. An image is formed upon electron interaction through the TEM grid which is then magnified and focused to measure comparable soot dimensions. It is found that under a magnification resolution of 10,500, soot particles are too small for statistical analysis. Therefore using a higher resolution such as 64,000, soot particles are magnified 10 times higher which gives a defined preview of primary soot particles leading up to agglomeration. To compensate for the higher resolution, the captured image profile only represents 10 % sample from the actual TEM image. At this resolution, each image is calibrated with a 200 nm line scale which is used to measure apparent spherical profiles of primary soot particles. The frequency of the soot agglomerates is not taken into account as it consists of several co-joined primary soot particles. But it is beneficial to take note of these features so as to track the formation of soot in laminar premixed flames.

APPENDIX B

B PREMIX Default Variables

In this APPENDIX describes the default solver specifications to achieve solution convergence for PREMIX flame code. Descriptions on the default settings for solution method can be found in the work of Kee and co-workers [154]. This guide is even extended to the setting up of custom input files as long as the syntax of the Keyword remains untouched. An initial energy equation computational is carried out to determine input prerequisites.

B.1 Solver Input Details

The image shows two screenshots of a software interface for setting solver parameters. The top screenshot shows the 'Basic' tab with the following parameters and values:

Parameter	Value
Absolute Tolerance	1.0E-9
Relative Tolerance	0.0001
Absolute Tolerance for Pseudo Timestepping	1.0E-9
Relative Tolerance for Pseudo Timestepping	0.0001

The bottom screenshot shows the 'Advanced' tab with the following parameters and values:

Parameter	Value	Unit
Pseudo Time Steps (Fixed Temperature)		
Number of Time Steps	100.0	
Initial Size of Time Step	1.0E-6	sec
Pseudo Time Steps (Energy Equation)		
Number of Time Steps	100.0	
Initial Size of Time Step	1.0E-6	sec
Minimum Pseudo Time Step	1.0E-10	sec
Maximum Pseudo Time Step	0.0001	sec
Number Time Steps Before Increasing	25.0	
Time Step Decrement Factor	2.0	
Number of Iterations before Updating Jacobian	20.0	
Number of Transient Iterations before Updating Jacobian	20.0	
Number of Initial Pseudo Time Steps	0.0	
Minimum Bounds on Species Fractions	-0.001	
Positive Value to Reset Species Fractions		

At the bottom of the Advanced tab, there are two radio buttons for differencing methods:

- Windward Differencing
- Central Differencing

Figure 64 Solver default variables

Figure 64 depicts the default variables employed in the Solver section of both energy and fixed gas temperature iterations. PREMIX code collaborates with another computer program, TWOPNT [164], to determine steady-state solutions for boundary value problems. First, the solver program attempts to solve the boundary conditions using a damped Newton's method. If this should not converge, TWOPNT program adopts a new Jacobian matrix for computing.

Any changes made to the absolute/relative tolerances for pseudo time-stepping, number and size of time-steps result in negligible effects observed in species profiles.

B.2 Reaction Zone Dimensions

In order to determine the flame dimensions needed for fixed gas temperature convergence, an initial energy equation computation is carried out to estimate the reaction zone prerequisites. Methyl radicals (CH_3) exhibit a Gaussian profile that centres and peaks in the main flame reaction zone as shown in Figure 56 (See Chapter 7.3.5). The shape of the profile does not have any effect on the convergence method. Table 6 summarises the dimensions of the reaction zone after energy equation iteration based on methyl radical (Note that: Flame simulation at $\text{Ø} = 2.84$ was tedious and failed to converge using same iteration method).

Table 6 Summary of reaction zone inputs used in CHEMKIN

Flame Test	Ø	Centre Position (mm)	Zone Width (mm)
1	1.82	2.35	8.35
2	1.95	2.55	8.45
3	2.08	2.65	8.45
4	2.22	2.75	8.12
6	3.10	3.4	6.45
7	3.80	3.85	5.6

APPENDIX C

C Tabulated Results

Calculated soot volume fraction results from laser diagnostics and thermocouple measurements are tabulated with respect to height above burner in this appendix.

C.1 Soot Volume Fraction (LE)

The manipulation of extinction measurements and laser path length into present soot volume fraction results is reviewed. Extinction measurements are attained between averaged transmitted and incident intensities (\bar{I}_T/\bar{I}_O) from photodiodes, **P1** and **P2**. The extinction coefficient, K_{ext} is determined by using Equation 2 and the measured laser path length in APPENDIX A.2. Finally, substitution of the refractive index of soot, $m = 1.57 - 0.56i$ into Equation 3. An overview of the calculated axial and radial results is shown in Tables 7 to 14.

Table 7 Summary of extinction measurements and soot volume fractions at $\emptyset = 1.82$

	Extinction Measurements	Extinction Coefficient	Soot Volume Fraction	Soot Volume Fraction (ppm)
HAB (mm)	\bar{I}_T/\bar{I}_O	$K_{ext} (\text{mm}^{-1})$	f_v	f_v (ppm)
3	0.996	0.129	9.216×10^{-9}	0.009
4	0.997	0.088	6.315×10^{-9}	0.006
5	0.997	0.093	6.652×10^{-9}	0.007
6	0.998	0.072	5.128×10^{-9}	0.005
7	0.993	0.242	1.728×10^{-8}	0.017
8	0.991	0.342	2.443×10^{-8}	0.024
9	0.982	0.673	4.803×10^{-8}	0.048
10	0.978	0.838	5.987×10^{-8}	0.060
11	0.967	1.308	9.341×10^{-8}	0.093
12	0.956	1.758	1.255×10^{-7}	0.126
13	0.947	2.139	1.527×10^{-7}	0.153
14	0.935	2.627	1.876×10^{-7}	0.188
15	0.930	2.853	2.037×10^{-7}	0.204
16	0.920	3.188	2.277×10^{-7}	0.228
17	0.918	3.156	2.253×10^{-7}	0.225
18	0.886	4.258	3.040×10^{-7}	0.304
19	0.874	4.417	3.154×10^{-7}	0.315

Table 8 Summary of extinction measurements and soot volume fractions at $\theta = 1.95$

	Extinction Measurements	Extinction Coefficient	Soot Volume Fraction	Soot Volume Fraction (ppm)
HAB (mm)	\bar{I}_T/\bar{I}_0	$K_{\text{ext}} (\text{mm}^{-1})$	f_v	f_v (ppm)
3	0.999	0.032	2.271×10^{-9}	0.002
4	0.999	0.016	1.149×10^{-9}	0.001
5	0.998	0.067	4.782×10^{-9}	0.005
6	0.995	0.165	1.175×10^{-8}	0.012
7	0.993	0.258	1.841×10^{-9}	0.018
8	0.983	0.619	4.420×10^{-8}	0.044
9	0.973	1.049	7.490×10^{-8}	0.075
10	0.964	1.425	1.018×10^{-7}	0.102
11	0.954	1.851	1.322×10^{-7}	0.132
12	0.935	2.702	1.929×10^{-7}	0.193
13	0.921	3.326	2.375×10^{-7}	0.237
14	0.907	3.918	2.797×10^{-7}	0.280
15	0.894	4.400	3.142×10^{-7}	0.314
16	0.879	4.931	3.521×10^{-7}	0.352
17	0.850	6.062	4.329×10^{-7}	0.433
18	0.840	6.072	4.335×10^{-7}	0.434
19	0.815	6.687	4.775×10^{-7}	0.478

Table 9 Summary of extinction measurements and soot volume fractions at $\varnothing = 2.08$

	Extinction Measurements	Extinction Coefficient	Soot Volume Fraction	Soot Volume Fraction (ppm)
HAB (mm)	\bar{I}_T/\bar{I}_0	$K_{\text{ext}} (\text{mm}^{-1})$	f_v	f_v (ppm)
3	0.996	0.130	9.266×10^{-9}	0.009
4	0.993	0.228	1.630×10^{-8}	0.016
5	0.992	0.272	1.943×10^{-8}	0.019
6	0.990	0.351	2.507×10^{-8}	0.025
7	0.987	0.487	3.480×10^{-8}	0.035
8	0.978	0.842	6.013×10^{-8}	0.060
9	0.963	1.453	1.038×10^{-7}	0.104
10	0.956	1.762	1.258×10^{-7}	0.126
11	0.929	2.989	2.135×10^{-7}	0.213
12	0.911	3.759	2.684×10^{-7}	0.268
13	0.895	4.493	3.208×10^{-7}	0.321
14	0.862	5.997	4.282×10^{-7}	0.428
15	0.846	6.631	4.735×10^{-7}	0.473
16	0.827	7.476	5.338×10^{-7}	0.534
17	0.811	7.735	5.523×10^{-7}	0.552
18	0.795	8.082	5.771×10^{-7}	0.577
19	0.774	8.516	6.081×10^{-7}	0.608

Table 10 Summary of extinction measurements and soot volume fractions at $\theta = 2.22$

	Extinction Measurements	Extinction Coefficient	Soot Volume Fraction	Soot Volume Fraction (ppm)
HAB (mm)	\bar{I}_T/\bar{I}_0	$K_{\text{ext}} (\text{mm}^{-1})$	f_v	f_v (ppm)
3	0.996	0.139	9.944×10^{-9}	0.010
4	0.996	0.144	1.025×10^{-8}	0.010
5	0.995	0.178	1.274×10^{-8}	0.013
6	0.994	0.225	1.607×10^{-8}	0.016
7	0.989	0.401	2.864×10^{-8}	0.029
8	0.982	0.689	4.918×10^{-8}	0.049
9	0.969	1.194	8.523×10^{-8}	0.085
10	0.953	1.904	1.360×10^{-7}	0.136
11	0.937	2.595	1.853×10^{-7}	0.185
12	0.914	3.550	2.535×10^{-7}	0.254
13	0.891	4.581	3.271×10^{-7}	0.327
14	0.847	6.445	4.602×10^{-7}	0.460
15	0.823	7.427	5.304×10^{-7}	0.530
16	0.790	8.760	6.256×10^{-7}	0.626
17	0.766	9.440	6.741×10^{-7}	0.674
18	0.745	9.839	7.026×10^{-7}	0.703
19	0.690	11.744	8.386×10^{-7}	0.839

Table 11 Summary of extinction measurements and soot volume fractions at $\theta = 2.84$

	Extinction Measurements	Extinction Coefficient	Soot Volume Fraction	Soot Volume Fraction (ppm)
HAB (mm)	\bar{I}_T/\bar{I}_0	$K_{\text{ext}} (\text{mm}^{-1})$	f_v	f_v (ppm)
3	0.999	0.037	2.669×10^{-9}	0.003
4	0.997	0.099	7.085×10^{-9}	0.007
5	0.999	0.046	3.305×10^{-9}	0.003
6	0.997	0.095	6.797×10^{-9}	0.007
7	0.995	0.178	1.274×10^{-8}	0.013
8	0.994	0.254	1.813×10^{-8}	0.018
9	0.986	0.573	4.091×10^{-8}	0.041
10	0.980	0.837	5.980×10^{-8}	0.060
11	0.965	1.493	1.066×10^{-7}	0.107
12	0.941	2.567	1.833×10^{-7}	0.183
13	0.930	3.044	2.174×10^{-7}	0.217
14	0.892	4.701	3.357×10^{-7}	0.336
15	0.868	5.732	4.093×10^{-7}	0.409
16	0.848	6.463	4.615×10^{-7}	0.462
17	0.809	7.896	5.638×10^{-7}	0.564
18	0.762	9.695	6.923×10^{-7}	0.692
19	0.701	11.594	8.279×10^{-7}	0.828

Table 12 Summary of extinction measurements and soot volume fractions at $\theta = 3.10$

	Extinction Measurements	Extinction Coefficient	Soot Volume Fraction	Soot Volume Fraction (ppm)
HAB (mm)	\bar{I}_T/\bar{I}_0	$K_{ext} (mm^{-1})$	f_v	f_v (ppm)
3	0.998	0.053	3.797×10^{-9}	0.004
4	0.999	0.038	2.705×10^{-9}	0.003
5	0.998	0.065	4.609×10^{-9}	0.005
6	0.995	0.188	1.341×10^{-8}	0.013
7	0.996	0.160	1.142×10^{-8}	0.011
8	0.993	0.274	1.958×10^{-8}	0.020
9	0.990	0.400	2.859×10^{-8}	0.029
10	0.972	1.130	8.070×10^{-8}	0.081
11	0.968	1.271	9.078×10^{-8}	0.091
12	0.967	1.350	9.638×10^{-8}	0.096
13	0.934	2.730	1.949×10^{-7}	0.195
14	0.918	3.340	2.385×10^{-7}	0.239
15	0.895	4.242	3.029×10^{-7}	0.303
16	0.857	5.726	4.089×10^{-7}	0.409
17	0.825	6.813	4.865×10^{-7}	0.486
18	0.799	7.573	5.408×10^{-7}	0.541
19	0.786	7.623	5.443×10^{-7}	0.544

Table 13 Summary of extinction measurements and soot volume fractions at $\theta = 3.80$

	Extinction Measurements	Extinction Coefficient	Soot Volume Fraction	Soot Volume Fraction (ppm)
HAB (mm)	\bar{I}_T/\bar{I}_0	$K_{ext}(\text{mm}^{-1})$	f_v	f_v (ppm)
3	1.001	(0.023)	(1.611×10^{-9})	(0.002)
4	1.001	(0.022)	(1.603×10^{-9})	(0.002)
5	1.000	0.007	5.248×10^{-10}	0.001
6	0.998	0.060	4.274×10^{-9}	0.004
7	0.995	0.177	1.260×10^{-8}	0.013
8	0.998	0.084	6.024×10^{-9}	0.006
9	0.988	0.464	3.315×10^{-8}	0.033
10	0.988	0.500	3.567×10^{-8}	0.036
11	0.981	0.783	5.591×10^{-8}	0.056
12	0.966	1.389	9.920×10^{-8}	0.099
13	0.955	1.797	1.283×10^{-7}	0.128
14	0.949	2.046	1.461×10^{-7}	0.146
15	0.920	3.175	2.267×10^{-7}	0.227
16	0.905	3.659	2.613×10^{-7}	0.261
17	0.901	3.598	2.569×10^{-7}	0.257
18	0.857	4.843	3.458×10^{-7}	0.346
19	0.815	5.718	4.083×10^{-7}	0.408

Table 14 Summary of radial extinction measurements and soot volume fractions at $\phi = 2.84$

		Extinction Measurements	Extinction Coefficient	Soot Volume Fraction	Soot Volume Fraction (ppm)
HAB (mm)	Radial Position (mm)	\bar{I}_T/\bar{I}_O	$K_{ext} (mm^{-1})$	f_v	f_v (ppm)
9	-12	0.997	0.441	3.148×10^{-8}	0.031
	-10	0.993	0.441	3.148×10^{-8}	0.031
	-8	0.988	0.620	4.424×10^{-8}	0.044
	-6	0.984	0.715	5.105×10^{-8}	0.051
	-4	0.982	0.774	5.530×10^{-8}	0.055
	-2	0.982	0.715	5.105×10^{-8}	0.051
	0	0.982	0.715	5.105×10^{-8}	0.051
	2	0.982	0.715	5.105×10^{-8}	0.051
	4	0.986	0.584	4.169×10^{-8}	0.042
	6	0.987	0.584	4.169×10^{-8}	0.042
	8	0.987	0.667	4.765×10^{-8}	0.048
	10	0.992	0.512	3.658×10^{-8}	0.037
	12	0.996	0.548	3.914×10^{-8}	0.039
11	-12	0.983	1.906	1.361×10^{-7}	0.136
	-10	0.970	1.906	1.361×10^{-7}	0.136
	-8	0.962	1.942	1.387×10^{-7}	0.139
	-6	0.955	2.026	1.446×10^{-7}	0.145
	-4	0.957	1.799	1.285×10^{-7}	0.128
	-2	0.959	1.668	1.191×10^{-7}	0.119
	0	0.956	1.740	1.242×10^{-7}	0.124
	2	0.959	1.644	1.174×10^{-7}	0.117
	4	0.959	1.704	1.217×10^{-7}	0.122
	6	0.962	1.692	1.208×10^{-7}	0.121
	8	0.966	1.728	1.234×10^{-7}	0.123
	10	0.973	1.692	1.208×10^{-7}	0.121
	12	0.983	1.906	1.361×10^{-7}	0.136
13	-12	0.960	4.289	3.063×10^{-7}	0.306
	-10	0.931	4.361	3.114×10^{-7}	0.311
	-8	0.922	4.027	2.876×10^{-7}	0.288
	-6	0.916	3.849	2.748×10^{-7}	0.275
	-4	0.918	3.479	2.484×10^{-7}	0.248
	-2	0.914	3.515	2.510×10^{-7}	0.251
	0	0.912	3.575	2.552×10^{-7}	0.255
	2	0.912	3.598	2.569×10^{-7}	0.257
	4	0.921	3.336	2.382×10^{-7}	0.238
	6	0.920	3.634	2.595×10^{-7}	0.259
	8	0.928	3.670	2.620×10^{-7}	0.262
	10	0.937	3.968	2.833×10^{-7}	0.283
	12	0.961	4.158	2.969×10^{-7}	0.297

Cont'd

		Extinction Measurements	Extinction Coefficient	Soot Volume Fraction	Soot Volume Fraction (ppm)
HAB (mm)	Radial Position (mm)	\bar{I}_T/\bar{I}_O	$K_{ext} (mm^{-1})$	f_v	f_v (ppm)
15	-12	0.924	7.935	5.666×10^{-7}	0.567
	-10	0.884	7.423	5.301×10^{-7}	0.530
	-8	0.873	6.613	4.722×10^{-7}	0.472
	-6	0.865	6.291	4.492×10^{-7}	0.449
	-4	0.856	6.291	4.492×10^{-7}	0.449
	-2	0.854	6.148	4.390×10^{-7}	0.439
	0	0.853	6.112	4.365×10^{-7}	0.436
	2	0.852	6.255	4.467×10^{-7}	0.447
	4	0.860	6.112	4.365×10^{-7}	0.436
	6	0.860	6.541	4.671×10^{-7}	0.467
	8	0.876	6.434	4.594×10^{-7}	0.459
	10	0.887	7.244	5.173×10^{-7}	0.517
	12	0.927	7.626	5.445×10^{-7}	0.545
17	-12	0.867	13.547	9.674×10^{-7}	0.967
	-10	0.840	10.295	7.351×10^{-7}	0.735
	-8	0.820	9.592	6.849×10^{-7}	0.685
	-6	0.809	9.103	6.500×10^{-7}	0.650
	-4	0.800	8.924	6.373×10^{-7}	0.637
	-2	0.796	8.817	6.296×10^{-7}	0.630
	0	0.793	8.865	6.330×10^{-7}	0.633
	2	0.794	8.924	6.373×10^{-7}	0.637
	4	0.796	9.127	6.517×10^{-7}	0.652
	6	0.806	9.246	6.602×10^{-7}	0.660
	8	0.821	9.484	6.772×10^{-7}	0.677
	10	0.842	10.128	7.232×10^{-7}	0.723
	12	0.870	13.273	9.478×10^{-7}	0.948

C.2 Calibration of Soot Volume Fraction (LII)

Manipulation of LII signals into soot volume fractions by single-point calibration against laser extinction is reviewed. The ICCD camera captures the soot incandescence in the form of two-dimensional images and MathLab[®] is employed to extract relevant values out of these images. LII signals are averaged over 5 pixels on the image. Background intensity values are taken into consideration for each flame condition. Single-point calibration at $\varnothing = 2.22$ of HAB 11mm against laser extinction is used to convert LII signals into present soot volume results. This point is found to be 1.90×10^{-4} ppm per intensity. Calibrated soot volume fraction profiles from HAB 7 to 15 mm in all flame test conditions are shown in Tables 15 to 21. Table 22 refers to the radial soot volume fractions at $\varnothing = 2.84$ after calibration.

Table 15 Calibration of LII signals into soot volume fraction at $\varnothing = 1.82$

Background Noise = 463.73			Soot Volume Fraction (LII)
HAB (mm)	Average Signal Intensity (Before)	Average Signal Intensity (After)	f_v (ppm)
7	691.08	227.35	0.043
8	846.38	382.66	0.073
9	1027.16	563.43	0.107
10	1197.43	733.71	0.139
11	1367.78	904.05	0.172
12	1489.66	1025.93	0.195
13	1504.80	1041.07	0.198
14	1506.60	1042.87	0.198
15	1561.87	1098.14	0.209

Table 16 Calibration of LII signals into soot volume fraction at $\Theta = 1.95$

Background Noise = 281.67			Soot Volume Fraction (LII)
HAB (mm)	Average Signal Intensity (Before)	Average Signal Intensity (After)	f_v (ppm)
7	567.06	285.39	0.054
8	758.87	477.20	0.091
9	956.25	674.58	0.128
10	1171.49	889.82	0.169
11	1348.00	1066.34	0.203
12	1452.16	1170.49	0.222
13	1455.10	1173.43	0.223
14	1505.63	1223.97	0.232
15	1498.53	1216.86	0.231

Table 17 Calibration of LII signals into soot volume fraction at $\Theta = 2.08$

Background Noise = 230.15			Soot Volume Fraction (LII)
HAB (mm)	Average Signal Intensity (Before)	Average Signal Intensity (After)	f_v (ppm)
7	483.90	253.76	0.048
8	709.47	479.32	0.091
9	959.39	729.24	0.139
10	1235.70	1005.55	0.191
11	1460.17	1230.03	0.234
12	1575.48	1345.33	0.256
13	1572.53	1342.39	0.255
14	1634.61	1404.47	0.267
15	1601.28	1371.13	0.260

Table 18 Calibration of LII signals into soot volume fraction at $\Theta = 2.22$

Background Noise = 230.42			Soot Volume Fraction (LII)
HAB (mm)	Average Signal Intensity (Before)	Average Signal Intensity (After)	f_v (ppm)
7	286.75	56.33	0.011
8	374.76	144.34	0.027
9	560.55	330.13	0.063
10	849.58	619.16	0.118
11	1205.99	975.57	0.185
12	1497.90	1267.48	0.241
13	1607.59	1377.17	0.262
14	1685.05	1454.63	0.276
15	1743.99	1513.57	0.288

Table 19 Calibration of LII signals into soot volume fraction at $\Theta = 2.84$

Background Noise = 226.66			Soot Volume Fraction (LII)
HAB (mm)	Average Signal Intensity (Before)	Average Signal Intensity (After)	f_v (ppm)
7	238.39	11.73	0.002
8	255.97	29.30	0.006
9	301.95	75.29	0.014
10	382.87	156.20	0.030
11	502.21	275.55	0.052
12	623.17	396.50	0.075
13	705.78	479.12	0.091
14	815.61	588.95	0.112
15	872.68	646.02	0.123

Table 20 Calibration of LII signals into soot volume fraction at $\Theta = 3.10$

Background Noise = 244.35			Soot Volume Fraction (LII)
HAB (mm)	Average Signal Intensity (Before)	Average Signal Intensity (After)	f_v (ppm)
7	256.02	11.67	0.002
8	274.30	29.96	0.006
9	317.79	73.44	0.014
10	380.99	136.64	0.026
11	478.61	234.26	0.044
12	581.12	336.77	0.064
13	646.39	402.04	0.076
14	706.18	461.83	0.088
15	766.46	522.11	0.099

Table 21 Calibration of LII signals into soot volume fraction at $\Theta = 3.80$

Background Noise = 248.90			Soot Volume Fraction (LII)
HAB (mm)	Average Signal Intensity (Before)	Average Signal Intensity (After)	f_v (ppm)
7	260.44	11.54	0.003
8	273.56	24.66	0.007
9	308.90	60.00	0.019
10	358.43	109.53	0.036
11	424.40	175.49	0.061
12	472.09	223.19	0.080
13	498.70	249.80	0.092
14	531.69	282.78	0.109
15	529.48	280.58	0.105

Table 22 Radial soot volume fractions from LII calibration at $\varnothing = 2.84$

Background Noise = 226.66				Soot Volume Fraction (LII)
HAB (mm)	Radial Position (mm)	Average Signal Intensity (Before)	Average Signal Intensity (After)	f_v (ppm)
9	-12	803.79	577.13	0.110
	-10	579.93	353.27	0.067
	-8	499.13	272.47	0.052
	-6	472.86	246.20	0.047
	-4	475.99	249.33	0.047
	-2	458.46	231.80	0.044
	0	474.99	248.33	0.047
	2	477.26	250.60	0.048
	4	464.39	237.73	0.045
	6	466.79	240.13	0.046
	8	463.13	236.47	0.045
	10	481.33	254.67	0.048
	12	475.26	248.60	0.047
11	-12	1475.93	1249.27	0.237
	-10	953.46	726.80	0.138
	-8	669.99	443.33	0.084
	-6	580.73	354.07	0.067
	-4	552.39	325.73	0.062
	-2	544.66	318.00	0.060
	0	538.59	311.93	0.059
	2	572.06	345.40	0.066
	4	547.93	321.27	0.061
	6	545.33	318.67	0.061
	8	558.26	331.60	0.063
	10	556.46	329.80	0.063
	12	617.79	391.13	0.074
13	-12	1871.86	1645.20	0.313
	-10	1331.46	1104.80	0.210
	-8	886.79	660.13	0.125
	-6	733.99	507.33	0.096
	-4	707.46	480.80	0.091
	-2	709.39	482.73	0.092
	0	702.06	475.40	0.090
	2	688.06	461.40	0.088
	4	702.93	476.27	0.090
	6	700.39	473.73	0.090
	8	684.99	458.33	0.087
	10	701.46	474.80	0.090
	12	762.06	535.40	0.102

Cont'd

Background Noise = 226.66				Soot Volume Fraction (LII)
HAB (mm)	Radial Position (mm)	Average Signal Intensity (Before)	Average Signal Intensity (After)	f_v (ppm)
15	-12	1970.59	1743.93	0.331
	-10	1505.26	1278.60	0.243
	-8	1113.39	886.73	0.168
	-6	945.33	718.67	0.137
	-4	884.73	658.07	0.125
	-2	884.06	657.40	0.125
	0	879.53	652.87	0.124
	2	880.06	653.40	0.124
	4	864.73	638.07	0.121
	6	863.73	637.07	0.121
	8	854.53	627.87	0.119
	10	868.19	641.53	0.122
	12	943.26	716.60	0.136

C.3 Temperatures after Correction

The potential differences measured from the thermocouple are amplified using an in-house built voltage amplifier. To convert these potentials, a simple conversion of 2.5 mV per degree is applied, knowing the offset of the amplifier. Gas temperatures are corrected to compensate for heat losses by radiation and ceramic wire cooling (See APPENDIX A.6). The final temperature results are shown in Table 23 to 29. Radial temperatures at $\varnothing = 2.84$ are tabulated in Table 30.

Table 23 Axial temperatures after radiation correction at $\varnothing = 1.82$

Average Detected Voltage		Before Correction	After Correction
HAB (mm)	V (mV)	T (K)	T (K)
3	1998	1072.20	1505.71
4	1943	1050.20	1467.17
5	1918	1040.20	1450.23
6	1902	1033.80	1439.42
7	1892	1029.80	1432.73
8	1872	1021.80	1419.62
9	1862	1017.80	1412.81
10	1858	1016.20	1410.40
11	1822	1001.80	1386.98
12	1795	991.00	1369.45
13	1795	991.00	1369.26
14	1748	972.20	1339.76
15	1690	949.00	1303.14
16	1648	932.20	1276.04
17	1580	905.00	1236.14
18	1500	873.00	1189.42
19	1412	837.80	1139.19

Table 24 Axial temperatures after radiation correction at $\emptyset = 1.95$

Average Detected Voltage		Before Correction	After Correction
HAB (mm)	V (mV)	T (K)	T (K)
3	2000	1073.00	1507.92
4	1938	1048.20	1464.22
5	1910	1037.00	1445.15
6	1895	1031.00	1435.09
7	1878	1024.20	1423.87
8	1868	1020.20	1417.23
9	1835	1007.00	1395.56
10	1795	991.00	1369.63
11	1820	1001.00	1385.99
12	1780	985.00	1360.19
13	1768	980.20	1352.45
14	1690	949.00	1303.48
15	1660	937.00	1284.96
16	1618	920.20	1259.32
17	1588	908.20	1241.60
18	1468	860.20	1171.20
19	1392	829.80	1128.08

Table 25 Axial temperatures after radiation correction at $\emptyset = 2.08$

Average Detected Voltage		Before Correction	After Correction
HAB (mm)	V (mV)	T (K)	T (K)
3	1922	1041.80	1453.72
4	1898	1032.20	1437.60
5	1810	997.00	1379.26
6	1792	989.80	1367.72
7	1780	985.00	1360.33
8	1760	977.00	1347.37
9	1755	975.00	1344.38
10	1738	968.20	1333.37
11	1730	965.00	1328.40
12	1723	962.20	1324.11
13	1675	943.00	1294.14
14	1658	936.20	1283.95
15	1638	928.20	1271.73
16	1602	913.80	1249.90
17	1478	864.20	1177.00
18	1422	841.80	1145.23
19	1365	819.00	1113.45

Table 26 Axial temperatures after radiation correction at $\emptyset = 2.22$

Average Detected Voltage		Before Correction	After Correction
HAB (mm)	V (mV)	T (K)	T (K)
3	1918	1040.20	1451.65
4	1895	1031.00	1436.25
5	1832	1005.80	1394.17
6	1810	997.00	1379.98
7	1785	987.00	1363.65
8	1765	979.00	1350.86
9	1765	979.00	1351.05
10	1748	972.20	1340.17
11	1740	969.00	1334.99
12	1730	965.00	1328.69
13	1715	959.00	1319.62
14	1682	945.80	1298.80
15	1650	933.00	1279.21
16	1638	928.20	1272.14
17	1510	877.00	1195.90
18	1490	869.00	1184.31
19	1410	837.00	1138.73

Table 27 Axial temperatures after radiation correction at $\emptyset = 2.84$

Average Detected Voltage		Before Correction	After Correction
HAB (mm)	V (mV)	T (K)	T (K)
3	1662	937.80	1288.74
4	1760	977.00	1350.25
5	1845	1011.00	1405.24
6	1848	1012.20	1405.69
7	1830	1005.00	1393.93
8	1832	1005.80	1395.32
9	1842	1009.80	1401.90
10	1830	1005.00	1394.14
11	1835	1007.00	1397.22
12	1818	1000.20	1386.22
13	1802	993.80	1376.19
14	1752	973.80	1343.70
15	1735	967.00	1333.22
16	1685	947.00	1302.58
17	1622	921.80	1263.25
18	1548	892.20	1219.00
19	1490	869.00	1185.32

Table 28 Axial temperatures after radiation correction at $\emptyset = 3.10$

Average Detected Voltage		Before Correction	After Correction
HAB (mm)	V (mV)	T (K)	T (K)
3	1375	823.00	1119.71
4	1505	875.00	1193.67
5	1698	952.20	1310.40
6	1805	995.00	1378.41
7	1802	993.80	1375.95
8	1778	984.20	1360.51
9	1770	981.00	1355.27
10	1748	972.20	1341.54
11	1742	969.80	1337.51
12	1732	965.80	1331.36
13	1705	955.00	1314.32
14	1688	948.20	1303.81
15	1625	923.00	1264.97
16	1580	905.00	1237.83
17	1525	883.00	1205.49
18	1458	856.20	1167.06
19	1370	821.00	1117.05

Table 29 Axial temperatures after radiation correction at $\varnothing = 3.80$

Average Detected Voltage		Before Correction	After Correction
HAB (mm)	V (mV)	T (K)	T (K)
3	1055	695.00	950.83
4	1152	733.80	1000.32
5	1280	785.00	1068.00
6	1425	843.00	1148.86
7	1565	899.00	1229.73
8	1610	917.00	1256.74
9	1725	963.00	1327.69
10	1708	956.20	1316.75
11	1723	962.20	1326.18
12	1700	953.00	1312.16
13	1678	944.20	1298.04
14	1662	937.80	1288.61
15	1618	920.20	1261.37
16	1588	908.20	1243.40
17	1520	881.00	1203.04
18	1448	852.20	1161.64
19	1368	820.20	1116.39


Table 30 Radial temperatures after correction at $\varnothing = 2.84$

		Radial Position (mm)				
		-10	-5	0	5	10
Average Detected Voltage	V (mV)	1913	1838	1755	1791	1836
Before Correction	T (K)	1038.09	1008.27	975.10	989.58	1007.42
After Correction	T (K)	1448.70	1399.03	1345.33	1368.55	1397.54

APPENDIX D

D Mass Flow Controller Calibration Sheets

To calibrate the tube and ball flowmeters, thermal mass flow controllers (MFCs) from Bronkhorst High-Tech [165] are used to precisely determine the separate flows of ethylene, air and nitrogen. Both mass flow controllers (Model F-201CV-500AAAD-22-E) are connected and controlled via a power supply/readout unit (Model E-5714). Calibration sheets for these MFCs are shown in Figure 65 and Figure 66.



Page: 1 - 1

CALIBRATION CERTIFICATE

FLUID NO. 1 OF 1

CERTIFICATE NO. BHTC69/CL9/873346

Calibration by comparison
Calibration date: 3 Dec 2009

We hereby certify that the instrument mentioned below has been calibrated in accordance with the stated values and conditions. The calibration standards used are traceable to national standards of the Dutch Metrology Institute VSL.

Calibrated instrument		Calibration standard	
Type	Flow controller (D)	Type	Piston Prover
Serial number	M9209559B	Serial number	80206
Model number	F-201CV-500-AAD-22-E	Certificate no.	BHTG09/667492
Rated accuracy*	±(0.8%Rd + 0.2%FS)	Uncertainty	±0.3% Rd

Customer conditions		Calibration conditions	
Fluid	C2H4	Fluid	AiR
Flow	200.0 mln/min	Flow	328.3 mln/min (equivalent flow)
Pressure	20.0 psi (g)	Pressure	5.0 bar (a)
Temperature	20.0 °C	Temperature	24.0 °C
		Atm. pressure	996.6 hPa (a)

Calibration and Conversion results

Point	Calibrated flow		Conversion factor	Customer flow**		Output signal	
	AIR	C2H4		C2H4			
1	0.0000 mln/min		-	0.0000 mln/min	0.00%	0.000 V	
2	39.98 mln/min		0.609	24.33 mln/min	12.17%	0.608 V	
3	80.00 mln/min		0.609	48.69 mln/min	24.34%	1.217 V	
4	120.0 mln/min		0.609	73.03 mln/min	36.52%	1.826 V	
5	160.0 mln/min		0.609	97.38 mln/min	48.69%	2.435 V	
6	200.0 mln/min		0.609	121.7 mln/min	60.87%	3.044 V	
7	240.0 mln/min		0.609	146.1 mln/min	73.06%	3.653 V	
8	320.0 mln/min		0.609	194.9 mln/min	97.47%	4.874 V	
9	400.0 mln/min		0.610	243.8 mln/min	121.92%	6.098 V***	

The measurement uncertainty of the calibrated AIR flow is ±0.4% Rd.
The measured deviation between the flow indicated by the calibrated instrument and the reference flow indicated by the calibration standard is less than ±0.21% Rd.

Notes

Flow unit mln/min is defined at conditions 0.00 °C, 1013.25 hPa (a).
 * Rated accuracy is specified under calibration conditions.
 ** The calibrated flow is converted to customer fluid and/or conditions using Bronkhorst High-Tech FLUIDAT® software.
 *** Analog output above 5 V cannot be guaranteed.

Measurement uncertainties are based upon 95% (k=2) confidence limits. Although the item calibrated meets the specifications and performance at the time of calibration, due to any number of factors, this does not imply continuing conformance to the specifications.

More detailed information about the used calibration method can be found on <http://www.bronkhorst.com/certificates>.

Calibrator	R.Kh.	QC	M.F.K.
Signed		Date	7 Dec 2009
		Signed	

BHTMultiFluidToolDLL V2.02 FLUIDAT® V5.50 (Database: 05-05-1999) Report V1.03

Figure 65 Calibration Sheet for Ethylene Mass Flow Controller



CALIBRATION CERTIFICATE

FLUID NO. 1 OF 1

CERTIFICATE NO. BHTC69/CL9/873342

Calibration by comparison
Calibration date: 3 Dec 2009

We hereby certify that the instrument mentioned below has been calibrated in accordance with the stated values and conditions. The calibration standards used are traceable to national standards of the Dutch Metrology Institute VSL.

Calibrated instrument

Type Flow controller (D)
Serial number M9209559A
Model number F-201CV-1K0-AAD-22-V
Rated accuracy* $\pm(0.8\%Rd + 0.2\%FS)$

Calibration standard

Type Piston Prover
Serial number 80204
Certificate no. BHTG09/634940
Uncertainty $\pm 0.3\% Rd$

Customer conditions

Fluid **AIR**
Flow **1000 ml/min**
Pressure **20.0 psi (g)**
Temperature **20.0 °C**

Calibration conditions

Fluid **AIR**
Flow **997.2 ml/min (equivalent flow)**
Pressure **5.0 bar (a)**
Temperature **22.3 °C**
Atm. pressure **997.5 hPa (a)**

Calibration and Conversion results

Point	Calibrated flow		Conversion factor	Customer flow**		Output signal
	AIR			AIR		
1	0.000	ml/min	-	0.000	ml/min	0.00% 0.000 V
2	79.91	ml/min	1.003	80.17	ml/min	8.02% 0.401 V
3	159.9	ml/min	1.003	160.4	ml/min	16.04% 0.802 V
4	239.8	ml/min	1.003	240.6	ml/min	24.06% 1.203 V
5	319.8	ml/min	1.003	320.8	ml/min	32.08% 1.604 V
6	399.7	ml/min	1.003	401.0	ml/min	40.10% 2.005 V
7	479.7	ml/min	1.003	481.2	ml/min	48.12% 2.406 V
8	639.7	ml/min	1.003	641.6	ml/min	64.16% 3.208 V
9	799.5	ml/min	1.003	801.9	ml/min	80.19% 4.010 V
10	959.5	ml/min	1.003	962.3	ml/min	96.23% 4.812 V
11	1119	ml/min	1.003	1123	ml/min	112.27% 5.613 V***

The measurement uncertainty of the calibrated AIR flow is $\pm 0.4\% Rd$.
The measured deviation between the flow indicated by the calibrated instrument and the reference flow indicated by the calibration standard is less than $\pm 0.16\% Rd$.

Notes

Flow unit ml/min is defined at conditions 0.00 °C, 1013.25 hPa (a).

* Rated accuracy is specified under calibration conditions.

** The calibrated flow is converted to customer fluid and/or conditions using Bronkhorst High-Tech FLUIDAT® software.

*** Analog output above 5 V cannot be guaranteed.

Measurement uncertainties are based upon 95% (k=2) confidence limits. Although the item calibrated meets the specifications and performance at the time of calibration, due to any number of factors, this does not imply continuing conformance to the specifications.

More detailed information about the used calibration method can be found on <http://www.bronkhorst.com/certificates>.

Calibrator R.Kh.

QC M.F.K.

Date 7 Dec 2009

Signed

Signed

Figure 66 Calibration Sheet for Air Mass Flow Controller

APPENDIX E

E Publications

Publication arising from this thesis

Wang, Y., Nathan, G.J., Alwahabi, Z.T., King, K.D., Ho, K. and Yao, Q. (2010)
Effect of a uniform electric field on soot in laminar premixed ethylene/air flames.
Combustion and Flame, v. 157 (7), pp. 1308-1315, July 2010

NOTE: This publication is included in the print copy of the thesis
held in the University of Adelaide Library.

It is also available online to authorised users at:

<http://dx.doi.org/10.1016/j.combustflame.2010.03.001>